Time Component of Weak Nuclear Axial Vector Currents in the Mass A=12 System

– Beta-ray Angular Distribution from Aligned ^{12}B and ^{12}N –

Atsushi Kitagawa

Dissertation in Physics

OSAKA UNIVERSITY

GRADUATE SCHOOL OF SCIENCE

TOYONAKA, OSAKA 560, JAPAN

August 1992

Abstract

In order to study the meson-exchange effect in the time component of the weak nuclear axial vector currents, the beta-ray angular distributions from aligned mirror nuclei of ^{12}B and ^{12}N, ($\boldsymbol{J}^{\pi}$,T,T$_z$:1^+,1,$\mp$1) $\rightarrow$ (0^+,0,0), were observed as a function of beta-ray energies and a pair of the alignment-correlation coefficients was precisely determined. The sum of the coefficients is proportional to the time component and does not include the unknown weak interaction coupling constants. Moreover, the sum of coefficients is an excellent probe for the meson-exchange effect in the time component, because it is predicted by a recent theoretical study that the meson-exchange current enhances the time component by about 40% than the value calculated under the impulse approximation. The present study is of crucial importance for investigations of the non-nucleonic degree of freedom in a nucleus, that is one of the most important problems to be disclosed in the current nuclear physics.

The alignment-correlation coefficients of ^{12}B and ^{12}N were determined in the previous experiments, that was mainly performed to investigate the limitation of G-parity conservation. However, these results turned out to be insufficient to precisely probe the meson-exchange current, because the spin manipulation for determining the alignment was incomplete and thus the systematic errors in the determined degree of alignment were not rejected. In the present experiment, the spin manipulation technique for determining the degree of alignment was improved so that the reliability in the determined coefficients was greatly improved.

The spin manipulation technique was based on the β-NMR of ^{12}B(^{12}N) in a Mg

single crystal (hcp structure). In the recent studies on the hyperfine interactions of the ^{12}B and ^{12}N implanted in Mg crystal, the second minority site was found (the small fraction of about 15% was located). The present improvement consisted of the spin manipulations of ^{12}B and ^{12}N not only in the majority site, but also in the minority site.

From the experimental viewpoint, the measurement of the alignment-correlation coefficients is much freer than the polarization-correlation one from systematic errors due to any small mixtures of background beta rays, scattered beta rays and any other detector configurations. Moreover, the method for calibrating the beta-ray energy was also improved than the previous experiments. Consequently, it has become possible to compare the experimental and theoretical value as a function of the beta-ray energy for more definite discussions on the meson-exchange current.

The alignment-correlation coefficient was determined from the ratio of the observed beta-ray energy spectrum with the pure plus and minus alignment. The pure alignments of both signs ($A = \pm(7.1 \pm 0.1)\%$ with $P = 0.1 \pm 0.1\%$ for ^{12}B, and $A = \pm(17.1 \pm 0.2)$ with $P = 0.2 \pm 0.1$ for ^{12}N, typically) were created by converting the initial polarization obtained through nuclear reactions. The precise degrees of alignment were obtained by the improved spin-manipulation technique.

The alignment-correlation coefficients ($\alpha_{\mp}$) were deduced by averaging the alignment correlation terms ($\left[\frac{B_2(E)}{B_0(E)}\right]$) divided by the beta-ray energy. The coefficients of ^{12}B and ^{12}N were determined as $\alpha_- = -0.0174 \pm 0.0056$ (%/MeV) and $\alpha_+ = -0.2774 \pm 0.0086$ (%/MeV), respectively. The most reliable value of a sum of the alignment coefficients, which is proportional to the time component term, was determined as $(\alpha_- + \alpha_+) = -0.2948 \pm 0.0107$ (%/MeV).

The present observed value of $(\alpha_- + \alpha_+)$ is found to be larger by about $36 \pm 5\%$ than the theoretical IA value calculated by using the Cohen-Kurath shell model. This discrepancy cannot explain without the evidence of the meson-exchange current. Moreover, the present value is even larger by $25 \pm 4\%$ than the the recent theoretical value, which was calculated by using the Paris potential and includes the meson-exchange effects and the first and higher-order core polarization effects. It can be concluded from these facts that the present experiment results of the alignment-correlation coefficients definitely indicate the strong meson-exchange effect in the time component of the weak nuclear axial vector currents. However, more evaluate discussions on the meson-exchange current, more accurate theoretical calculations of the core polarization are required.

On the other hand, the difference of the coefficients $\alpha_\mp$ gives a limit $f_{\rm T}/f_{\rm W} = 0.04 \pm 0.11$ to the G-parity conservation law.

Acknowledgements

The author wishes to extend his thanks to all of those who have helped to make this work successful:

Professor T. Minamisono for his proposing the present experiment, providing earnest guidance during the work, and discussing the thesis.

Associate Professor Y. Nojiri for his constant collaboration, discussions, and encouragement.

Research Associate K. Matsuta for his constant collaboration, discussions and encouragement.

Research Associate M. Fukuda for his collaboration in during the later stage of the present work and for discussions concerning the thesis.

Professor M. Morita for his studies, which stimulated the present experiment and for discussions concerning the theory of beta decay.

Associate Professor K. Koshigiri for his studies, which included the theoretical calculation, and for discussions concerning the theory of beta decay.

Professor K. Katori, Professor Y. Nagashima, and Professor H. Ohtsubo for giving their valuable suggestions.

Mr. Y. Takahashi for his technical supports during the present experiment and for operating the Van de Graaff Accelerator.

Mr. M. Sakamoto for his technical supports during the present experiment and for developing the experimental setup.

Y. Takahashi, Y. Matsuo, I. Minami, Y. Someda, T. Araki, and K. Matsuda, all students, for their collaboration over a period of many years.

Professor Y. Hirao and Dr. S. Yamada for their continuous encouragements.

Contents

List of Figures

List of Tables

Chapter 1

Introduction

The weak interaction, that causes nuclear beta decay, and the electromagnetic interaction were described in the unified theory by Weinberg and Salam [1]. In the Weinberg-Salam model $W^{\pm}$, W^0, and Z^0 bosons mediate the weak interaction in the some way as photons do in the electromagnetic interaction. These $W^{\pm}$ bosons were discovered in 1983 in an experiment of the proton-antiproton collisions at CERN [2]. The Z^0 boson was also discovered. The experimental results show that the masses of the bosons are heavy enough to explain the short range of the weak interaction. Since the masses of the intermediate bosons are sufficiently larger than the momentum transfer in the nuclear beta decay, the weak interaction can be well described by the product of the hadronic and leptonic currents.

Then the weak interaction Hamiltonian is given as the product of the hadronic current (J_λ) and the leptonic current (ℓ_λ):

$$H = \sqrt{\frac{1}{2}} G[J_\lambda \ell_\lambda + h.c.], \tag{1.1}$$

where G is the Fermi coupling constant and $h.c.$ stands for the Hermitian conjugate. Gen-

erally Hamiltonian of the weak interaction includes also the strangeness-changing part and the lepton-lepton interaction part [3], which are omitted here. In the weak interaction, since parity violation is at its maximum, the leptonic current is the direct sum of the vector and axial vector terms with the same weight,

$$\ell_\lambda = i\overline{\psi_e}\gamma_\lambda(1+\gamma_5)\psi_\nu. \tag{1.2}$$

The hadronic current has a same structure and can be described also as a sum of the vector term (V_λ) and the axial vector term (A_λ),

$$J_\lambda = V_\lambda + A_\lambda. \tag{1.3}$$

Regarding the actual hadronic current, however, other terms arising from the strong interaction between hadrons and mesons must be taken into account. This can be done by adding many-body terms to the one-body term for the hadronic current, as follows:

$$J_\lambda(\boldsymbol{r}) = \sum_{i=1}^{A} J_\lambda(i) + \sum_{i,j=1}^{A} J_\lambda(i,j) + \epsilon. \tag{1.4}$$

Here, the first and second terms are the one-body and the two-body terms; the others are the many-body terms. We can obtain simple results by taking only the first term. This is called the 'impulse approximation'. The second term is a two-body current in which the nucleon exchanges mesons with another nucleon through the interaction shown in Fig. (1.1), and is referred to as "meson-exchange currents". The third term (ϵ) is very small. The history of meson-exchange currents started as Yukawa's meson theory [4]. At first, the effect of meson-exchange currents was considered on the magnetic moment of ^{3}H and ^{3}He [5, 6]. The theoretical calculation was carried out using a model-independent description in terms of soft-pion theorems [7].

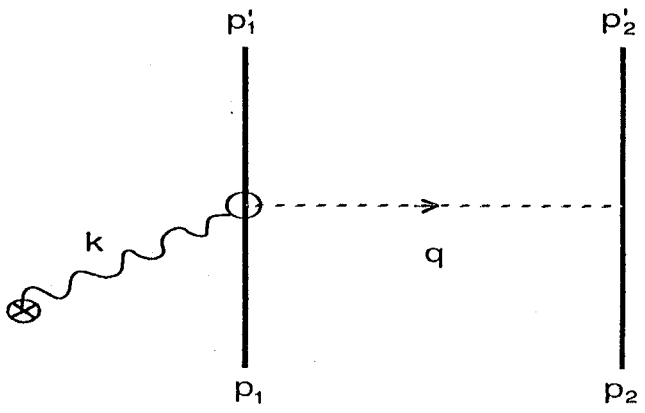

Figure 1.1: Feynman diagram of the two-body pion-exchange current.

In the nuclear beta decay, Kubodera, Delorme, and Rho (KDR) suggested that clear evidence for the meson-exchange effect can be found in the axial current, and then proposed a possible experimental test [8]. They pointed out that the one-pion exchange process is dominant over other shorter range processes, such as multipion or heavier meson exchanges. The soft-pion theorem was therefore applied to the axial current.

It can be shown that the exchange currents have a large amplitude ($O(1)$) in the time component of the axial vector current; the impulse term has a small magnitude ($O(\frac{p}{M})$). KDR estimated that the matrix element of the one-body current is enhanced by about 40% by the exchange current in the case of the mass A=12 system. The amplitude of the pion emission for the Feynman diagram given in Fig. (1.1) is described as the sum of the 'commutator term', the 'PCAC consistency term' and the 'Born term'. Part of the 'Born term' is taken into account in the wave function. The remainder of the 'Born term' is, however, cancelled out by the 'PCAC consistency term'. As a result, the amplitude of pion emission can be described using only the 'commutator term'. From current algebra, the

commutator is, thus, given as follows:

$$[Q^5_\beta, V^\alpha_\lambda] = i\epsilon_{\alpha\beta\gamma} A^\gamma_\lambda \tag{1.5}$$

and

$$[Q^5_\beta, A^\alpha_\lambda] = i\epsilon_{\alpha\beta\gamma} V^\gamma_\lambda. \tag{1.6}$$

Here, the axial weak charge (Q^5_β) is defined as

$$Q^5_\beta = \int dx A^\beta_4, \tag{1.7}$$

where α, β and γ are the isospin indices of the two-body, pion and one-body currents; $\epsilon_{\alpha\beta\gamma}$ is a completely antisymmetric tensor of the isospin indices. In a nonrelativistic approximation, the magnitude of the main term (γ_λ) of the vector currents is $O(\frac{p}{M})$ for the space component ($\lambda = 1 \sim 3$) and $O(1)$ for the time component ($\lambda = 4$). On the other hand, the magnitude of the main term ($\gamma_\lambda\gamma_5$) of the axial vector currents is $O(1)$ for the space component and $O(\frac{p}{M})$ for the time component. From the commutator relations, Eq.(1.5) and (1.6), the term due to meson-exchange currents has an opposite contribution to that of the impulse term. Table (1.1) shows the order of such currents without any coupling constants. In the case of photo-pion production, the space component has a large-magnitude $O(1)$, thus making leaving the time component small ($O(\frac{p}{M})$). On the other hand, in the case of weak-pion production, the time component has a large-magnitude $O(1)$ and the space component is small, $O(\frac{p}{M})$, for the axial vector term. We therefore obtain information concerning the meson exchange current enhanced in the time component of the axial vector current.

	space component $\lambda = 1 \sim 3$	time component $\lambda = 4$
V_λ^{IA}	$O(\frac{p}{M})$	$O(1)$
V_λ^{MEC}	$O(1)$	$O(\frac{p}{M})$
A_λ^{IA}	$O(1)$	$O(\frac{p}{M})$
A_λ^{MEC}	$O(\frac{p}{M})$	$O(1)$

Table 1.1: Amplitudes of the impulse (approximation) term and the meson exchange currents. The coupling constants are neglected in these terms.

KDR also pointed out that the decay rates in the $0^+ \rightarrow 0^-$ as well as $0^- \rightarrow 0^+$ transitions are a potential source of information concerning the time component. The mesonic effects increase the beta-decay rate of the $^{16}\mathrm{N}(0^-) \rightarrow ^{16}\mathrm{O}(0^+) + e^+ + \nu$ interaction by a factor of 2 or more. In the experiment, however, it is difficult to separate out only the time component from the induced pseudo scalar current. Additional theoretical studies concerning this subject are presented in references [9, 10, 11]. Many experiments have been carried out concerning the $0^- \rightarrow 0^+$ beta decay [12, 13, 14, 15]. The results, however, contain large uncertainties due to this circumstance.

Beta decay in the mass A=12 system has provided an excellent testing ground for the weak interaction. The ground states of $^{12}\mathrm{B}(1^+$:Gnd.) and $^{12}\mathrm{N}(1^+$:Gnd.) constitute an isotriplet($T = 1$) with an excited state of $^{12}\mathrm{C}(1^+$:15MeV) and decay to the ground state of $^{12}\mathrm{C}(I^\pi = 0^+, T = 0)$ (See Fig. (1.2)). The beta decays represent pure Gamow-Teller transitions. Morita studied the beta-ray energy spectra in the mass A=12 system and

described the spectra as being a sum of the weak magnetism term (whose sign changes with the sign of the beta decay) and the main term (whose sign does not change) [16].

$$P(E) \propto pE(E_0 - E)^2 \left(1 \pm \frac{8}{3}aE\right) \qquad \text{for } \beta^{\mp} \tag{1.8}$$

Thus, the Conserved Vector Current hypothesis (CVC) can be tested by observing the beta-ray spectra of ^{12}B and ^{12}N. The Colombia group (Wu *et al.*), and later the Heidelberg group, observed these spectra [17, 18, 19]. Their results agree with the theoretical prediction from the CVC hypothesis.

The term which depends on the nuclear structure can be canceled by comparing the beta-ray angular distributions from oriented ^{12}B and ^{12}N nuclei; it has played the most important role in testing concerning the G-parity conservation law. Here, the G-parity operator is defined as a product of the charge conjugate and the 180° rotation about the iso-y axis:

$$G = C \exp(i\pi I_y). \tag{1.9}$$

Weinberg classified the weak nucleon currents in terms of their G-parities, and named the currents which violate G-parity second-class currents (SCC) [20]. Both the polarization-correlation coefficient and the alignment-correlation coefficient are described as a sum of the weak-interaction term and the nuclear structure-dependent term. The weak-interaction term, which comprises of the SCC term (f_{T}) and the weak magnetism term (a) changes sign with the sign of beta decay. On the other hand, since the nuclear structure-dependent term, namely the nuclear parameter (y) defined by the ratio of the time component of the axial vector current to the Gamow-Teller matrix element, does not depend on the sign of

beta decay, a and f_T can be extracted by a comparison of the correlation coefficients in both $\beta^{\pm}$ decays.

The Osaka group (Sugimoto *et al.*) measured the angular distributions of the beta-ray spectra from polarized ^{12}B and ^{12}N in order to determine the SCC term [21]. Since the weak magnetism term in the A=12 system had already been determined in the test experiments of the CVC theory, the f_T term was obtained from the difference of two correlation coefficients. However, the experimental results from the polarization correlation terms contained large experimental errors caused by beta-ray scattering. To prevent this problem, the Osaka group (Minamisono *et al.*) measured the distributions from aligned ^{12}B and ^{12}N nuclei with zero polarization [22]. Later, Grenacs *et al.* also carried out the same type of experiment [23], but with finite polarization. Since the alignment correlation term is less sensitive to beta-ray scattering, a clear limitation of the second-class current was obtained [22, 24]. In this most sensitive test the G-parity conservation law was confirmed at the 20% level of the weak magnetism term.

On the other hand, the nuclear parameter (y) can also be isolated from the sum of the same coefficients. The result given by Minamisono *et al.* showed that the time component was very close to the theoretical calculation from the impulse approximation (IA), and was not enhanced as is predicted by KDR. This result was explained later by Koshigiri *et al.*. They pointed out that the effect of first-order core polarization is as large as the effect of the meson exchange currents in absolute magnitude but with opposite sign. The core polarization thus canceled the enhancement due to the meson exchange currents. The theoretical value agreed with the experimental value very well.

For these correlation-type experiments, the nuclear magnetic resonance (NMR) tech-

nique is indispensable for manipulating the spin-ensemble. ^{12}B and ^{12}N nuclei (with spin $I = 1$) were implanted into a Mg single crystal in which the electric field gradient (q) is available for spin manipulation. The energy levels of magnetic substates $m = -1, 0, +1$ under an external magnetic field of H_0 are given by the magnetic dipole interaction (μH_0) and the electric quadrupole interaction (eqQ). Each transition is therefore separated from all other transitions, and it is possible to manipulate the substate populations selectively by using selected RF transitions.

What we measure is the product of the energy-dependent coefficient and the spin alignment. This means that the spin polarization must be measured to high precision. Therefore, for more accurate measurements of the correlation coefficients, we must study the hyperfine interactions of ^{12}B and ^{12}N in Mg single crystals in order to develop a new way of spin manipulation. The reason for this study was that, from observations of the NMR-line widths due to dipolar broadening, we already knew that the final sites of ^{12}B and ^{12}N are the interstitial sites in Mg [26], and that a small fraction of the ^{12}B or ^{12}N are located at other sites, *i.e.*, the minority of ^{12}B or ^{12}N nuclei sit in other final sites where they are exposed to different electric field gradients. Since this fraction prevents us from determining an accurate value for the alignment, the quadruple interaction, the final sites must definitely be studied. The ^{12}B or ^{12}N nuclei at the two sites must be manipulated independently. For this purpose, we developed a new spin-ensemble-control technique in which the spins of the majority and minority are both independently manipulated in order to accurately determine the degree of alignment.

We also needed to measure the energy of the beta ray. Since the energy scales were determined from fitting theoretical functions to the observed beta-ray energy-spectra from

previous experiments, the energy scale was ambiguous. This was due to a distortion of the spectra caused by beta-ray scattering. In the present improved method, the beta-ray energies were therefore calibrated in independent runs by detecting the end points of the energy spectra of several well-known beta emitters. Details concerning these experimental improvements are described in Chapters 3 and 4.

In the present experiment, the time component of the axial vector currents was compared with the theoretical values given in the frame work of the impulse approximation studied by Koshigiri *et al.*, who recalculated the time component in terms of the higher order terms of the core polarization [27, 33]. These results concerning the differences of the correlation coefficients are discussed in Chapter 5.2. The stricter limitation on the existence of SCC are given by the present coefficients. We also discuss the G-parity conservation law at the 11% level of the weak magnetism term, as will be discussed in Chapter 5.3.1.

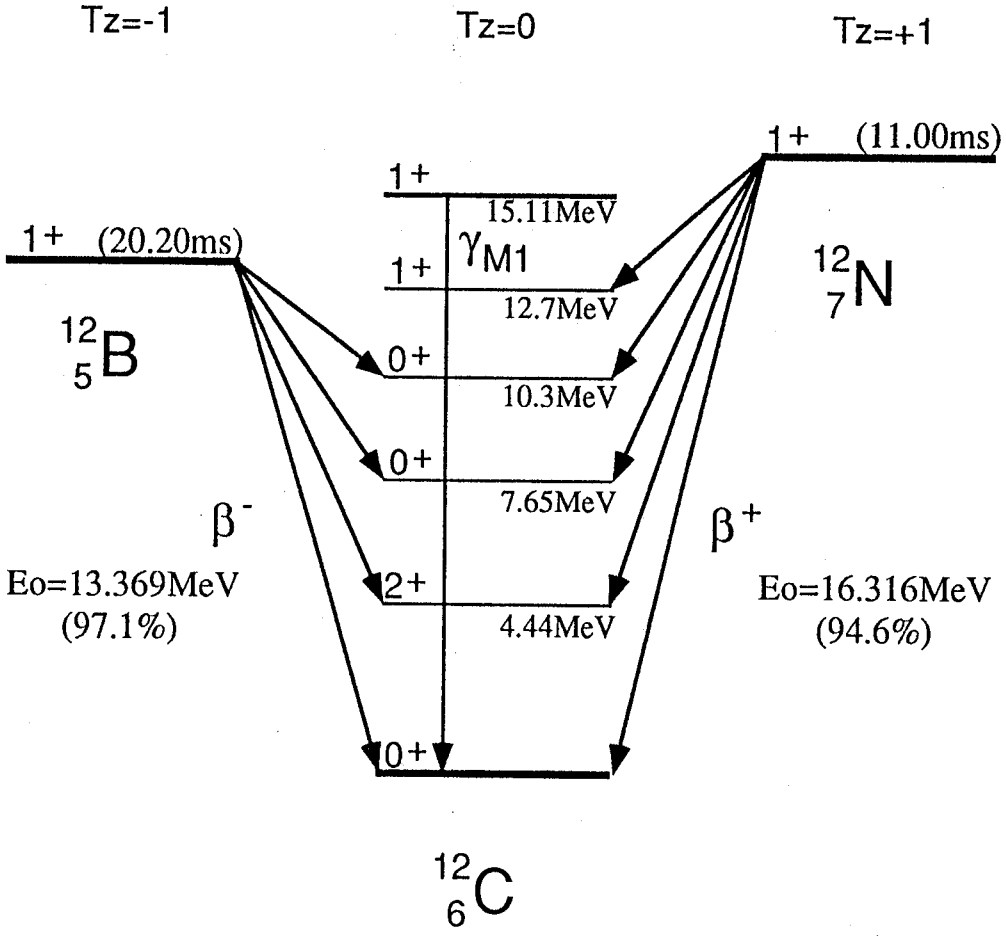

Figure 1.2: Decay of the isospin triplet ($T = 1$) to the goround state of ^{12}C in a mass A=12 system.

Table 1.2: Decay properties of ^{12}B and ^{12}N in the A=12 system.

	^{12}B		^{12}N	
Spin I^{π}	1^+		1^+	
Half Life $t_{1/2}$ *)	20.41(6)	msec	10.97(4)	msec
To the ground state	13.369	MeV	16.316	MeV
	97.14±0.30	%	94.55±0.60	%
To the 4.439 MeV level	8.931	MeV	11.877	MeV
	1.28±0.04	%	1.90±0.03	%
To the 7.654 MeV level	5.716	MeV	8.662	MeV
	1.5±0.3	%	2.7±0.4	%
To the 10.3 MeV level	3.1	MeV	6.0	MeV
	0.08±0.02	%	0.46±0.15	%
To the 12.710 MeV level			3.606	MeV
			0.29±0.13	%

*) F. Ajzenberg-Selove Nucl. Phys. A433 (1985) 1

Chapter 2

Theory of Nuclear Beta-Decay

2.1 Interaction Hamiltonian

Accurate calculations of beta decay in the mass A=12 system were obtained by Morita and Koshigiri, *et al.*[25, 28]. The interaction Hamiltonian density for nuclear beta decay can be described as a current-current interaction,

$$H_{\rm I}(\boldsymbol{r}) = \sqrt{\frac{1}{2}} G[J_\lambda(\boldsymbol{r})\ell_\lambda(\boldsymbol{r}) + h.c.]. \tag{2.1}$$

Here, G is the Fermi coupling constant, and is given by

$$G = (2.9954 \pm 0.0009) \times 10^{-12}\hbar/m_e^2 c. \tag{2.2}$$

The lepton currents ($\ell_\lambda(\boldsymbol{r})$) are given with a parity non-conserving part as

$$\ell_\lambda(\boldsymbol{r}) = -i\overline{\psi_e}(\boldsymbol{r})\gamma_\lambda(1+\gamma_5)\psi_\nu(\boldsymbol{r}). \tag{2.3}$$

The hadron currents for the nucleons are generally expressed as follows with the condition of invariance under the proper Lorentz transformation:

$$J_\lambda(\boldsymbol{r}) \;=\; V_\lambda(\boldsymbol{r}) + A_\lambda(\boldsymbol{r}), \tag{2.4}$$

$$V_\lambda = \overline{\psi}_{\rm p}(f_{\rm V}\gamma_\lambda + f_{\rm W}\sigma_{\lambda\rho}k_\rho + if_{\rm S}k_\lambda)\psi_{\rm n}, \tag{2.5}$$

$$A_\lambda = \overline{\psi}_{\rm p}\gamma_5(f_{\rm A}\gamma_\lambda + f_{\rm T}\sigma_{\lambda\rho}k_\rho + if_{\rm P}k_\lambda)\psi_{\rm n}, \tag{2.6}$$

with

$$k = p_{\rm n} - p_{\rm p} \tag{2.7}$$

and

$$\sigma_{\lambda\rho} = \frac{[\gamma_\lambda, \gamma_\rho]}{2i}. \tag{2.8}$$

The form factors (f_i) depend on the square of the momentum transfer (k). However, since k^2 is very small, the f_i are assumed to be constant in the case of beta decay. If the Hamiltonian is invariant under the time-reversal (f_i) are also real. $f_{\rm V}$, $f_{\rm W}$, $f_{\rm S}$, $f_{\rm A}$, $f_{\rm T}$, and $f_{\rm P}$ have been named vector, weak magnetism, induced scalar, axial vector, induced tensor, and induced pseudo scalar.

The effective Hamiltonian is formed by replacing the lepton part by its matrix element, $L_\lambda(\boldsymbol{r})$, as follows:

$$H_{\rm I} = \frac{G}{\sqrt{2}}\int J_\lambda(\boldsymbol{r})L_\lambda(\boldsymbol{r})d\boldsymbol{r}, \tag{2.9}$$

with

$$\begin{aligned} L_\lambda(\boldsymbol{r}) &= \langle e\overline{\nu}_e|\ell_\lambda(\boldsymbol{r})|0\rangle \\ &= -i\overline{\psi}^e_{S_e}(\boldsymbol{r})\gamma_\lambda(1+\gamma_5)\psi^\nu_{S_\nu}(\boldsymbol{r}) \end{aligned} \tag{2.10}$$

$$\tag{2.11}$$

and

$$J_\lambda(\boldsymbol{r}) = V_\lambda(\boldsymbol{r}) + A_\lambda(\boldsymbol{r}) \tag{2.12}$$

for β^- decay. Here, $\psi^e_{S_e}$ and $\psi^\nu_{S_\nu}$ are the wave functions for the electron and antineutrino.

In Eq. (2.9) the wave function can be expanded into a series of partial waves as

$$\psi^e_{S_e}(\boldsymbol{r}) = 4\pi \sum_{\kappa_e m_e \mu_e} i^{\ell_e}(\ell_e m_e \frac{1}{2} S_e | j_e \mu_e) \boldsymbol{Y}^*_{\ell_e m_e}(\hat{\boldsymbol{p}}) \begin{pmatrix} G_{\kappa_e} \chi_{\kappa_e \mu_e} \\ iF_{\kappa_e} \chi_{-\kappa_e \mu_e} \end{pmatrix} \tag{2.13}$$

and

$$\psi^\nu_{S_\nu}(\boldsymbol{r}) = \frac{4\pi}{\sqrt{2}} \sum_{\kappa_\nu m_\nu \mu_\nu} i^{\ell_\nu}(\ell_\nu m_\nu \frac{1}{2} S_\nu | j_\nu \mu_\nu) \boldsymbol{Y}^*_{\ell_\nu m_\nu}(\hat{\boldsymbol{q}}) \begin{pmatrix} f_{\kappa_\nu} \chi_{-\kappa_\nu \mu_\nu} \\ ig_{\kappa_\nu} \chi_{\kappa_\nu \mu_\nu} \end{pmatrix}. \tag{2.14}$$

Here, $\boldsymbol{p}$, $\boldsymbol{q}$ are the momenta of electron and antineutrino; ℓ, m are the orbital angular momentum and its z-component; j, μ are the total angular momentum and its z-component. κ is a quantum number defined as

$$\begin{aligned} j_\kappa &= |\kappa| - \frac{1}{2}, \\ \ell_\kappa &= \begin{cases} \kappa & (\kappa > 0) \\ -(\kappa+1) & (\kappa < 0) \end{cases}, \\ S_\kappa &= \frac{\kappa}{|\kappa|}, \\ \bar{\ell}_\kappa &= \ell_{-\kappa} = \ell_\kappa - S_\kappa. \end{aligned} \tag{2.15}$$

f_κ and g_κ are the radial wave functions for the antineutrino, and F_κ and G_κ are the radial wave functions included the Coulomb phase shift for the electron. χ is the spin angular function defined as

$$\chi_{\kappa\mu} = \sum_{ms} (\ell_\kappa m \frac{1}{2} s | j_\kappa \mu) \boldsymbol{Y}_{\ell_\kappa m}(\hat{\boldsymbol{r}}) \chi_s \tag{2.16}$$

with

$$\chi_{1/2} = \begin{pmatrix} 1 \\ 0 \end{pmatrix}, \qquad \chi_{-1/2} = \begin{pmatrix} 0 \\ 1 \end{pmatrix}. \tag{2.17}$$

The nuclear currents operators (V_λ and A_λ) are written in terms of the space and time components, as follows:

$$V_\lambda(\boldsymbol{r}) = (\boldsymbol{J}^V, i\rho^V(\boldsymbol{r})) \tag{2.18}$$

and

$$A_\lambda(\boldsymbol{r}) = (\boldsymbol{J}^A, i\rho^A(\boldsymbol{r})). \tag{2.19}$$

The effective Hamiltonian can thus be expanded in terms of the Hamiltonian operator (Ξ_{JLM}) corresponding to the lepton system of the total angular momentum (J), z-component (M), and orbital angular momentum (L) as follows:

$$\begin{aligned} H_{\rm I} &= \frac{1}{2}G(4\pi)^{\frac{3}{2}} \sum_{\substack{\kappa_e,\kappa_\nu,L \\ \kappa'_e,\kappa'_\nu,L'}} i^{-\ell_e-\ell_\nu}(\ell_e \tfrac{1}{2} m_e s_e|j_e\mu_e)(-)^{\mu_e-\frac{1}{2}}\boldsymbol{Y}_{\ell_e m_e}(\hat{\boldsymbol{p}}) \\ &\quad \times[(\ell_\nu \tfrac{1}{2} m_\nu - s_\nu|j_\nu\mu_\nu)\boldsymbol{Y}^*_{\ell_\nu m_\nu}(\hat{\boldsymbol{q}}) \pm (\bar{\ell}_\nu \tfrac{1}{2} m_\nu - s_\nu|j_\nu\mu_\nu)\boldsymbol{Y}^*_{\ell_\nu m_\nu}(\hat{\boldsymbol{q}})] \\ &\quad \times \sum_{J,L,M}(j_e j_\nu - \mu_e\mu_\nu|JM)\Xi_{JLM}(\kappa_e,\kappa_\nu). \end{aligned} \tag{2.20}$$

Here,

$$\begin{aligned} &\Xi_{JLM}(\kappa_e,\kappa_\nu) \\ &= \sqrt{4\pi}\int d\boldsymbol{r} \times \\ &\quad \{\pm\rho^V(\boldsymbol{r})Y_{JM}(\hat{\boldsymbol{r}})[G_{\kappa_e}g_{\kappa_\nu}S_{0JJ}(\kappa_e,\kappa_\nu) - F_{\kappa_e}f_{\kappa_\nu}S_{0JJ}(-\kappa_e,-\kappa_\nu)] \\ &\quad \mp\boldsymbol{J}^V(\boldsymbol{r})\boldsymbol{Y}^M_{JL1}(\hat{\boldsymbol{r}})[G_{\kappa_e}f_{\kappa_\nu}S_{1LJ}(\kappa_e,-\kappa_\nu) - F_{\kappa_e}g_{\kappa_\nu}S_{1LJ}(-\kappa_e,\kappa_\nu)] \\ &\quad +\boldsymbol{J}^A(\boldsymbol{r})\boldsymbol{Y}^M_{JL1}(\hat{\boldsymbol{r}})[G_{\kappa_e}g_{\kappa_\nu}S_{1LJ}(\kappa_e,\kappa_\nu) - F_{\kappa_e}f_{\kappa_\nu}S_{1LJ}(-\kappa_e,-\kappa_\nu)] \\ &\quad -i\rho^A(\boldsymbol{r})Y_{JM}(\hat{\boldsymbol{r}})[G_{\kappa_e}f_{\kappa_\nu}S_{0JJ}(\kappa_e,-\kappa_\nu) - F_{\kappa_e}g_{\kappa_\nu}S_{0JJ}(-\kappa_e,\kappa_\nu)]\}, \end{aligned} \tag{2.21}$$

with

$$S_{KLJ}(\kappa_1,\kappa_2) = \sqrt{2\cdot[\ell_1,\ell_2,j_1,j_2]}(\ell_1 0 \ell_2 0|L0)\begin{Bmatrix} \ell_1 & \ell_2 & L \\ j_1 & j_2 & J \\ 1/2 & 1/2 & \kappa \end{Bmatrix}. \tag{2.22}$$

The last line in Eq. (2.21) is the time component term in which we are interested.

2.2 Impulse Approximation

If we assume that the nuclear currents can be expressed as the sum of individual nucleon currents under the nonrelativistic approximation, the weak nuclear current densities are described as follows:

$$\begin{aligned}
\rho^V_{\rm IA} &= \sum_{j=1}^{A}\delta(\boldsymbol{r}-\boldsymbol{r}_j)\tau_j^{\pm}\left[f_{\rm V}\pm E_0 f_{\rm S}1\right]_j, \\
\boldsymbol{J}^V_{\rm IA} &= \sum_{j=1}^{A}\delta(\boldsymbol{r}-\boldsymbol{r}_j)\tau_j^{\pm}\left[f_{\rm V}\frac{\boldsymbol{p}}{2M}+(f_{\rm V}-2Mf_{\rm W})\frac{i\boldsymbol{\sigma}\times\boldsymbol{k}}{2M}\mp f_{\rm S}\boldsymbol{k}\right]_j, \\
\boldsymbol{J}^A_{\rm IA} &= \sum_{j=1}^{A}\delta(\boldsymbol{r}-\boldsymbol{r}_j)\tau_j^{\pm}\left[(f_{\rm A}\mp E_0 f_{\rm T})\boldsymbol{\sigma}-f_{\rm P}\frac{(\boldsymbol{\sigma}\cdot\boldsymbol{k})\boldsymbol{k}}{2M}\right]_j, \\
\rho^A_{\rm IA} &= \sum_{j=1}^{A}\delta(\boldsymbol{r}-\boldsymbol{r}_j)\tau_j^{\pm}\left[f_{\rm A}\frac{\boldsymbol{\sigma}\cdot\boldsymbol{p}}{2M}+(\pm 2Mf_{\rm T}+E_0 f_{\rm P})\frac{\boldsymbol{\sigma}\cdot\boldsymbol{k}}{2M}\right]_j,
\end{aligned} \tag{2.23}$$

with

$$\boldsymbol{p} = \boldsymbol{k}_f + \boldsymbol{k}_i \tag{2.24}$$

and

$$\boldsymbol{k} = \boldsymbol{k}_f - \boldsymbol{k}_i. \tag{2.25}$$

Here, $\boldsymbol{k}_f$ and $\boldsymbol{k}_i$ are the momentum operators on the nuclear wave functions in the initial and final nucleon states; $\boldsymbol{r}_j$ is the coordinate of each nucleon. We obtained from Eq. (2.23) an explicit description of the Hamiltonian operator in the impulse approximation,

2.3 Mesonic Enhancements of the Time Component

The one-pion exchange contribution to the two-nucleon current (J^α_λ) shown in Fig. (1.1) is given by the following transition matrix element, $\tilde{J}^\alpha_\lambda$:

$$\begin{aligned}
\tilde{J}^\alpha_\lambda &= (2\pi)^3\delta(\boldsymbol{p}_1+\boldsymbol{p}_2+\boldsymbol{k}-\boldsymbol{p}'_1-\boldsymbol{p}'_2)\langle p'_1p'_2|J_\lambda|p_1p_2\rangle \\
&= (2\pi)^3\delta(\boldsymbol{p}_1+\boldsymbol{p}_2+\boldsymbol{k}-\boldsymbol{p}'_1-\boldsymbol{p}'_2) \\
&\quad \left\{\langle\pi^\beta(q)N(p'_1)|J^\alpha_\lambda|N(p_1)\rangle\frac{1}{q^2+m^2_\pi}\langle N(p'_2)|J^\beta_\pi|N(p_2)\rangle\right\}. \qquad (2.26)
\end{aligned}$$

Here, p_i, p'_i , q and k are the four momentum of the initial nucleon, the final nucleon and pion, and the momentum transfer induced by the external field; $\boldsymbol{p}_i$, $\boldsymbol{p}'_i$, $\mathbf{q}$ and $\mathbf{k}$ are their three momentum; α and β denote the isospin indices of the two-nucleon current and the pion; J^β_π is the pion source current. The pion production amplitude by the external field in Eq. (2.26) is expressed as follows using the soft-pion theorems:

$$\begin{aligned}
\langle\pi^\beta(q)N(p'_1)|J^\alpha_\lambda|N(p_1)\rangle &= i\bar{u}(p'_1)\left[\frac{g_r}{Mf_A}\tilde{J}^{\beta\alpha}_\lambda(k-q)-\frac{g_r}{2M}\{\gamma_5\tau_\beta,J^\alpha_\lambda(k)\}_+\right. \\
&\quad +g_r\gamma_5\tau_\beta\frac{-i\gamma(p'_1+q)+M}{(p'_1+q)^2+M^2}J^\alpha_\lambda(k) \\
&\quad \left.+J^\alpha_\lambda(k)\frac{-i\gamma(p_1-q)+M}{(p_1-q)^2+M^2}g_r\gamma_5\tau_\beta\right]u(p_1)\psi^*_\beta. \qquad (2.27)
\end{aligned}$$

Here, ψ^*_β is the isospin wave function of the pion,

$$\psi_i=\frac{1}{\sqrt{2}}\begin{pmatrix}1\\ \pm i\\ 0\end{pmatrix} \qquad \text{for } \pi^\pm \qquad (2.28)$$

and

$$\psi_i = \frac{1}{\sqrt{2}} \begin{pmatrix} 0 \\ 0 \\ 1 \end{pmatrix} \qquad \text{for } \pi^0. \tag{2.29}$$

$f_{\rm A}$ is the axial vector coupling constant for the one-nucleon current and g_r is the pion nucleon coupling constant. $J^\alpha_\lambda(k)$ and $\tilde{J}^{\beta\alpha}_\lambda(k)$ are defined as

$$\langle N(p_2)|J^\alpha_\lambda|N(p_1)\rangle = \bar{u}(p_2)J^\alpha_\lambda(p_2-p_1)u(p_1), \tag{2.30}$$

and

$$\langle N(p_2)|[Q^5_\beta, J^5_\lambda]|N(p_1)\rangle = \bar{u}(p_2)\tilde{J}^{\beta\alpha}_\lambda(p_2-p_1)u(p_1), \tag{2.31}$$

with an axial weak charge of

$$Q^5_\beta = \int d\boldsymbol{x} A^\beta_0(\boldsymbol{x},0). \tag{2.32}$$

The first term in Eq. (2.27) is known as the 'commutator term', the second is the 'PCAC consistency term' and the third is the 'Born term'. However part of the 'Born term' is taken into account in the nuclear wave function; the other part is compensated for by the 'PCAC consistency term'. Thus, only the commutator term remains:

$$\langle \pi^\beta(q)N(p'_1)|J^\alpha_\lambda|N(p_1)\rangle = i\frac{g_r}{Mf_{\rm A}}\langle N(p_1)|[Q^5_\beta, J^\alpha_\lambda]|N(p_2)\rangle. \tag{2.33}$$

From current algebra, the commutator is given by

$$[Q^5_\beta, A^\alpha_\lambda] = i\epsilon_{\alpha\beta\gamma}V^\gamma_\lambda. \tag{2.34}$$

From Eq. (2.33) and Eq. (2.34), the amplitude of the pion emission is given by

$$\langle \pi^\beta(q)N(p'_1)|J^\alpha_4|N(p_1)\rangle = i\frac{g_r}{Mf_{\rm A}}\epsilon_{\alpha\beta\gamma}\tau^\gamma_1. \tag{2.35}$$

The pion source current is

$$\langle N(p_2')|J_\pi^\beta|N(p_2)\rangle = ig_r\frac{\boldsymbol{\sigma}\cdot\boldsymbol{q}}{2M}\tau_2^\beta. \tag{2.36}$$

By combining Eq. (2.27) and Eq. (2.36) with Eq. (2.26) the following transition matrix element in the nonrelativistic limit is obtained:

$$\begin{aligned}\tilde{J}_4^\alpha &= \frac{1}{(2\pi)^3}\delta^3(\boldsymbol{p}_1+\boldsymbol{p}_1'+\boldsymbol{k}-\boldsymbol{p}_2-\boldsymbol{p}_2')\frac{g_r}{Mf_{\rm A}}\frac{1}{\boldsymbol{q}^2+m_\pi^2}\frac{\boldsymbol{\sigma}_2\cdot\boldsymbol{q}}{2M}(\boldsymbol{\tau}_1\times\boldsymbol{\tau}_2)^\alpha \\ &\equiv i\rho_{\rm MEC}^{\rm A}{}^{\alpha}(\boldsymbol{x}_1,\boldsymbol{x}_2).\end{aligned} \tag{2.37}$$

The defined $\rho_{\rm MEC}^A(\boldsymbol{x}_1,\boldsymbol{x}_2)$ is the contribution of the exchange current to the axial vector charge in Fig. 1.1. The total $\rho^A(\boldsymbol{r})$ is the sum of $\rho_{\rm MEC}^A$ and the impulse approximation term $\rho_{\rm IA}^{\rm A}$,

$$\rho_{\rm MEC}^A \equiv \delta(\boldsymbol{r}-\boldsymbol{x}_1)\rho_{\rm MEC}^{\rm A}{}^{1\pm i2}(\boldsymbol{x}_1,\boldsymbol{x}_2)+\delta(\boldsymbol{r}-\boldsymbol{x}_2)\rho_{\rm MEC}^{\rm A}{}^{1\pm i2}(\boldsymbol{x}_1,\boldsymbol{x}_2) \tag{2.38}$$

and

$$\rho^A(\boldsymbol{r}) = \rho_{\rm IA}^A(\boldsymbol{r})+\rho_{\rm MEC}^A(\boldsymbol{r}). \tag{2.39}$$

The meson exchange current contributes to the effective Hamiltonian as a form of $\rho^A Y_J$ given in Eq. (2.21).

2.4 Beta-ray Angular Distributions from Oriented ^{12}B and ^{12}N

The probability of beta-ray emission with an energy between E and $E+dE$ within the solid angle $d\Omega_e$ is given by

$$dP = \frac{1}{(2\pi)^5} pE(E_0 - E)^2 \sum_{Mi} \rho_{M_i' M_i} a_{M_i} dE d\Omega_e \tag{2.40}$$

Here, the density matrix is defined as the absolute square of the transition amplitude from the nuclear state (J_i, M_i) to the state (J_f, M_f), averaged over the z-components of the leptons as well as the final nuclear spin states,

$$\rho_{M_i' M_i} \equiv \sum_{s_e, s_\nu, M_f} \int d\Omega_\nu \langle J_f M_f | H_{\rm I} | J_i M_i \rangle \langle J_f M_f | H_{\rm I} | J_i M_i' \rangle^* \times \frac{1 + 3E - E_0 - 3\boldsymbol{p}\cdot\boldsymbol{q}}{12M}. \tag{2.41}$$

The initial nuclear spin states (a_{M_i}) are the populations of the initial magnetic substate (M_i); they are normalized as

$$\sum_{M_i} a_{M_i} = 1. \tag{2.42}$$

From Eqs. (2.20),(2.40) and (2.41) the beta-ray angular distribution from oriented nuclei can be described without any restrictions on the nuclear currents as

$$\begin{aligned} \frac{dP}{dE d\Omega_e} &= \frac{G^2}{(2\pi)^4} pE(E_0 - E)^2 \sum_{\ell, J, J', k} \sqrt{2J_i + 1}\, \hat{f}_\ell(J_i) P_\ell(\cos\theta_e) \\ &\quad \times (-)^{J_f - J_i + J + J' + \ell} W(J_i J_i J J'; \ell J f) b^{(\ell)}_{JJ'}(k), \end{aligned} \tag{2.43}$$

with

$$\hat{f}_\ell(J_i) = \sum_{M_i} \sqrt{2J_i + 1} (-)^{j_i - M_i} (J_i J_i M_i - M_i | \ell 0) a_{M_i}. \tag{2.44}$$

Here, θ_e is the direction of the electron momentum with respect to the nuclear orientation axis; $P_\ell(\cos\theta)$ are Legendre polynomials. If the recoil correction is neglected, the particle parameters $(b^{(\ell)}_{JJ'}(k))$ for $k = 0$ are

$$\begin{aligned} b^{(\ell)}_{JJ'} &= \sum_{\substack{\kappa_e, \kappa_\nu, L \\ \kappa_e', \kappa_\nu', L'}} \frac{1}{2J_i + 1} i^{\ell_e' - \ell_e} (-)^{j_\nu - \frac{1}{2}} (j_e \tfrac{1}{2} j_e' - \tfrac{1}{2} | \ell 0) \\ &\quad \times W(j_e j_e' J J'; \ell j_\nu) [\delta_{\kappa_\nu, \kappa_\nu'} \mp i S_{\kappa_\nu} \delta_{\kappa_\nu, -\kappa_\nu'}] \end{aligned}$$

$$\times\sqrt{(2j_e+1)(2j'_e+1)(2J+1)(2J'+1)}$$

$$\times\langle J_f\|\Xi_{JL}(\kappa_e,\kappa_\nu)\|J_i\rangle\langle J_f\|\Xi_{J'L'}(\kappa'_e,\kappa'_\nu)\|J_i\rangle^*. \tag{2.45}$$

The reduced matrix element is defined by

$$\langle J_fM_f|\Xi_{JLM}|J_iM_i\rangle = \frac{1}{\sqrt{2J_f+1}}(J_iJM_iM|J_fM_f)\langle J_f\|\Xi\|J_i\rangle. \tag{2.46}$$

In the case that the ^{12}B and ^{12}N decay into the ground state of ^{12}C, the transitions are $1^+ \to 0^+$. Therefore, $J = 1$ and $L = 0 \sim 2$. The Hamiltonian operator can thus be described as

$$\begin{aligned}
&\sum_L \Xi_{1LM}(\kappa_e,\kappa_\nu) \\
&= \frac{2}{3}\sqrt{4\pi}\sqrt{|\kappa_e\kappa_\nu|}(j_e\tfrac{1}{2}j_\nu-\tfrac{1}{2}|10)\int d\boldsymbol{r}\times \\
&\quad \{i\boldsymbol{J}^A[(\boldsymbol{Y}^M_{101}(\boldsymbol{r})-\sqrt{2}\boldsymbol{Y}^M_{121}(\boldsymbol{r}))L^- - \kappa(\boldsymbol{Y}^M_{101}(\boldsymbol{r})+\frac{1}{\sqrt{2}}\boldsymbol{Y}^M_{121}(\boldsymbol{r}))L^+] \\
&\quad \pm i\boldsymbol{J}^V\boldsymbol{Y}^M_{111}(\boldsymbol{r})\sqrt{\frac{3}{2}}\kappa\mathcal{L}^+ \\
&\quad -i\rho^A Y_{1M}(\boldsymbol{r})3\mathcal{L}^-\},
\end{aligned} \tag{2.47}$$

with

$$\kappa = \kappa_e + \kappa_\nu. \tag{2.48}$$

Here, combinations of the product of the lepton wave functions are defined by

$$L^\pm = G_{\kappa_e}g_{\kappa_\nu} \pm F_{\kappa_e}f_{\kappa_\nu} \tag{2.49}$$

and

$$\mathcal{L}^\pm = G_{\kappa_e}f_{\kappa_\nu} \pm F_{\kappa_e}g_{\kappa_\nu}. \tag{2.50}$$

2.4.1 Impulse approximation

The beta-ray angular distribution is given by substituting Eqs. (2.23) and (2.47) for Eq. (2.43). By approximating the electron and neutrino wave functions, the angular distribution can be simply described as a sum of the main term, the polarization term and the alignment term as follows:

$$\begin{aligned} W(E,\theta) &= \text{const.} \times g_{\mathrm{A}}^2\langle\sigma\rangle pE(E_0-E)^2 \\ &\quad \times F(\pm Z,E)(1+R(E,E_0))\left(1\mp\frac{8}{3}aE\right) \\ &\quad \times[1\mp P(p/E)(1+\alpha_{\mp}E)\mathtt{P}_1(\cos\theta)+A\alpha_{\mp}E\mathtt{P}_2(\cos\theta)], \end{aligned} \tag{2.51}$$

where, E and p are the total energy and momentum of the beta ray and E_0 is the end-point energy; $F(\pm Z,E)$ is Fermi function for the Coulomb correction and $R(E,E_0)$ is the radiative correction; θ is the polar angle between the electron momentum and the quantization axis of the nuclear spin polarization. P and A are the polarization and alignment defined in terms of the magnetic substate populations (a_m), as follows, for spin $I=1$:

$$P \equiv a_{+1} - a_{-1} \tag{2.52}$$

and

$$A \equiv 1 - 3a_0. \tag{2.53}$$

$\mathtt{P}_1(\cos\theta)$ and $\mathtt{P}_2(\cos\theta)$ are Legendre polynomials.

The coefficients $\alpha_{\mp}$ are defined as follows:

$$\alpha_{\mp} = \pm\frac{2}{3}(a-b), \tag{2.54}$$

with

$$a = Re\left(\frac{g_{\rm W}}{g_{\rm A}}\right) \tag{2.55}$$

and

$$b = Re\left(\frac{g_{\rm T}}{g_{\rm A}}\right) \tag{2.56}$$

Here, the effective coupling constants (g) are given in terms of the coupling constants (f) for a free nucleon as follows:

$$g_{\rm A} = f_{\rm A} \mp E_0 f_{\rm T}, \tag{2.57}$$

$$\begin{aligned} g_{\rm W} &= x(f_{\rm W} - f_{\rm V}/2M) \\ &= x[-(\mu_{\rm p} - \mu_{\rm n})f_{\rm V}/2M - f_{\rm V}/2M], \end{aligned} \tag{2.58}$$

and

$$g_{\rm T} = f_{\rm T} \pm y(f_{\rm A}/2M). \tag{2.59}$$

Here, the nuclear parameters (x and y) are defined under the nonrelativistic approximation as

$$x = 1 + \frac{1}{1 + \mu_{\rm p} - \mu_{\rm n}} \frac{\int \boldsymbol{\alpha} \times \boldsymbol{r}}{\boldsymbol{\sigma}} \tag{2.60}$$

and

$$y = -2M \frac{\int i\gamma_5 \boldsymbol{r}}{\int \boldsymbol{\sigma}}. \tag{2.61}$$

The ratio (y) of the time component of the axial vector current to the Gamow-Teller matrix element can be extracted purely from the sum of $\alpha_{\mp}$,

$$(\alpha_- + \alpha_+) = -\frac{4}{3}(y/2M). \tag{2.62}$$

The difference of $\alpha_{\mp}$ comprises the weak magnetism term (a) and the second-class current term,

$$(\alpha_- - \alpha_+) = \frac{4}{3}\left(a - \frac{f_{\rm T}}{f_{\rm A}}\right). \tag{2.63}$$

2.4.2 Description including the mesonic effect

In order to discuss the meson-exchange contribution to the alignment-correlation term, the general form of the beta-ray angular correlation shape factors ($B_i(E)$) is defined as a function of the beta-ray energy,

$$W(E,P,A,\theta) \propto pE(E_0-E)^2[B_0(E) + P\cdot B_1(E)\mathtt{P}_1(\cos\theta) + A\cdot B_2(E)\mathtt{P}_2(\cos\theta)]. \tag{2.64}$$

To use the spectral shape ($w(E)$), which depends on only the beta-ray energy, Eq. (2.64) is translated as

$$W(E,P,A,\theta) \equiv w(E)\left[1 + P\frac{B_1(E)}{B_0(E)}\mathtt{P}_1(\cos\theta) + A\frac{B_2(E)}{B_0(E)}\mathtt{P}_2(\cos\theta)\right], \tag{2.65}$$

with

$$w(E) \propto pE(E_0-E)^2\cdot B_0. \tag{2.66}$$

In the present experiment we observed the beta-ray energy spectra in the direction $\theta = 0$ or π. The observed spectrum is thus described as

$$W_{\rm o}(E,P,A) = w(E)\left[1 + P\frac{B_1(E)}{B_0(E)} + A\frac{B_2(E)}{B_0(E)}\right] \tag{2.67}$$

and

$$W_{\pi}(E,P,A) = w(E)\left[1 - P\frac{B_1(E)}{B_0(E)} + A\frac{B_2(E)}{B_0(E)}\right]. \tag{2.68}$$

Here, $\frac{B_2(E)}{B_0(E)}$ is the alignment correlation term.

Chapter 3

Experimental Method

For determining the alignment correlation terms we must observe a pair of beta-ray-energy spectra with different spin alignments. These spectra must then be compared under the same conditions. It is therefore important to accurately measure the degree of polarization and alignment as well as the energy spectra. In the present study the experimental techniques were greatly improved very much compared with the previous ones. The procedure of the experiment comprised the production of polarized nuclei, the maintaining of the polarization, the manipulation of spin-ensemble and the observation beta-ray spectra. This chapter explains the experimental method used for the present work.

3.1 Production of Polarized Nuclei

A schematic view of the present experimental set up is given in Fig.(3.1). The ^{12}B and ^{12}N nuclei were produced through ^{11}B(d,p)^{12}B and ^{10}B(^{3}He,n)^{12}N reactions, respectively. Details concerning the experimental conditions for the production are listed in Table (3.1).

In the present experiments the pulse-beam method was used for low-background beta-ray detection. The target was enriched ^{10}B or ^{11}B ($100\mu g/cm^2$ thick) evaporated on the surface of a Mo-ribbon-target backing. The target backing was set in the groove of a fan-shaped target rotor. The size of the target backing was $430mm \times 3mm$, and $0.015mm$ thick. The diameter of the rotor was $760mm$. The rotation period was $60ms/rotation$. The production and beta-ray counting times were separated by chopping the incident beam. During the counting time the Mo backing was moved to the other end of the chamber and hidden by a radiation shield made of lead and iron for beta-ray detection with a very low background.

In the case of ^{12}B production, the procedure was as follows. A deuteron beam was accelerated to 1.5 MeV by the 4.8 MV Van de Graaff accelerator at Osaka University. The beam was chopped by an electrostatic deflector that was synchronized with the rotating target. The beam was then focused on the target with an area less than $2 \times 6mm$, thus inducing a nuclear reaction. The produced ^{12}B nuclei ejected from the target with the various recoil energies were caught in a catcher, given in Fig.(3.2). The recoil nuclei were polarized through the nuclear reaction. In order to obtain the optimum degree of polarization, the incident beam energy and the recoil angle were chosen as shown in Fig.(3.2).

The recoil nuclei were implanted into a single-crystal Mg catcher of about 200 μm thick in order to stop them within a definite area and to maintain their polarization. The Mg catcher was set so that the recoil nuclei ejected into any recoil angle from 40° to 75° would be implanted. At this solid angle the largest polarization and smallest alignment were obtained at the present incident energy. In order to maintain the polarization and to manipulate the nuclear spin ensemble by the nuclear magnetic resonance (NMR) technique, an external static magnetic field of about 300 Oe was applied along the flight path of the

recoil nuclei and the catcher area. Although the magnetic field was not sufficiently strong to completely maintain the polarization, the rate of depolarization was small, *i.e.*, a net polarization of about 13% was maintained; this was 85% of the initial polarization produced through the reaction. The experimental conditions for the ^{12}N are summarized in Table 3.1.

For an easy energy calibration of the beta rays, also these beta rays from ^{20}F, ^{41}Sc, and ^{17}F were also detected, for which BaF_2 and CaO targets were used. They were separately placed by evaporating at the end part of Mo backing. Each length of the target area was 20 mm. By adjusting the beam chopping time each target could be bombarded separately.

Table 3.1: Parameters for the production of the polarized nuclei.

	^{12}B		^{12}N	
Half Life $t_{1/2}$	20.41(6)	msec	10.97(4)	msec
Reaction	^{11}B(d,p)^{12}B		^{10}B(^{3}He,n)^{12}N	
Q value	1.1444(13)	MeV	1.5631(90)	MeV
Beam Energy	1.5	MeV	3.0	MeV
Recoil Angle	$40° \sim 75°$		$20° \sim 55°$	
Mean Recoil Energy	0.44	MeV	1.5	MeV
Stopper	Mg		Mg	
Max. Range	1.5	μm	2.7	μm
Magnetic Field	300	Oe	600	Oe
Max. Polarization	13	%	25	%

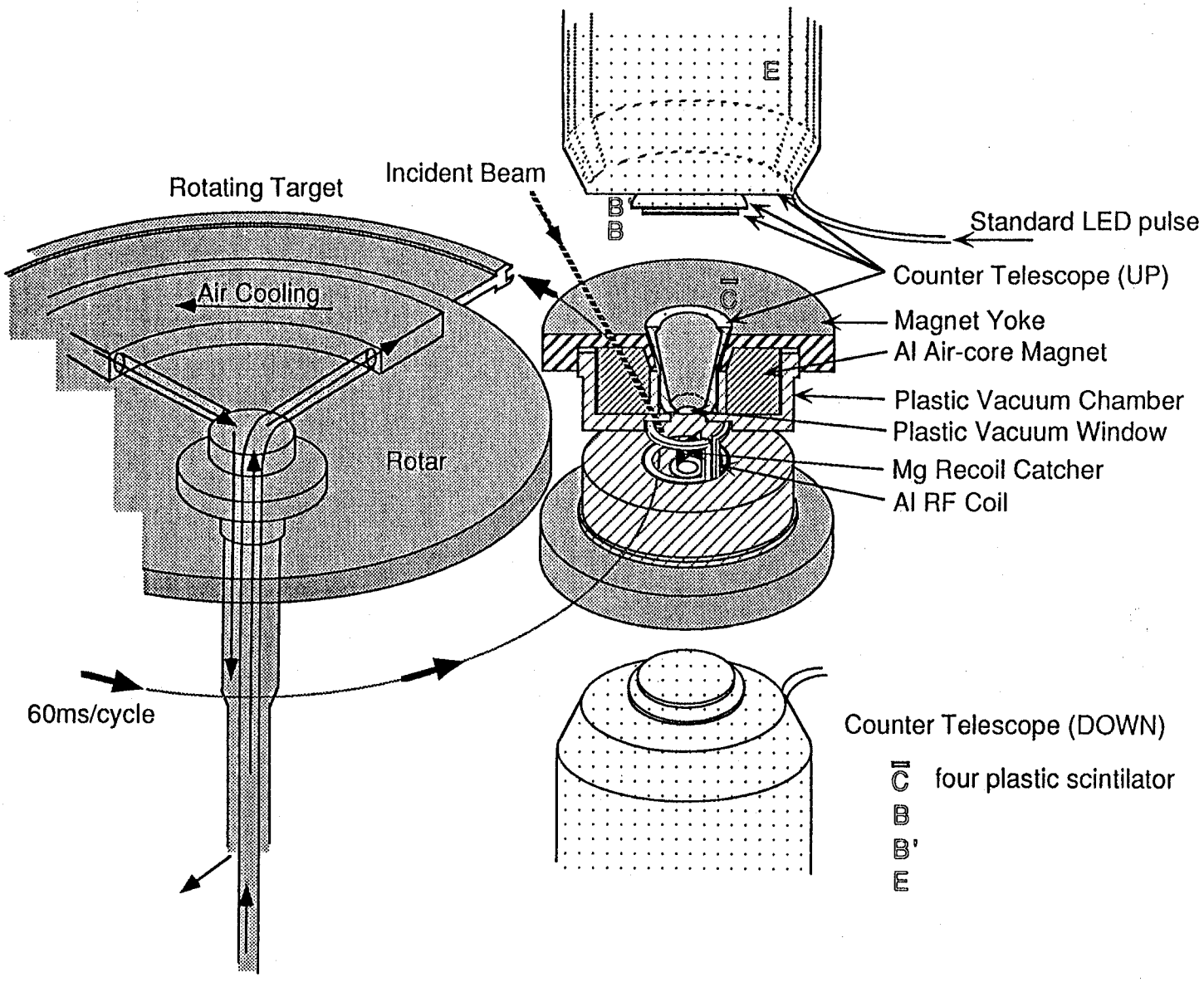

Figure 3.1: Schematic view of the present experimental setup. The target was rotated in a vacuum chamber. The target rotator was cooled by a jet of air running inside the rotator. The chamber was made of plastic in order to avoid any possible backscattering of beta rays from the wall. The beta rays from ^{12}B and ^{12}N in the recoil stopper were observed by two sets of counter telescopes. The energy counters (E) were equipped with a gain stabilizer using pulsed monitor light from an LED.

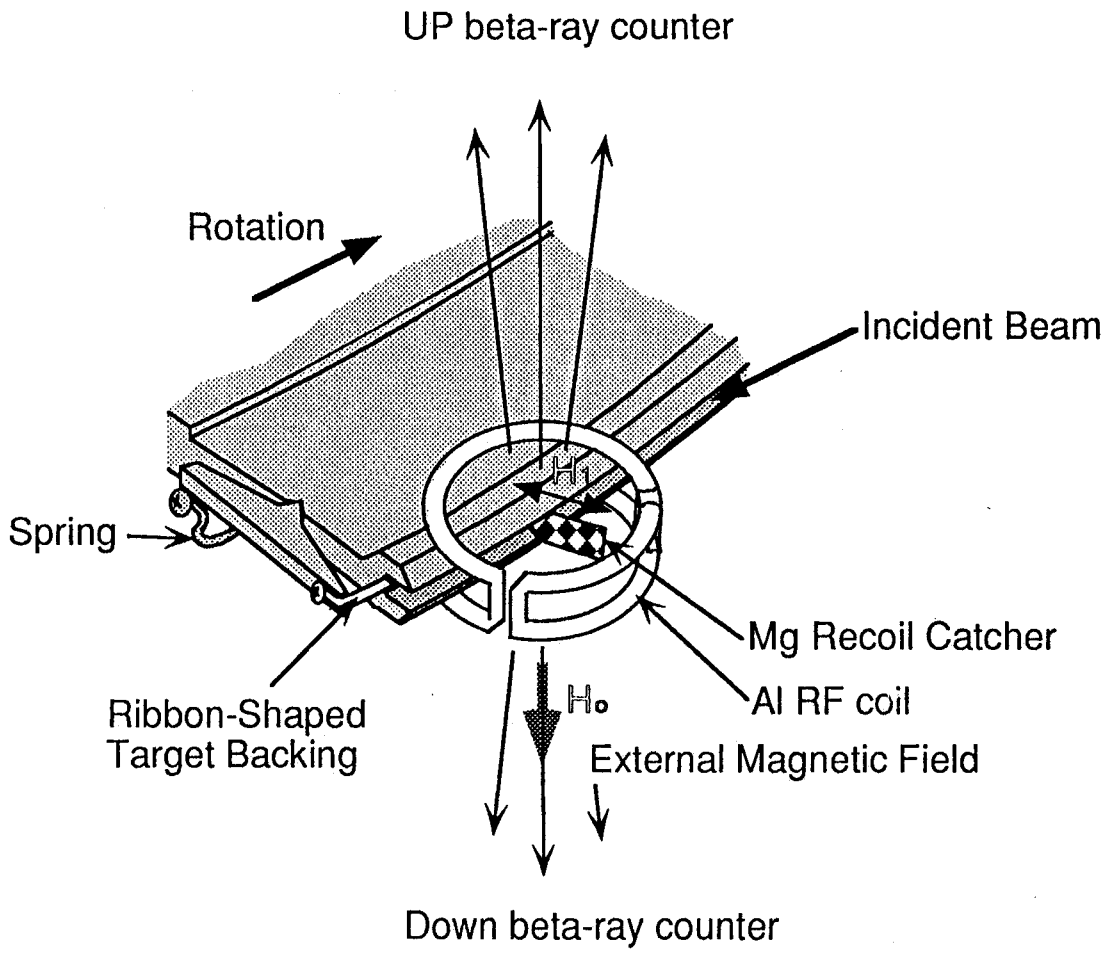

Figure 3.2: Production of polarized nuclei.

3.2 Manipulation of the Nuclear Spin Ensemble

The large polarization was obtained through the nuclear reactions. However, the pure alignment of both positive and negative signs, *i.e.* the large alignment without polarization, were necessary. We obtained this condition by using the spin manipulation based on the NMR technique. The control technique for the spin ensemble is thus crucial for obtaining aligned nuclei with no polarization. In this section we describe details concerning this technique.

3.2.1 Principle of the conversion from polarization to alignment

The energies of magnetic substates for a nucleus with spin $I = 1$ can be described as follows using first-order perturbation theory for strong field limit [30]:

$$E_m = -m\hbar\omega_L + \frac{1}{12}\hbar\omega_Q(3m^2 - I(I+1))(3\cos^2\theta - 1), \tag{3.1}$$

where

$$\omega_L = \gamma H_0,$$

$$(\gamma = \mu/I\hbar),$$

and

$$\omega_Q = \frac{3}{2}eqQ/\hbar. \tag{3.2}$$

Here, μ and Q are the nuclear magnetic moment and electric quadrupole moment; H_0 is the external magnetic field and q is the electric field gradient; θ is the angle between the external magnetic field and the principal axis of the field gradient. Under the present condition, ($I = 1$ and the angle $\theta = 0$),

$$E_m = -m\hbar\omega_L + \frac{1}{6}\hbar\omega_Q(3m^2 - 2). \tag{3.3}$$

The signs of eqQ, and thus the signs of ω_Q, had been previously determined so as to be negative for both ^{12}B and ^{12}N implanted in the Mg single crystal [31]. Since the sign of the initial alignment was known to be positive for both ^{12}B and ^{12}N, the magnetic substate populations of ^{12}B and ^{12}N were as schematically shown in Fig.(3.3). H_0 was set so as to be parallel to the initial polarization, as shown in Figs.(3.2) and (3.3).

The separations of the energies between adjacent substates were as follows:

$$\begin{aligned} \Delta E_{-1\leftrightarrow 0} &= \hbar\omega_L + \frac{1}{2}\hbar\omega_Q \\ \nu_\ell &= \frac{1}{2\pi}(\omega_L + \frac{1}{2}\omega_Q), \end{aligned} \tag{3.4}$$

and

$$\begin{aligned} \Delta E_{+1\leftrightarrow 0} &= \hbar\omega_L - \frac{1}{2}\hbar\omega_Q \\ \nu_h &= \frac{1}{2\pi}(\omega_L - \frac{1}{2}\omega_Q), \\ \nu_\ell &< \nu_h \qquad\qquad (\omega_Q < 0). \end{aligned} \tag{3.5}$$

We could thus induce a transition between substates $m = 1$ and $m = 0$, or between $m = 0$ and $m = -1$, separately, by applying an RF field (H_1) at frequencies of ν_ℓ or ν_h, respectively.

We could also induce a double quantum transition between substate $m = 1$ and $m = -1$. The transition energy and the frequency were

$$\Delta E_{+1\leftrightarrow -1} = 2\hbar\omega_L \tag{3.6}$$

and

$$\nu_{\mathrm{L}} = \frac{1}{2}(\nu_{\ell} + \nu_{h}). \tag{3.7}$$

A double quantum transition could thus be induced at the center frequency (ν_{L}) while neglecting the second-order shift. This separated frequencies (ν_{ℓ}, ν_{h}, and ν_{L}) offer a way to control the spin ensemble.

We used two kinds of methods in the NMR technique to handle substate populations: one was the adiabatic fast-passage (AFP) method for exchanging substate populations between two levels; the other was the depolarization (DEP) method for equalizing two substate populations.

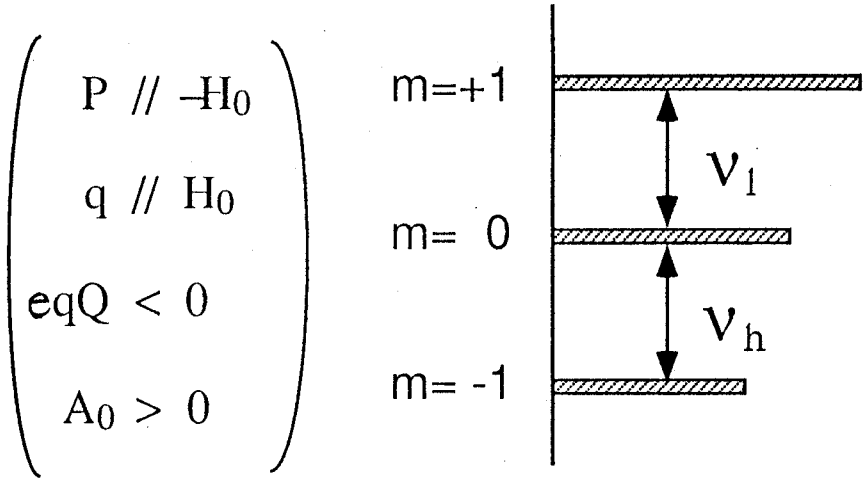

Figure 3.3: Schematic view of the magnetic substate populations (a_m); a_m depends on the nuclear reaction and magnetic field. In the present experiment, the direction of the polarization was antipararell to H_0 and the initial alignment was positive [31].

AFP method

When the frequency of the RF field is swept across the resonance frequency, $\omega = (E_m - E_{m'})/\hbar$, with an adequately slow sweep velocity and a strong RF field, the magnetic substates populations, a_m and $a_{m'}$, are interchanged. This process is called adiabatic fast passage (AFP) [32].

Upon determining from the coordinate system which is rotating with the same frequency (ω) as the applied RF magnetic field, the effective magnetic field (H_{eff}) becomes a fixed vector and the spin (I) precesses around H_{eff}, as shown in Fig.(3.4). When the RF frequency is swept across the resonance frequency (ω_L) in such a way that the effective field (H_{eff}) is inverted, as shown in Fig.(3.4), the nuclear spins also became inverted while following the motion of the effective field. It is necessary that the angular velocity of the rotation of H_{eff} is much slower than that of the precession of the spin around H_{eff} for a complete inversion of the spin. The adiabatic condition is thus given as

$$\frac{1}{\gamma H_1}\frac{d\omega}{dt} \ll \gamma H_1. \tag{3.8}$$

The frequency of the RF field (H_1) must therefore be modulated according to the above condition. Furthermore, in order to achieve a perfect population interchange, the amplitude of the RF magnetic field must also be modulated sinusoidally as a function of time, as shown in Fig.(3.5). Then the RF is swept around the off-resonance frequency the direction of the nuclear spin is restored during the final stage of the sweep (Fig.(3.6)), while causing no effect at the off-resonance frequencies. We designed the RF amplifier system while considering this AFP condition (Eq. (3.8)). The actual condition was determined experimentally from a test in which the achievement of conversion was tested as a function of the RF amplitude.

The conditions used in the present study are given in Table (3.2).

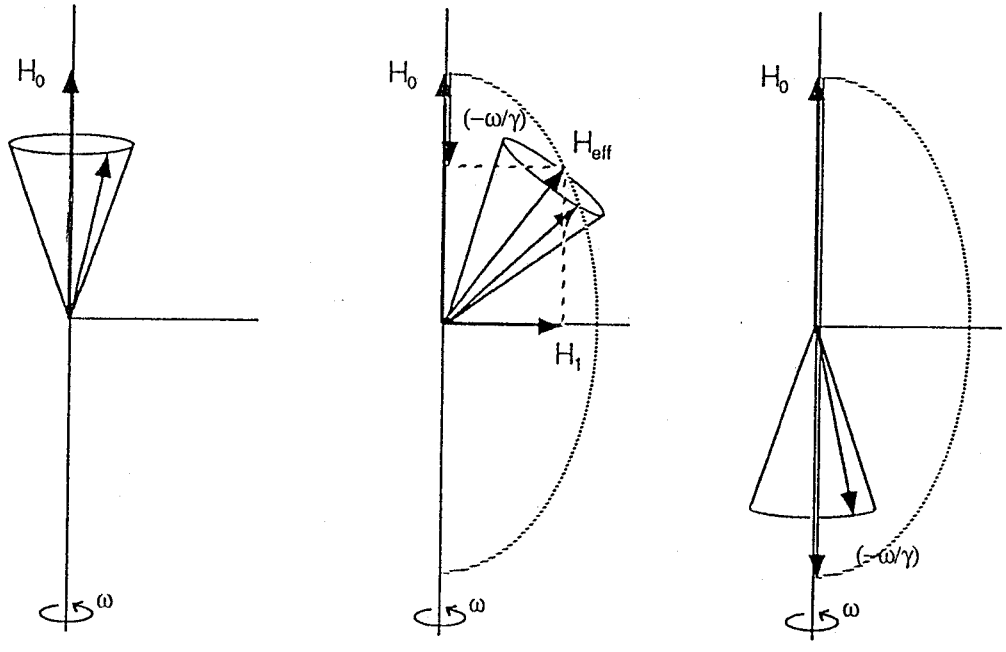

Figure 3.4: Effective magnetic field applied by the frequency-modulated RF and the principle of adiabatic fast passege (AFP). The RF frequency is swept across the resonance frequency (ω_L) in such a way that the effective field (H_{eff}) is inverted; nuclear spins are also inverted following the motion of the effective field.

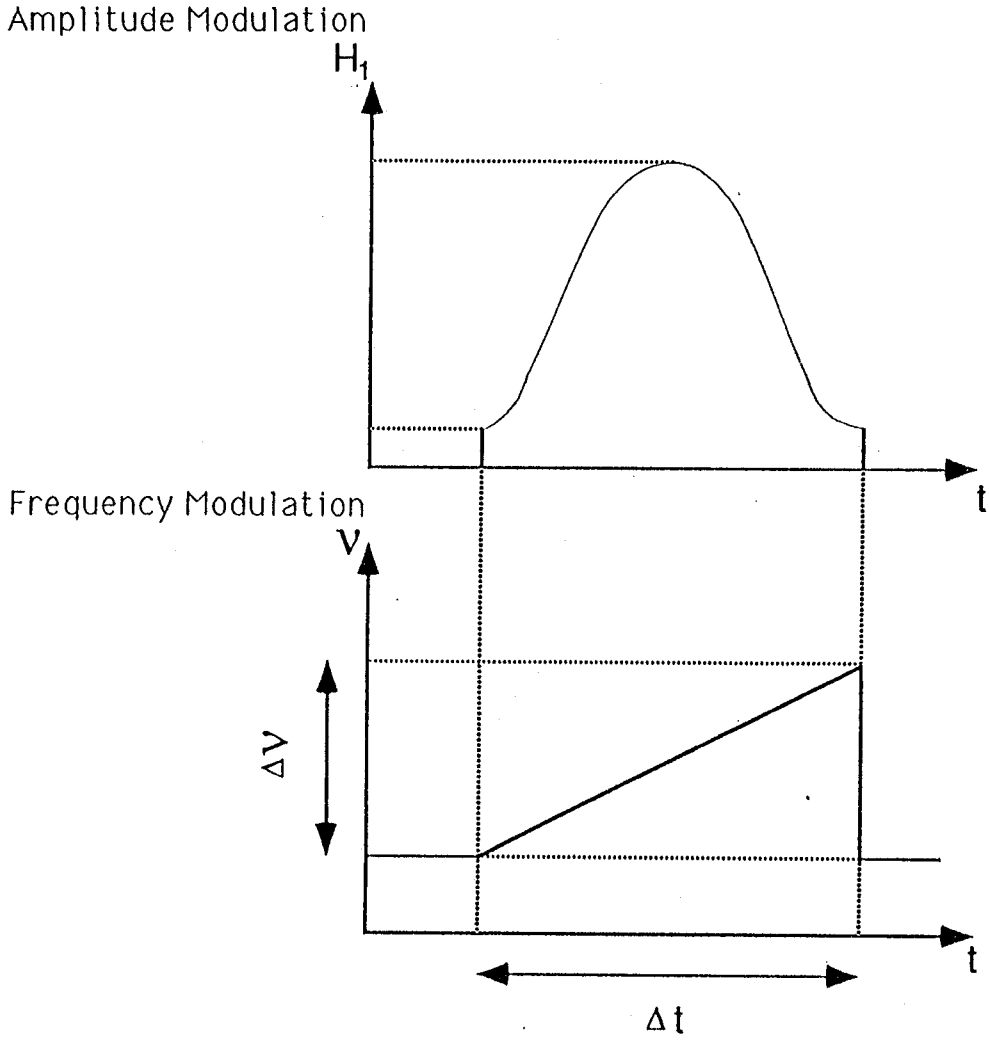

Figure 3.5: Schematic view of the amplitude and frequency modulation of the RF magnetic field as a function of time. The amplitude reaches its maximum at the resonance frequency.

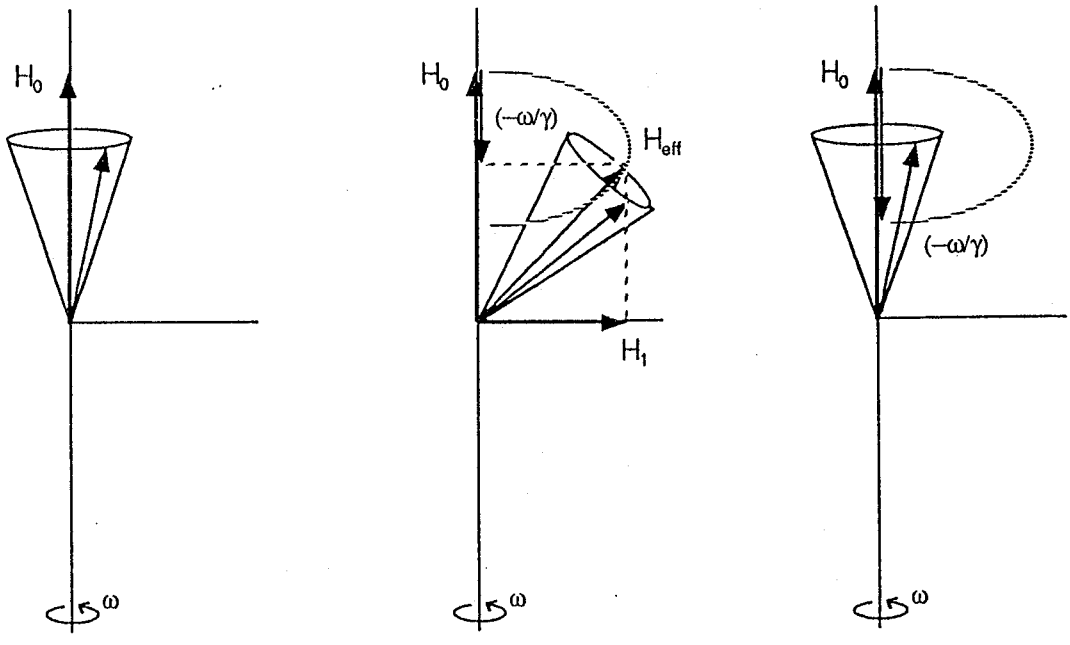

Figure 3.6: Magnetic field under the off AFP condition. When the RF is swept around the off-resonance frequency, the direction of the nuclear spin is restored during the final stage of the sweep. As a result, there is no effect at the off-resonance frequencies.

Depolarization method

The principle of the depolarization (DEP) method is described as follows. When an RF is applied at the on-resonance frequency, the nuclear spin precesses around H_1 with a frequency of γH_1 in the rotating frame. The precession frequencies spread due to the nuclear dipolar broadening (H_D) and the inhomogeneity of the external field, and even the inhomogeneity of the RF magnetic field. Therefore, after a sufficient time duration, the polarization is destroyed. In actual experiments, the RF frequency was modulated in frequency in order to cover the resonance time width. The actual condition is given in Table (3.2).

Conversion of polarization into alignment

A schematic diagram designed to explain the principle used to convert the polarization to a sizable degree of alignment is shown in Fig.(3.7). To convert the nuclear polarization to positive alignment, a depolarizing RF field was first applied at ν_h, the substate populations of $m = 0$ and $m = -1$ were thus equalized ($a_0 = a_1$), and a resultant polarization of $P_{\rm I}$ was obtained (Fig.(3.7)). An RF field for AFP was then applied at ν_ℓ, so that the substate populations of $m = 1$ and 0 were interchanged ($a_0 \leftrightarrow a_1$); the resultant polarization ($P_{\rm II}$) became equal to zero. We could thus obtain a pure positive alignment of $A_+ = 3/2P_0 - 1/2A_0$ if the depolarization and AFP were perfectly obtained and the relaxation effect of polarization and alignment was negligible. An RF magnetic field for AFP (AFP field) at ν_ℓ was finally applied once again in order to shift the alignment back to polarization and polarization $P_{\rm III}$ was thus obtained. In actual experiments $P_{\rm III}$ was smaller than $P_{\rm I}$ ($P_{\rm III} <$

P_{I}) due to the spin relaxation effect of alignment. We thus obtained a relaxation time of T_1 for the alignment from P_{I} and P_{III}. To obtain a negative alignment, a depolarization field was first applied at ν_ℓ; AFP was then applied at ν_h.

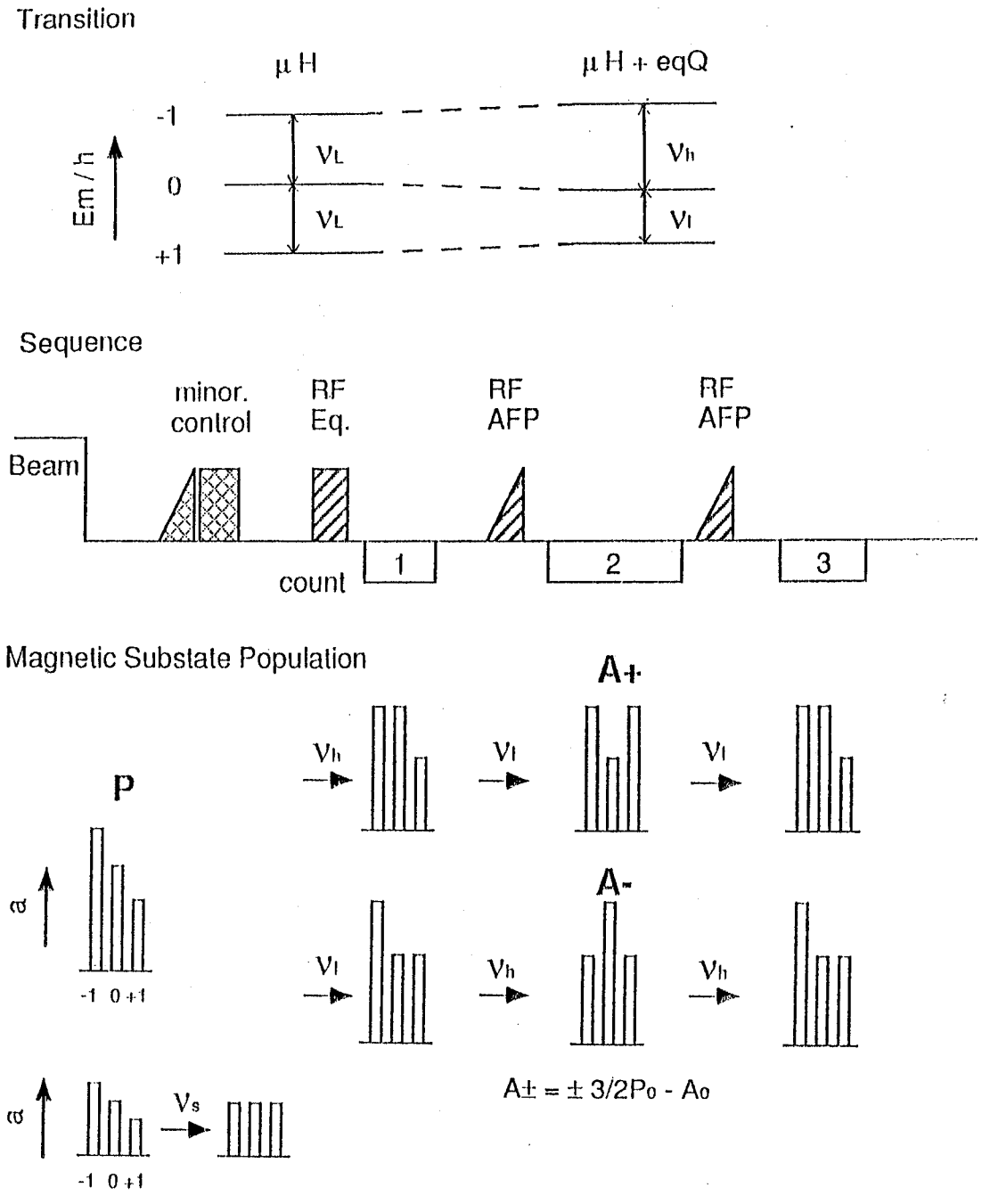

Figure 3.7: Schematic diagram of the spin control for producing the conditions $P = 0$ and $A = +A$ or $A = -A$. The closed triangle-shape RF indicates that the RF satisfied the AFP condition; the closed square-shape RF indicates the RF for equalization of two magnetic substates. The transition between $m = +1$ and $m = 0$ as well as the transition between $m = -1$ and $m = 0$ can be separated by selecting the resonance frequency ν_h and ν_l

3.2.2 Hyperfine interactions of ^{12}B and ^{12}N in a Mg single crystal

In order to accurately measure the alignment coefficients, knowledge concerning the hyperfine interactions of ^{12}B and ^{12}N in the Mg catcher is necessary. For this purpose, we studied the NMR spectra of ^{12}B and ^{12}N implanted in the Mg single crystal in detail [26].

The NMR spectra for both the single and double quantum transitions were observed with good accuracy as a function of the orientation angle of the c-axis relative to the external magnetic field (H_0), the amplitude of H_0, the amplitude of the RF magnetic field (H_1), and temperature of the Mg catcher. Fig.(3.8) shows a typical NMR spectrum of single quantum transitions between $m = \pm 1$ and 0 for $I = 1$ of ^{12}B in Mg with the crystal c-axis parallel to the external magnetic field. The line widths were determined under the condition of the weak H_1 and the low-temperature limit. We clearly observed a pair of small peaks located within a pair of large peaks for the majority of ^{12}B . A small fraction of ^{12}B thus sits at another site where the electric field gradient (q) is different from the ^{12}B at the major site.

The electric field gradient at the minor site could be determined by measurements of the quadrupole splitting or second-order shift of the double quantum transition. The direction of the field gradient was about 90° for the c-axis with the asymmetry parameter being close to zero. The magnitude of the coupling constant was the same as that for the major site.

It was shown that the q-axis of the minor component was perpendicular to the crystal c-axis. However, the q-axis was not directed in any specific direction, but was distributed

in the crystallographic a_1-a_2 plane. In the case of ^{12}N, the observed spectra also had the same structure, as shown in Fig.(3.10).

The q for the majority was parallel to the crystal c-axis with an asymmetry parameter of $\eta = 0$. According to observations of the line split of a pair of single quantum transitions as a function of crystal orientation, the quadrupole coupling constants, $|eqQ(^{12}\mathrm{B})/h| = (47.0 \pm 0.1)$ kHz and $|eqQ(^{12}\mathrm{N})/h| = (59.3 \pm 1.7)$ kHz, were determined for the majorities of ^{12}B and ^{12}N, respectively.

Figs. (3.9) and (3.11) show the double quantum transitions between $m = +1$ and $m = -1$. The double quantum transitions are free from a small effect due to a spread in the strength of the quadrupole interaction caused by lattice defects. The line width therefore represents the nuclear dipolar broadening directly. The line width was deduced using spectra with a Lorentzian distribution. The width was, thus, measured as a function of the crystal orientation and was compared with the van Vleck's values of the dipolar broadening. By using Gaussian distributions, no appreciable changes were recognized within the statistical error. Thus, in the case of ^{12}N in Mg, the final site was determined to be the interstitial trigonal site (the center of a trigonal prism structure in a h.c.p. lattice; see Fig.(3.12)). For the present analysis, a rearrangement of the lattice due to interstitial impurities was taken into account as a lattice expansion. It was concluded from the present results that, at least, the nearest neighbors of the impurities were expanded by about $\Delta a/a = (15 \pm 5)\%$. Also, in the case of ^{12}B, the final site was the interstitial site. However, no specific final site was definitely determined.

When some locations exist, as in the present case, each NMR time for each group of ^{12}B at different sites is necessary in order to control all nuclear spins of the nuclei. In

the case of ^{12}B and ^{12}N in Mg, the same control scheme used for the majority couldn't be applied to the minority, since they have field gradients with different directions. Their transitions couldn't be separated by the frequency for control.

The most important result in this study concerning the hyperfine interactions is that each transition of the majority could be separated from that of the minority. The crystal c-axis was therefore set parallel to the external magnetic field, since the spin-ensemble of the majority could be controlled without affecting the spin-ensemble of the minority. Namely, we can induce any transitions for any sites, independently.

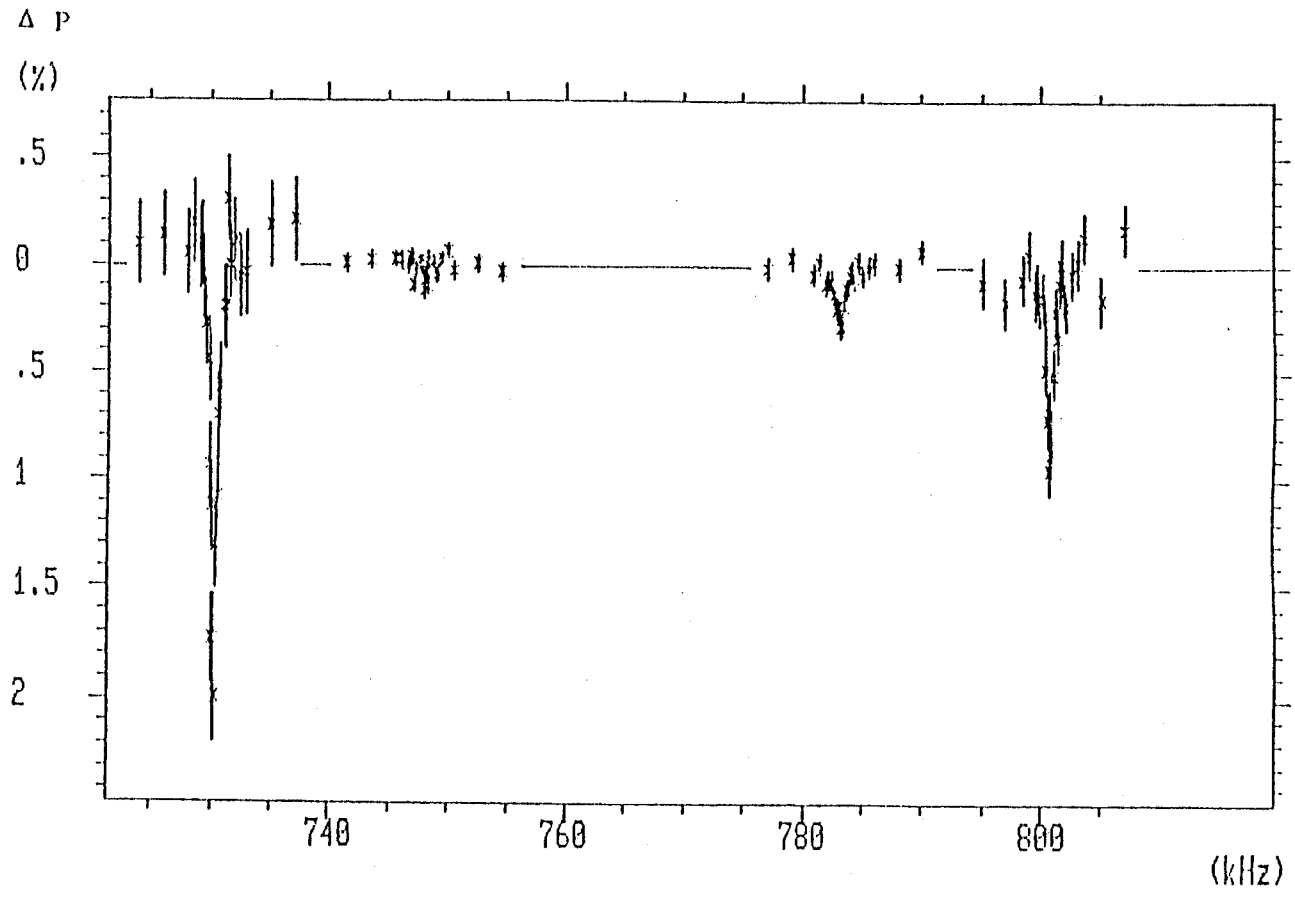

Figure 3.8: Typical NMR spectrum of the single quantum transitions (SQ) for ^{12}B. The external magnetic field is 1.0 kOe, and the applied RF magnetic field is about 2 Oe. The crystal c-axis is set pararell to the external magnetic field. The horizontal axis is the resonance frequency (kHz). The central sharp line shows the resonance of the double quantum transition. The vertical axis is the polarization change due to depolarization as the result of equalizing the RF (%). At the off-resonance point the amount of initial polarization does not change.

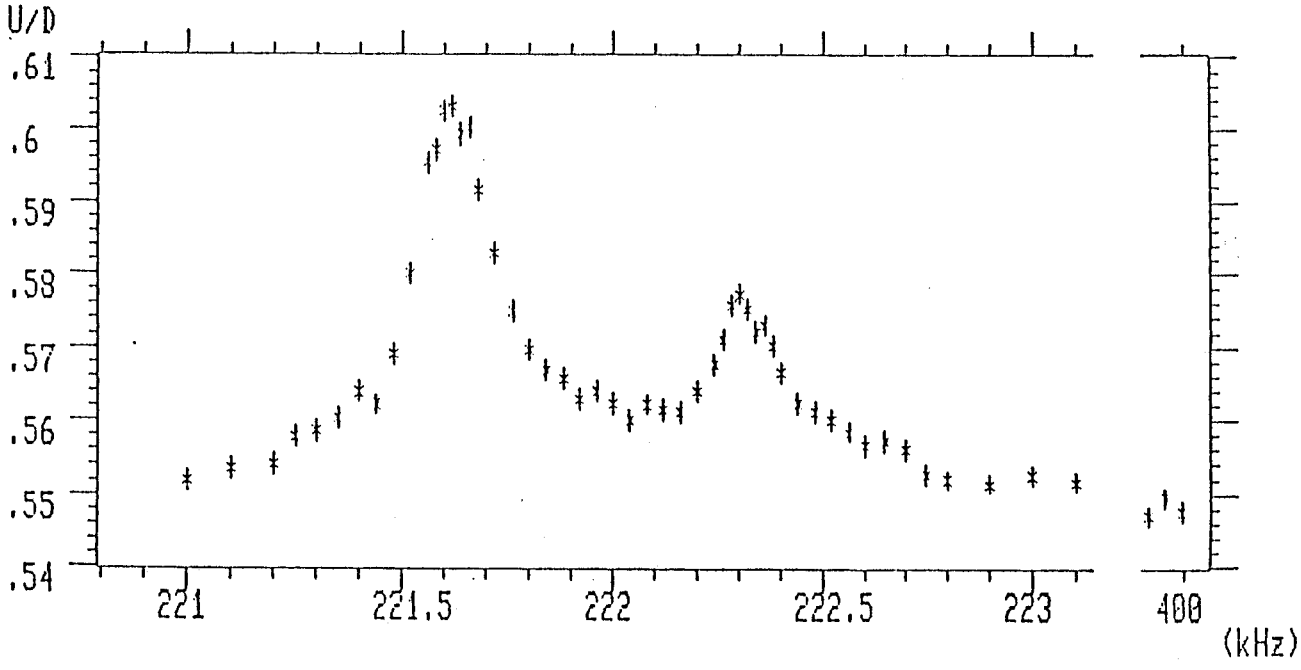

Figure 3.9: Typical NMR spectrum of the double quantum transition (DQ) for ^{12}B. The external magnetic field is 290 Oe, and the applied RF magnetic field is about 1.9 Oe. The crystal c-axis is set to pararell to the external magnetic field.

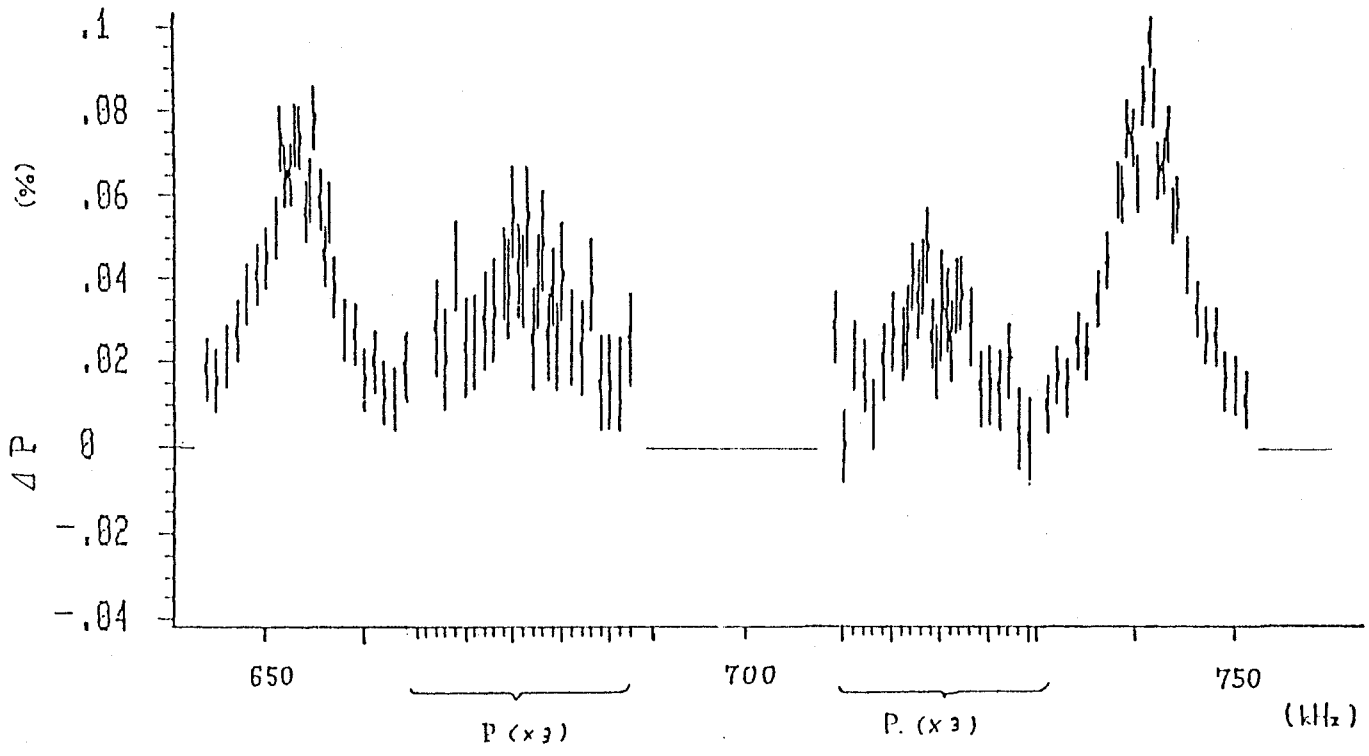

Figure 3.10: Typical NMR spectrum of the single quantum transitions (SQ) for ^{12}N. The external magnetic field is 2.0 kOe, and the applied RF magnetic field is about 2 Oe. The crystal c-axis is set pararell to the external magnetic field. The horizontal axis is the resonance frequency (kHz). The central sharp line shows the resonance of the double quantum transition. The vertical axis is the polarization change due to depolarization as the result of equalizing the RF (%). At the off-resonance point, the degree of initial polarization does not change.

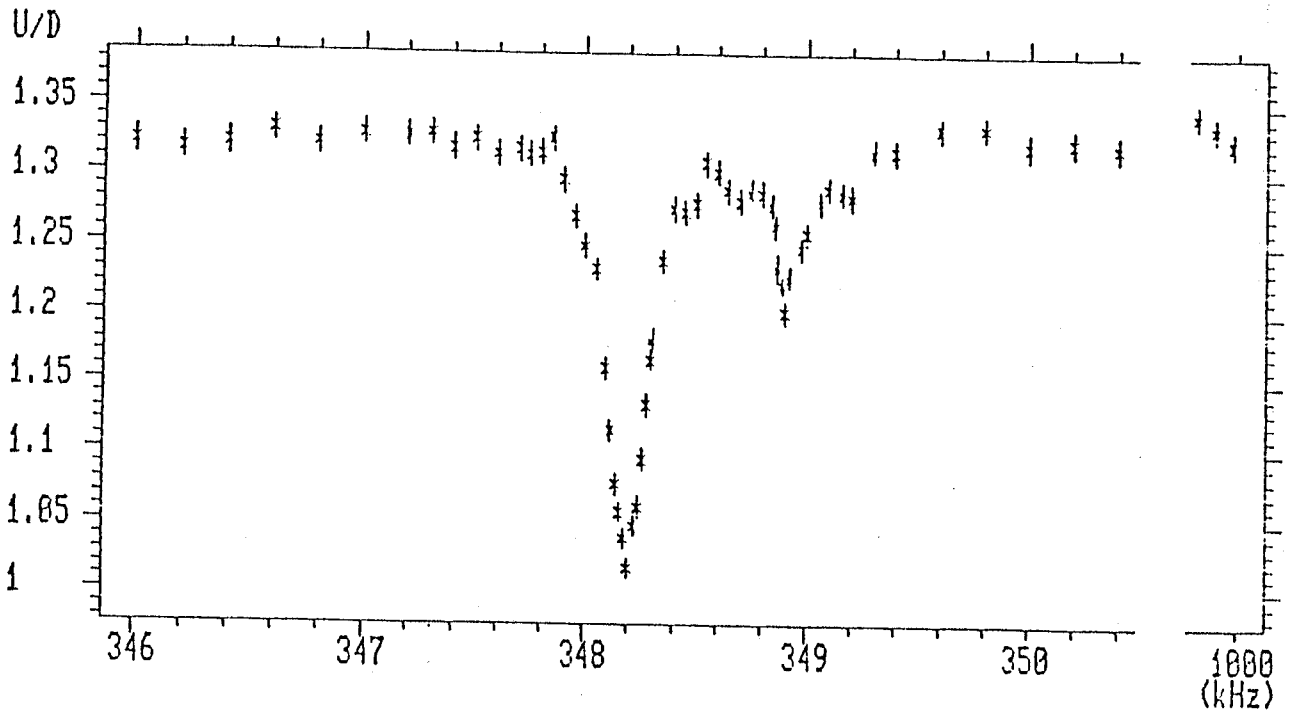

Figure 3.11: Typical NMR spectrum of the double quantum transition (DQ) for ^{12}N. The external magnetic field is 1.0 kOe and the applied RF magnetic field is about 4 Oe. The crystal c-axis is set pararell to the external magnetic field.

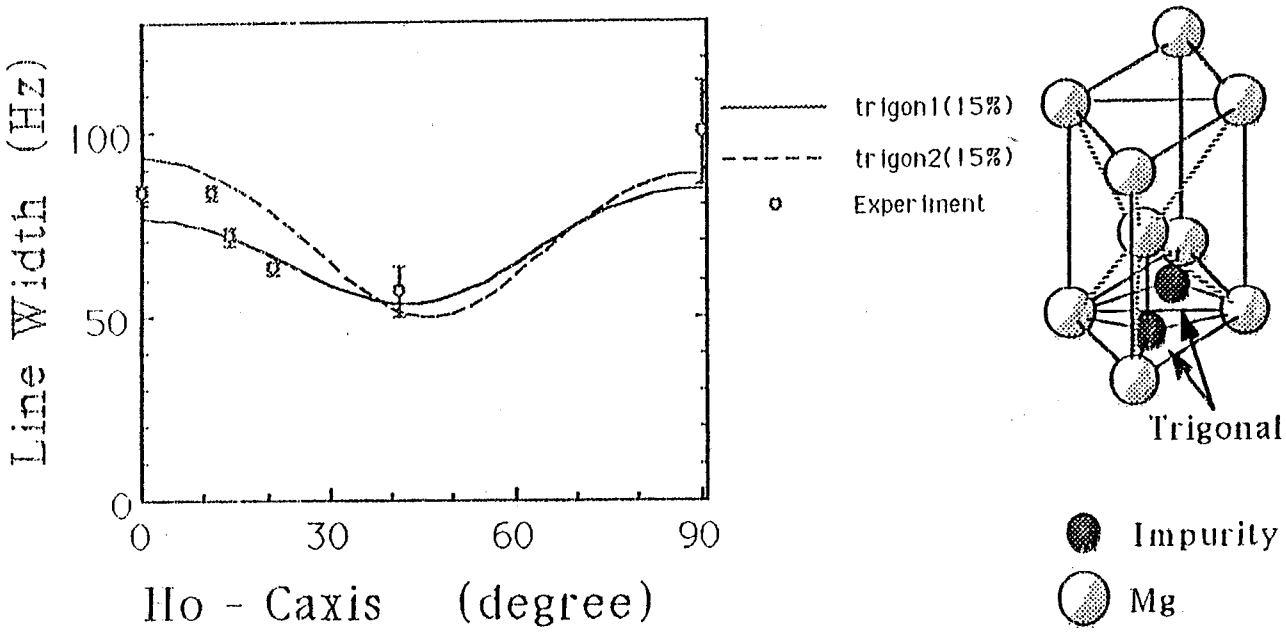

Figure 3.12: Final sites of impurities in the Mg single crystal (with h.c.p. structure). In the case of ^{12}N in Mg, the final site was determined to be the interstitial trigonal site (the center of a trigonal prism structure in a h.c.p. lattice) by the measurement of dipolar broadeninng line width. The left figure shows the observed line width of ^{12}N in Mg as a function of the crystal orientation. The solid lines indicate the theoretical value from the van Vleck formula for interstitial nuclei located at trigonal interstitial sites with a 15% lattice expansion.

3.2.3 Time sequence of the present experiment

Since we found that the sites with minor implanted nuclei for both ^{12}B and ^{12}N have different quadrupole couplings from that of the majority, the spin-ensemble control for both groups is necessary for a complete conversion of polarization to alignment.

Before carrying out spin control for the majority, spin control for the minority was undertaken. Since the direction of the q-axis for the minority is not unique, it was not easy to convert the polarization of the minority into alignment, and to use it for measurements. We therefore equalized the substate populations of the minority in actual measurements. Since it takes a relatively long time to completely equalize the substate populations using the DEP method, due to the spread of the field gradient, we equalized the populations as much as possible within a very short time.

The time sequence used to realize spin control for the present experiment is shown in Fig.(3.13). The procedure used to producing a positive alignment is shown as the $[A_+]$ part in Fig.(3.13). To equalize the populations for the minority, RF_{11} and RF_{12} were applied. RF_{11} is an RF with a single-sweep frequency modulation (FM) for the AFP technique (see section 3.2.1). RF_{11} covered the resonance frequency (ν_h') of the transition between $m = +1$ and $m = 0$ of the minority in order to exchange the magnetic substate population, a_{s1} and a_{s0} ($m = +1$ and 0). The width of the frequency modulation was 25 kHz, the sweep time of the frequency was 1ms, and the RF amplitude was about $H_1 \sim 5$ Oe, which satisfied the AFP condition described in Eq. (3.8). RF_{12} was an RF with a repetitive frequency modulation around the transition frequency (ν_l) for equalizing the sublevel populations (a_{s0} and a_{s-1}) of the minority. The width of the frequency modulation was 20 kHz; the

frequency was swept seven times; one sweep time was 0.3 ms. The amplitude of the RF was about 1 Oe. Although this sweep speed (20 kHz/0.3 msec) and amplitude was just sufficient for the DEP method, they were not sufficient for AFP. As a result of the spin control by RF_{11} and RF_{12}, the populations (a_{s1}, a_{s0}, and a_{s-1}) were nearly equal. After this procedure, the minority was left as it controlled, or was not disturbed by any other RF applied later.

Secondly, the spin-ensemble of the majority was controlled in order to convert polarization to alignment. The amplitude, frequency modulation width, and duration of the frequency sweep were the same as in the case of nuclei in the minority. The details are listed in Table 3.2. RF_{13} equalized the population (a_{m0} and a_{m-1}) of the majority. The beta-ray asymmetry was measured in count section I in order to determine the polarization (P_I). RF_{14}, RF with a single-sweep FM for the AFP, exchanged populations a_{m0} and a_{m+1}. Thus, the polarization was converted to alignment A_+. The beta ray spectra from the aligned nuclei were observed either at $\theta = 0°$ or 180° and from the polarization in count section II. The up-down asymmetries derived from these spectra also gave the degree of polarization (P_{II}); the degree of alignment was deduced. RF_{15} exchanged population a_{m0} and a_{m+1} again to convert the alignment back to polarization. Polarization P_{III}, measured in the count section III, was compared with polarization P_I in order to deduce the relaxation time for the alignment.

The procedure used for the spin manipulation to produce a negative alignment was essentially the same as that used for a positive alignment, as shown in the [A_-] part. It was important that part of the procedure used for the minority site was the same as that for positive alignment; the remaining procedure for the majority was reversed in the order of

the RF sequence for manipulating the substate populations. The same procedure resulted in the same residual populations in the $[A_+]$ and $[A_-]$ parts. Therefore, the effect due to the residual polarizations of the minority was canceled.

The $[P_+]$, $[P_-]$, and $[P_{++}]$ parts involved procedures for determining the polarization and geometrical asymmetry, and for checking the achievement factor. The $[P_+]$ part did not involve RF control, and gave the initial beta-ray asymmetry in count sections I, II, and III. In the $[P_-]$ part, RF_{41} was applied for the AFP at the double quantum transition between $m = +1$ and $m = -1$. The amplitude of the RF was $H_1 \sim 25$ Oe, the width of the frequency modulation was $\Delta\nu = 14$ kHz, and the duration of the frequency sweep was 2 ms. The AFP for the double quantum transition required a stronger RF field than that for the single quantum transitions. RF_{41} exchanged the total population a_{+1} and a_{-1} of nuclei both of the majority and minority, so that the initial polarization was reversed. The beta-ray asymmetry for the reversed polarizations were observed at count times I, II, III. In order to obtain the ratio of the initial beta-ray asymmetry to that for the reversed polarization, the geometrical efficiency in the beta-ray detectors was automatically cancelled. Since this ratio included the factor for the achievement of the AFP technique, a fifth cycle was introduced in order to determine the achievement factor. RF_{51} and RF_{52} were applied in order to invert the initial polarization, and to give it back again. The ratio of the initial asymmetry to that of the final was thus used to probe for the completeness of AFP achievement. The polarizations in all counting sections were determined from asymmetry measurements during the $[P_+]$, $[P_-]$, and $[P_{++}]$ cycles.

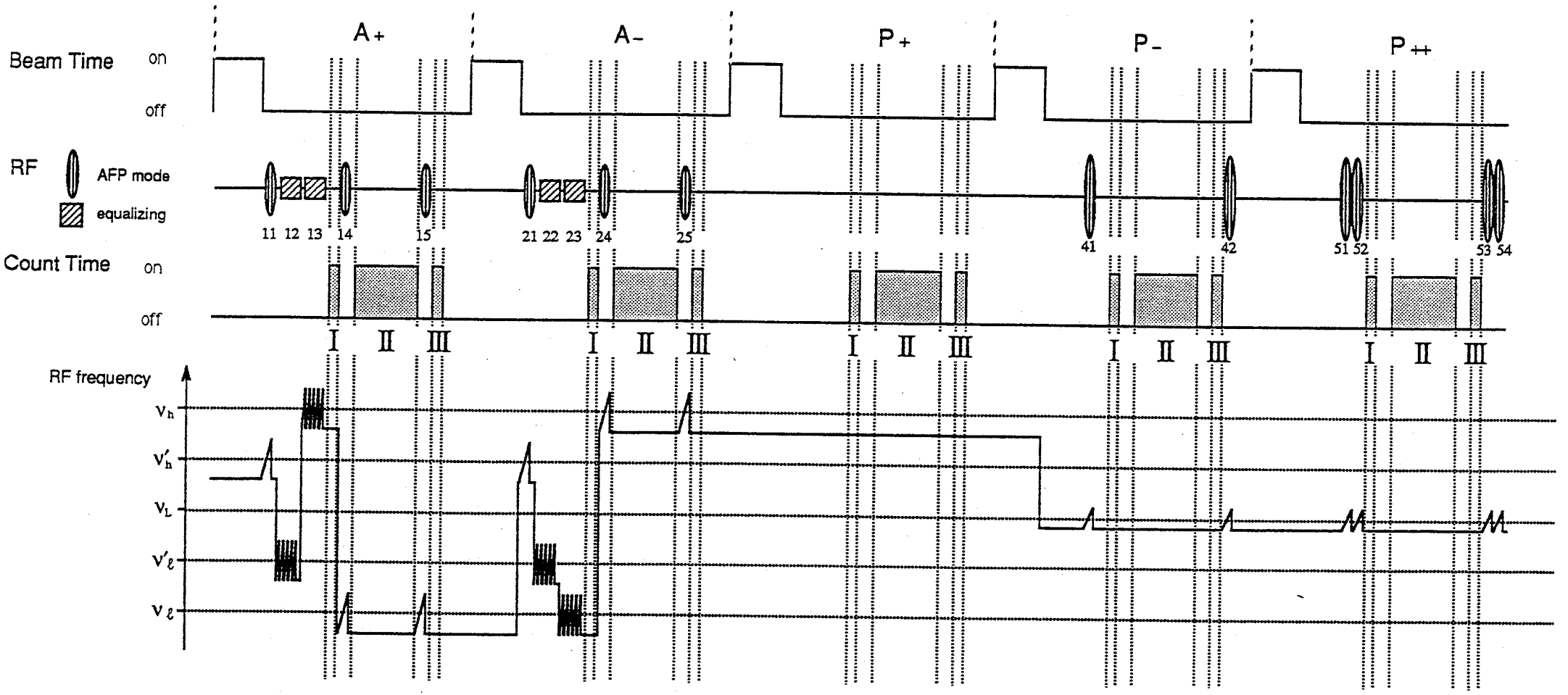

Figure 3.13: Schematic time sequence of the experiments controlled by the computer system. In order to decrease the statistic error of the beta-ray spectra with the alignment the $A = A_+$ and $A = A_-$, A_+ and A_- sections were repeated 10 times, the other sections were repeated 2 times in one complete control cycle.

3.2.4 RF system

The RF coil for producing an oscillating magnetic field (H_1) at the catcher comprised a pair of coils which were saddle shaped (Fig.(3.2)) in a way similar to the electron beam deflector used in a television set. This shape resulted in a better homogeneity of the RF field (H_1) over a wider effective area compared with a Helmholtz coil. The RF coil comprised $0.6mm$ thick Aℓ wire coated with a thin polyester film. Since the Mg catcher was heated by eddy currents induced by the RF field (H_1), it was mounted on a holder made of Aℓ to which a water-cooling system was attached inside the vacuum chamber. An RF coil with an aperture of $5cm$ in diameter, which faced the top and bottom beta-ray windows, was sufficiently large that the beta-ray counter telescopes did not detect the beta-rays scattered directly by the RF coil.

The RF amplification circuit is shown in Fig.(3.15). The circuit used in the present experiment comprised of two parts. One was a linear amplifier for the transmission of RF power; the other was a logic circuit used to gate the RF. The four RF sources were independently applied for each NMR technique, *i.e.*, the AFP and the equalization.

Three frequency synthesizers were used for the AFP technique. The AFP technique required a single sweep of the frequency modulation and sine-wave amplitude modulation. The single-sweep FM was obtained by using a ramp signal from a ramp generator. The AFP technique used for the single quantum transition required different sweep times of the frequency from that of the double quantum transition. Two ramp generators were therefore used for the AFP techniques. Amplitude modulation was provided by the sine-wave signal from another function generator. The double-balanced mixer works as an RF modulation

for sine-wave modulation. The RF amplitude for the AFP technique was controlled by attenuated square waves from the gate generators.

Three function generators were used to equalize the populations. The function generators produced frequency-modulated RF signals which were gated within the RF time. Equalization required a more accurate amplitude control than in AFP technique. The RF amplitude, the width of the frequency modulation, and the duration of the frequency sweep from each function generator were adjusted to the condition of each transition. All of the RF signals were mixed by an analogue mixer and, finally, power amplified by a 1000 W amplifier. In the present system the achievement factors of the spin control reached close to 100%, as listed in Table 3.3 and shown in Fig. (3.14).

			^{12}B	^{12}N
Spin	I^π		1^+	1^+
Half Life	$t_{1/2}$	(msec)	20.41(6)	10.97(4)
Magnetic Moment	μ	(μ_N)	1.003(1)	0.4571(5)
Electric Quadruple Moment	Q	(b)	0.0171(16)	$\sim$ (0.01)
$\angle(H_0 - c_{axis})$			0°	0°
Sign of eqQ in Mg			(−)	(−)
RF condition				
DQ AFP	H_1	(Oe)	10	25
	t_{RF}	(ms)	1	2
	Δf	(kHz)	14	14
SQ AFP	H_1	(Oe)	2	5
	t_{RF}	(ms)	1	1
	Δf	(kHz)	15	25
SQ DEP	H_1	(Oe)	1	1
	t_{RF}	(ms)	1	2
	Δf	(kHz)	15	20

Table 3.2: RF system conditions for the spin control; t_{RF} includes the amplitude modulation time.

			^{12}B	^{12}N
Achievement of AFP	$\alpha_{\rm DQ}$		0.9819 ± 0.0059	0.9776 ± 0.0045
			$(0.9476 \pm 0.0046)^*$	$(0.9776 \pm 0.0066)^*$
	$\eta_{\rm SQ}$	$\nu_\ell{}^{\rm main}$	0.9931 ± 0.0045	0.9889 ± 0.0059
			$(0.9654 \pm 0.0053)^*$	$(0.9630 \pm 0.0060)^*$
	$\eta_{\rm SQ}$	$\nu_h{}^{\rm main}$	0.9905 ± 0.0046	0.9799 ± 0.0057
			$(0.9708 \pm 0.0041)^*$	$(0.9816 \pm 0.0075)^*$
	$\eta_{\rm SQ}$	$\nu_h{}^{\rm sub}$	0.99243 ± 0.001	0.9827 ± 0.006
			$(-)^*$	$(-)^*$
Effective residual polarization	ΔP	(%)	0.070 ± 0.079	0.40 ± 0.21
Effective alignment change	ΔA	(%)	14.27 ± 0.20	34.26 ± 0.40
Relaxation time	$T_1(P)$	(ms)	179 ± 10	173 ± 21
	$T_1(A)$	(ms)	45.6 ± 1.8	61.0 ± 5.9

Table 3.3: Typical achievement of spin control.

(old data)* have the condition that $\angle(H_0 - c_{\rm axis}) = 90°$.

Here, $\alpha_{\rm DQ}$, η, ΔP and ΔA are defined as follows:

$$P \overset{\rm DQAFP}{\longrightarrow} \alpha_{\rm DQ} P \ ,$$

$$a_{\rm m} \overset{\rm SQ(m\leftrightarrow m')AFP}{\longrightarrow} \eta a_{\rm m'} + (1-\eta) a_{\rm m} \ ,$$

$$\Delta P \equiv P_{A+} - P_{A-} \ , \text{ and}$$

$$\Delta A \equiv A_{A+} - A_{A-} \ .$$

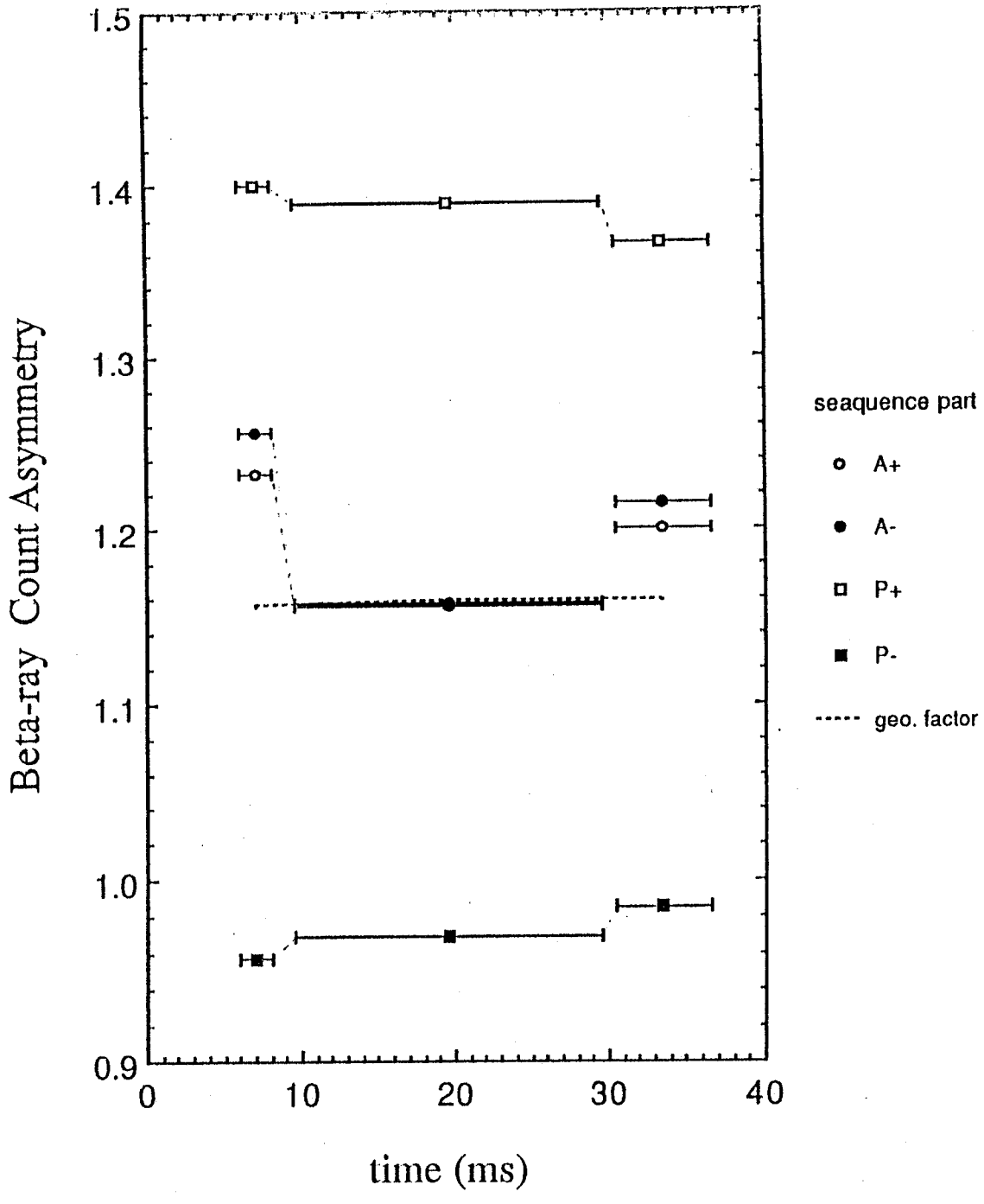

Figure 3.14: Achievement of the spin control. The vertical axis is the beta-ray asymmetry, defined as $(\frac{U}{D}) = \frac{\text{(upside counter's count)}}{\text{(downside counter's count)}}$.

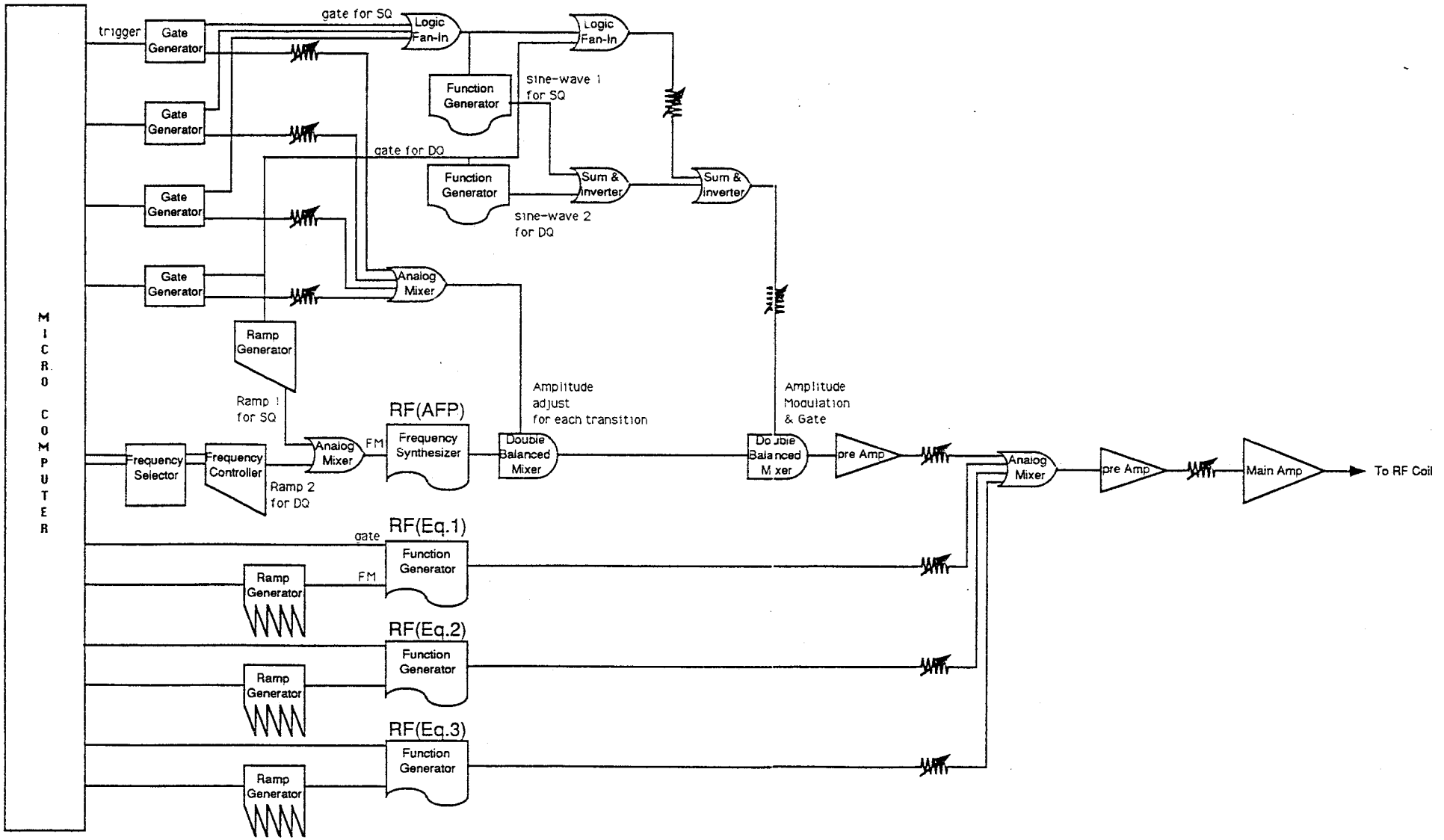

Figure 3.15: Schematic view of the circuit diagram for the RF system.

3.2.5 Control using a micro computer system

The control circuit and timing for the gate are shown in Fig.(3.16). The timing of the experiment was triggered by the monitor signal of the target rotor. Two photodiode sensors picked up the motion of the rotor and generated two trigger signals: 'rotor on' and 'rotor off'. When the target point of the rotor came around, at first the 'rotor on' signal was generated. Before opening the beam gate for beam bombardment, the bin gate was closed in order to inhibit beta-ray counting for rejecting the background counts. A standard light pulse from an LED was then emitted and detected by the E-counter for gain stabilization. By comparing the pulse height and standard level, the gain could be corrected. After the photo-multipliers for the E-counters were blocked by switching a high voltage, the pulse height spectra for the LED standard pulse were analysed by ADC and the data were stored in the computer as counts in count section IV(see Fig.(3.13)). The micro computer system then suspended the data-taking. As the last step of this series of processes, the beam from the accelerator was turned on by releasing the electrostatic chopper.

The production time, *i.e.*, the beam-on time, lasted until the 'rotor off' signal was detected. The signal 'rotor off' stopped the beam by the electrostatic deflector, released photomultiplier blocking, started beta-ray counting by opening the bin gate, and restarted data-taking by the computer. After restarting the computer, the computer controls both data-taking and the RF system according to the programmed timing based on its own clock. One experimental cycle comprised five parts with different data-taking sections, as shown in Fig.(3.13)

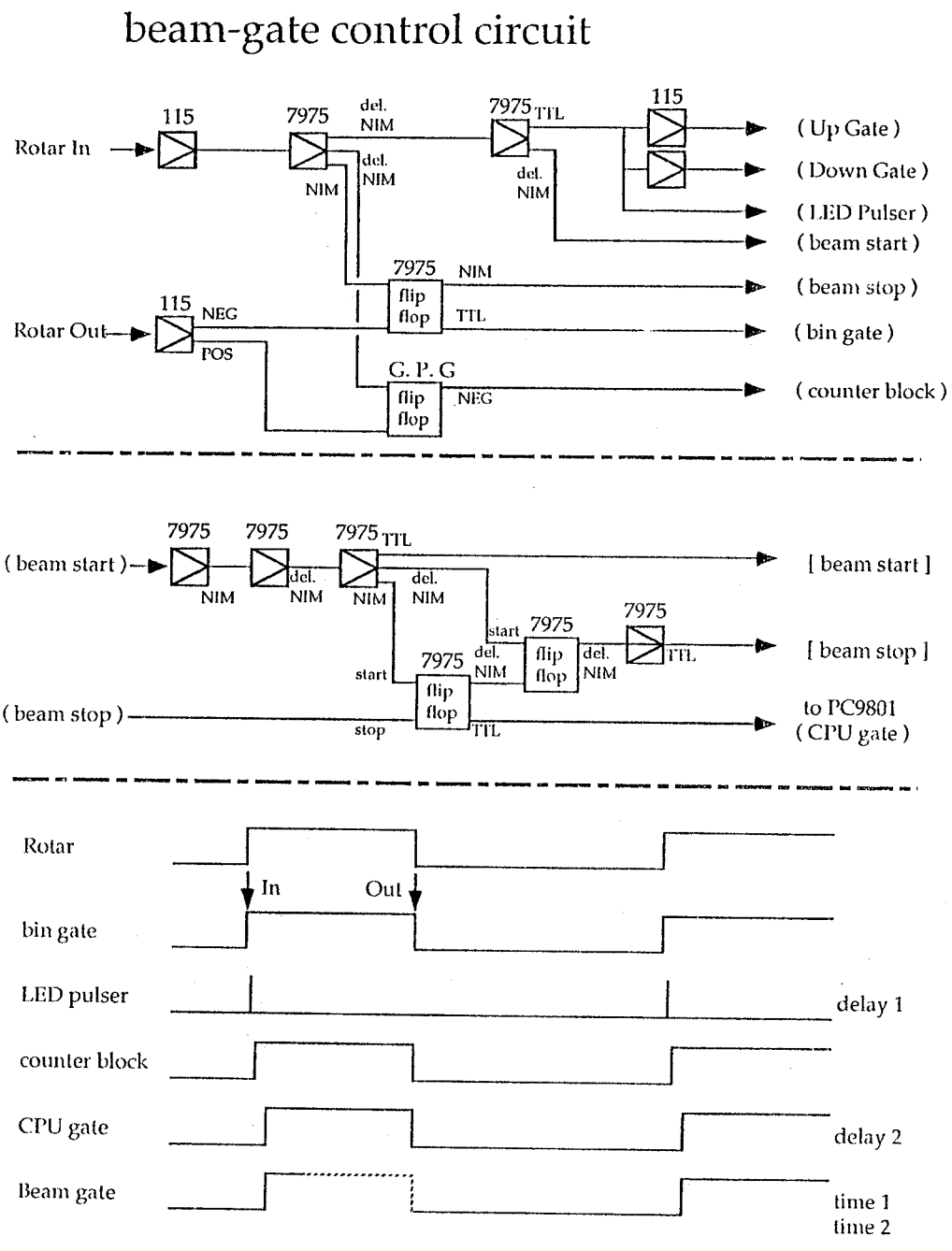

Figure 3.16: The upper figure is a schematic view of the circuit diagram for the beam and data-taking system by computer control. The lower figure is the timing of the gates for the beam, counter blocking and the initiation of data-taking.

3.3 Measurement of the Beta-ray Energy Spectra

3.3.1 Beta-ray detector

The beta rays emitted from ^{12}B and ^{12}N were detected by two sets of plastic scintillation counter telescopes placed above and below the Mg stopper. Fig.(3.17) shows a schematic view of a set of the beta-ray counter telescopes used in observations of the beta-ray energy spectra.

The beta-ray energy was measured by an E-counter, a scintillator of $152mm$ in diameter and $190mm$ in length attached to a photo multiplier of $127mm$ in diameter. For precise observations of the small correlation coefficient, the amplifier gain in the beta-ray detection system must be very stable. The stability of the energy counters was mainly dependent upon the stability of the photo multiplier gain against fluctuations in the temperature and counting rate. In the present experiment a pulse-height-gain-stabilizer was used in the amplifier system for gain stabilization. The standard light pulse was fed by an LED pulsar maintained at a constant temperature by a heater. Since, the counting rate might be sufficiently large during the beam-on time to saturate the phototube, the photo multiplier was blocked during this period by switching the high voltage for a dynode so as not to amplify the photo electrons. The stability of the counter system was monitored by the center of gravity of the standard pulse and the beta-ray-energy spectrum, as shown in Fig.(3.18).

Two ΔE counters were placed in front of the E-counter in order to define the solid angle of the beta rays. One of the ΔE counters (called B) was a scintillator of 55 mm in diameter and 1 mm in thickness attached to a 2-inch photo multiplier by a plastic light

guide (1mm in thickness and 150mm in length). Another ΔE counter (called B') was a scintillator of 80 $\times$ 80 mm and 1 mm in dimension. The counter's efficiency was very close to 100%. The accidental triple coincidence rate of E and two ΔE counters was negligible.

If beta rays from the catcher were scattered before being detected by the E-counter, the beta-ray energy spectra became distorted. In order to reject beta-ray scattering, the structures around the catcher and the detector were as much as possible made of materials with small Z. The walls of the reaction chamber were made of plastic, and the beta-ray windows were made of thin 50μm thick Capton foils. The magnets used for the external static field had only return yokes without any pole piece. The magnet coil and the RF coil used for the NMR technique were made of Aℓ wire instead of Cu wire. Besides, in order to reject the beta rays scattered by the return yokes, anti-coincidence counters (called C) were placed at the surfaces of the yokes. One set of the anti-coincidence counters comprised two annular scintillators and a cone-shaped scintillator. The light pulse from the cone-shaped scintillator was sent to photomultipliers through two fish-tail-type plastic light guides. The signals of the anti-coincidence comprised the sum of signals from two photo multipliers; as a result, a good detection efficiency was obtained.

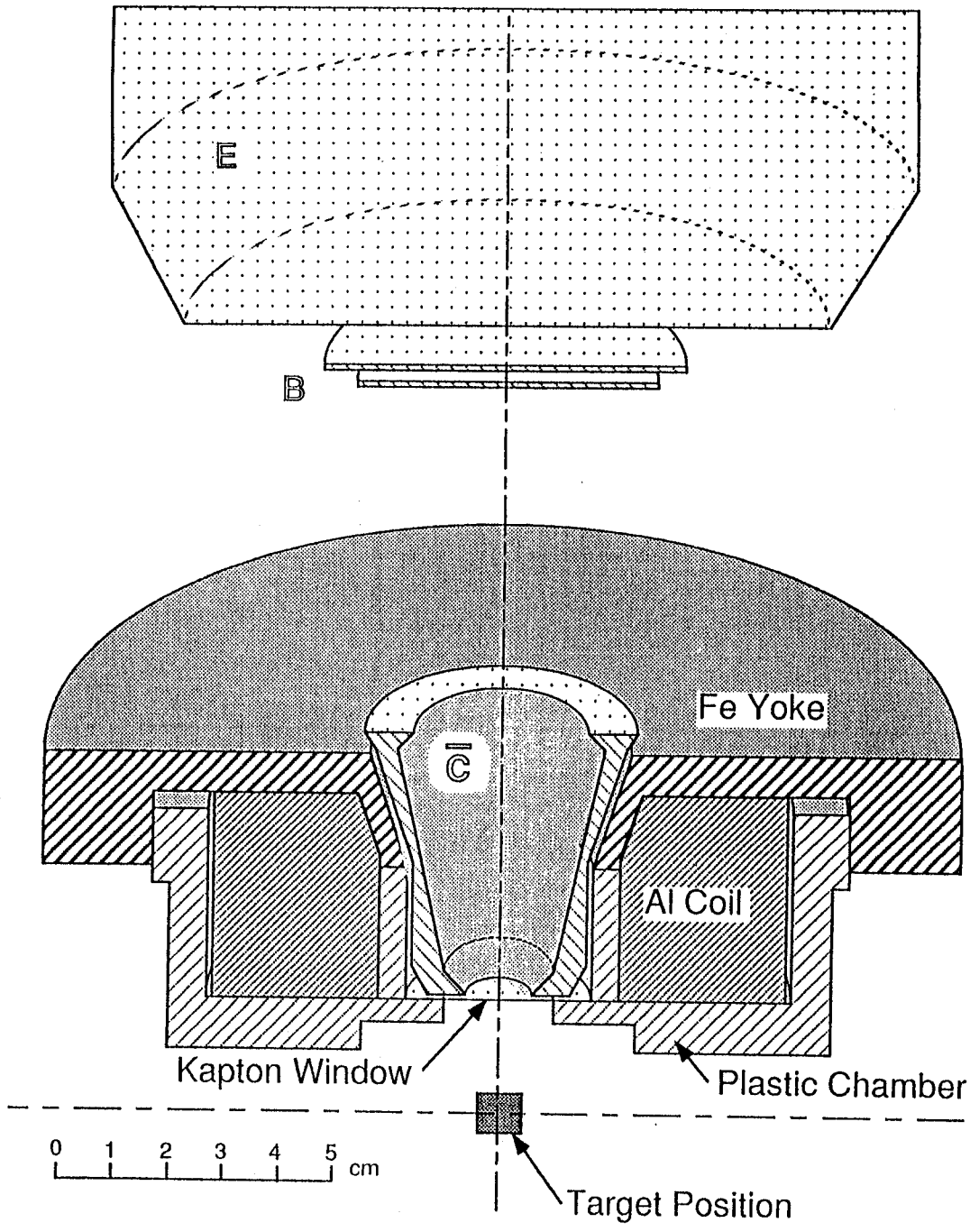

Figure 3.17: Schematic view of the beta-ray counter-telescope, the magnet and the vacuum chamber. The magnet comprised an iron yoke, an alminium coil and a plastic chamber. The anti-coinsidence 'C' counter rejects any scattered beta rays. The vacuum chamber is made of the plastic in order to prevent any beta rays from scattering.

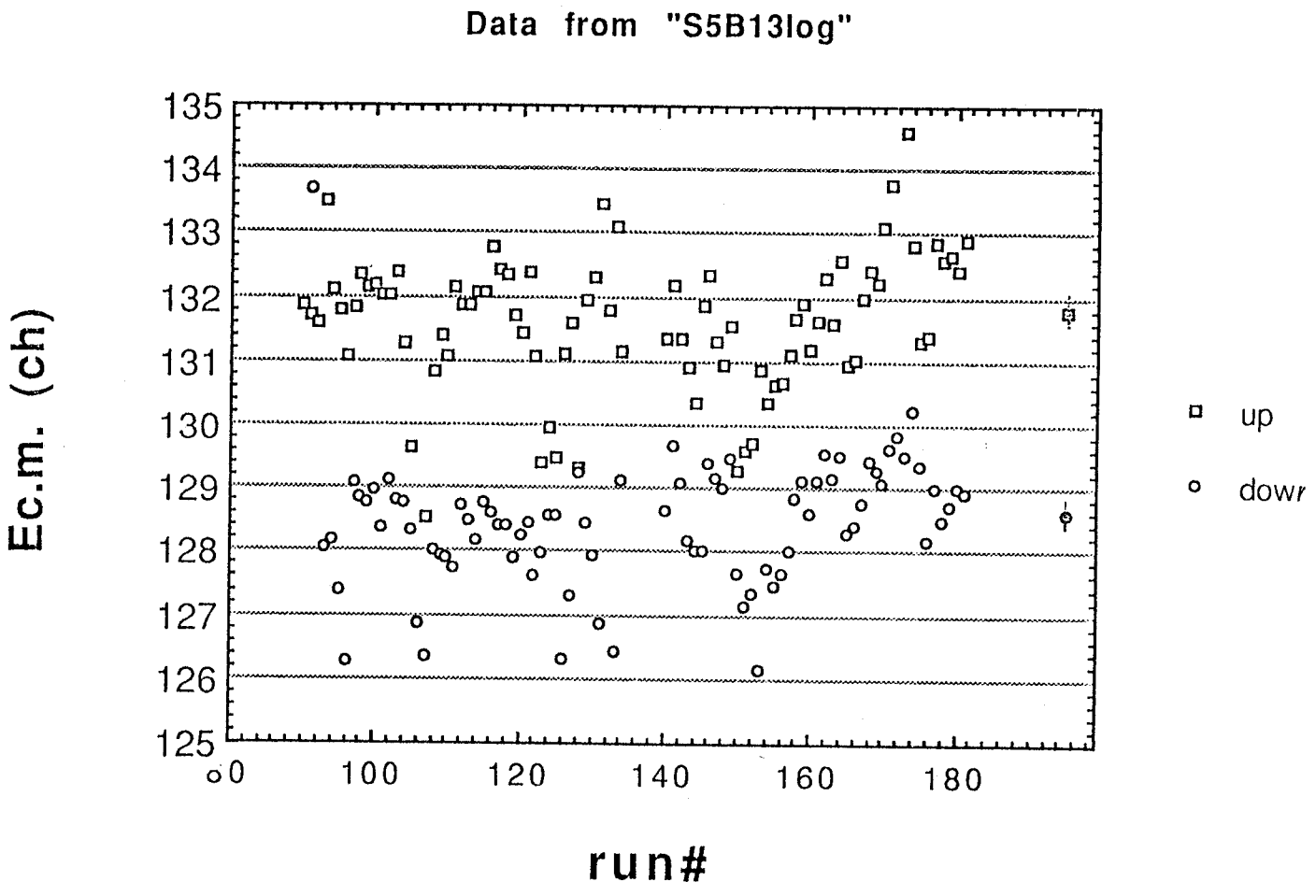

Figure 3.18: Stability of the beta-ray pulse height shown as the gravity of the pulse-hight spectrum as a function of time.

3.3.2 Electronics

In order to observe the beta-ray energy spectra, the pulses from the E-counter photomultipliers were amplified and measured. The electronic-circuit systems used to carry out these measurements are shown in Fig.(3.19)

The logic circuit used to trigger the beta-ray energy measurement mainly comprised a five-fold coincidence from four kinds of beta-ray counters (B, B', E and $\overline{C}$) as well as pile-up rejection. A four-fold coincidence ($B' \times B \times E \times (\overline{C_1+C_2})$) of the ΔE and the E-counters was produced and an anti-coincidence signal ($\overline{C_1+C_2}$) from the sum of the two anti-coincidence counter signals and the B and B' counters defined the solid angle of the beta rays; the C counter rejected scattered beta rays. The coincidence signal was then inhibited by a signal from the B' counter of other side to partially reject the cosmic ray. The final trigger signal was produced from the counter-coincidence signal as well as the pile-up rejection inhibit and the ADC busy inhibit. When a double pulse determined by the integration time for the signals from E-counters which occurred in E-counter of closer than 500ns, a pile-up rejection signal was generated which killed both events. In order to make this possible, logic signals from the B, B' and C counters were delayed by about 500 ns. Since the conversion time for ADC was about 5 μs/event, an ADC busy signal of 5μs duration killed any events which occurred within 5 μs after the event.

The analogue signal circuit mainly comprised linear gates and a gain stabilizer system. Any pulse from the E-counter was clipped by a delay line to a 170 ns width. The E-signal for a true event passed through a linear gate opened by the logic trigger for 470 ns. The true pulse was amplified by a spectroscopic amplifier and then sent to an ADC.

False pulses, including beta rays with an undefined solid angle, scattered beta rays, true pulses piled up, and true pulses during the ADC busy condition were rejected by the linear gate. The standard LED pulse could pass the linear gate using its the own trigger. The LED trigger also opened the linear gate, and the standard pulse was fed back to the gain stabilizer through the linear gate stretcher.

The bin gate signal gated all discriminators and, thus, protected succeeding circuits. Details concerning the modules used in the present study and the conditions are listed in Table 3.4

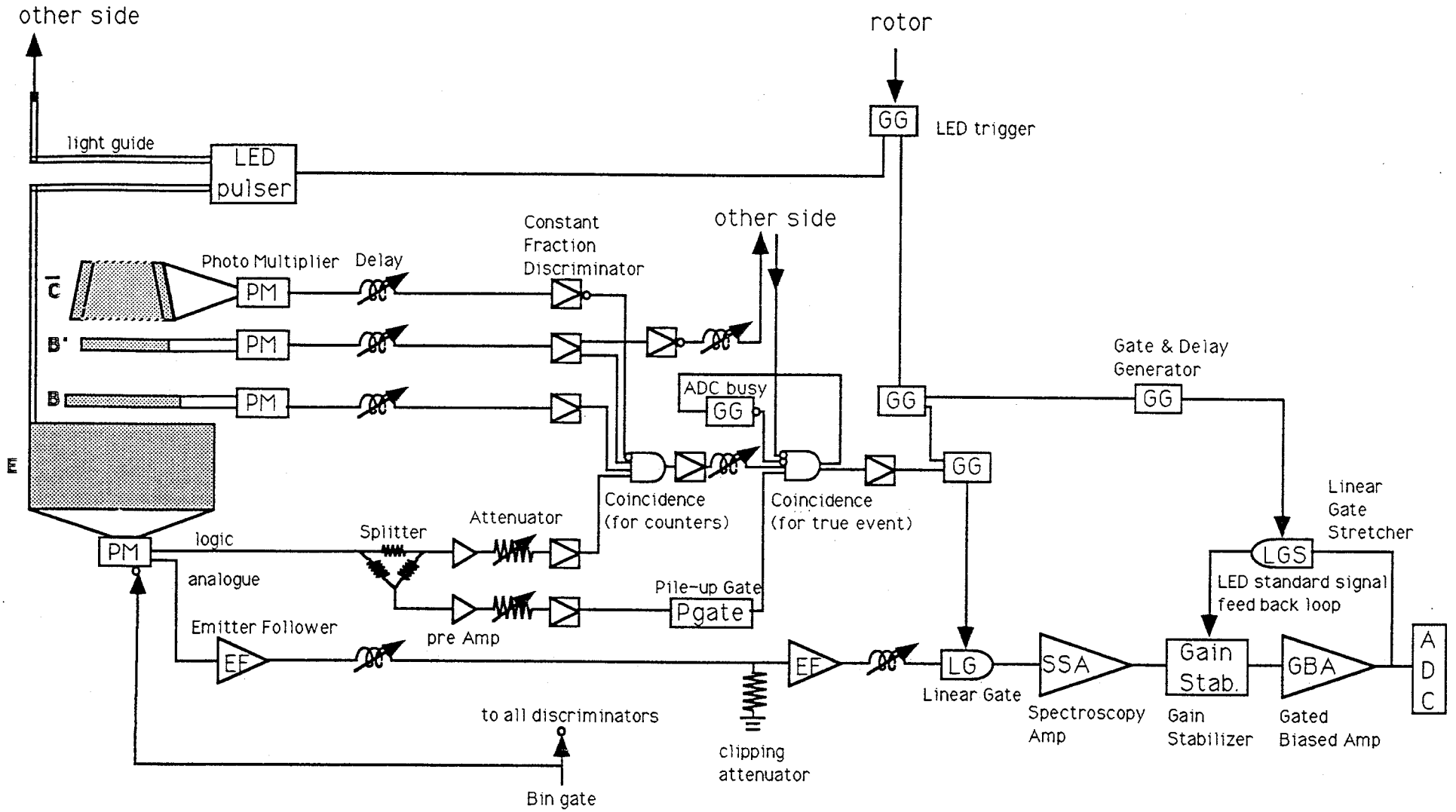

Figure 3.19: Schematic view of the circuit diagram for the beta-ray pulse prosessing system.

Table 3.4: Detector system modules and typical conditions

Modules	Type	Setting	conditions
Photomultiplier	Hamamatsu R329 (B',B)	H.V.	2500V
		^{90}Y output	7V
	Hamamatsu R329 (C)	H.V.	2500V
		^{90}Y output	3V
	Hamamatsu R1250 (E)	H.V.	1700V
	(modified breeder)	^{90}Y output	100mV
Discriminator	ORTEC QFD934 (B')	level	-30mv
		width	7ns
	ORTEC QFD934 (B)	level	-30mv
		width	10ns
	ORTEC QFD934 (E)	level	-30mv
		width	17ns
	ORTEC QFD934 (C)	level	-30mv
		width	30ns
Pile-up gate	ORTEC GP100NL	width	470ns
ADC busy	OULNS7973	width	5μs
Linear Gate	ORTEC LG101NL	width	170ns
Spectroscopy Amp.	ORTEC SSA452	gain	30
		shaping time	0.5μs

3.3.3 Beta-ray energy spectra of ^{12}B and ^{12}N

The beta-ray energy spectrum is described by Eq. (2.51). When nuclei have no polarization and no alignment, Eq. (2.51) can be simplified as follows:

$$W(E) = \text{const.} \times pE(E_0 - E)^2 \times F(\pm Z, E)\{1 + R(E, E_0)\}(1 \mp \frac{8}{3}aE). \tag{3.9}$$

Since we observed the beta-ray kinetic energy, Eq. (3.9) can be transformed using the kinetic energy (E_k) as

$$\begin{aligned} W(E_k) &= \text{const.} \times E_k(E_k + 2)^{\frac{1}{2}}(E_k + 1)(E_{k0} - E_k)^2 \\ &\quad \times F(\pm Z, E_k)(1 + R(E_k, E_{k0}))\{1 \mp \frac{8}{3}a(E_k + 1)\}, \end{aligned} \tag{3.10}$$

with

$$E_k = (E - m_e)/m_e. \tag{3.11}$$

The E counters have a sufficient volume to stop energetic beta rays from ^{12}B and ^{12}N, *i.e.*, 13.4 and 16.3 MeV for ^{12}B and ^{12}N, respectively. When a beta ray is injected into the plastic scintillator and does not escape, it loses energy mainly through an electric excitation process. A part of this energy is lost by the bremsstrahlung process, large part of the bremsstrahlung escapes from the scintillator with part of the electron energy. Therefore, the energy spectrum of monochromatic beta rays has low-energy tail, as shown in Fig.(3.20), in addition to a peak equal to the incident kinetic energy. The low-energy tail can be approximated by an exponential function.

Part of the incident beta rays escape from the plastic scintillator by backscattering from the entrance surface. The escaped beta rays also have the same effect on the energy

deposition with the bremsstrahlung. When the escape process can be explained by the backscattering, the tail can be approximated by an exponential function.

The spectrum of the energy deposited in the counter for monochromatic beta rays is therefore described as

$$f(x, E_k) = (1 - r)\delta(x - E_k) + r \cdot Y(x - E_k) \exp\{\lambda(x - E)\}. \tag{3.12}$$

Here, E_k is the incident kinetic energy, r the ratio of the low-energy tail, and λ the dumping factor of the tail; $\delta(x)$ is a delta function and $Y(x)$ is a step function.

The response function of the counter is thus given by folding with an error function which is spread by the statistical fluctuation, as follows:

$$S(x, E) = \int f(y, E) \cdot \frac{1}{\sqrt{2\pi}\sigma} \exp\{-\frac{(x - y)^2}{\sigma^2}\} dy. \tag{3.13}$$

The theoretical response function ($S(x, E)$) contains three parameters (r, λ, and σ). The width (σ) depends on the efficiencies of light emission in the scintillator, photo-electron emission at the photo cathode, or secondary electron reproduction at the dynode in the photomultiplier. In the present analysis, σ is determined from fitting spectrum. In a previous experiment, the actual response function was measured using monochromatic beta rays created by analyzing the beta rays emitted from beta-emitting nuclei, as shown in Fig.(3.21). From the results, the parameters of the response function are known to be

$$\lambda = 0.411/MeV \tag{3.14}$$

and

$$r = 0.17. \tag{3.15}$$

Typical beta-ray energy spectra are shown in Fig.(3.22). The solid line is the theoretical shape which best fits the data; it includes the counter response function and the effects of beta-ray scattering. The energy scale of the beta-ray energy spectrum was determined from the analysis of several beta emitters with a variety of end point energies.

Energy calibration and linearity

In the present analysis of the beta-ray energy spectra, determination of the energy scale is most important, since the observed ratio of the spectrum with positive alignment to the spectrum with negative alignment is given as the product of the alignment coefficient, the degree of alignment and the beta-ray energy. Therefore, the energy calibration directly affected the magnitude of the alignment coefficient. Most of the other effects could be canceled by comparing the data with a positive alignment and that with a negative alignment, measured under the same conditions, except for their alignment. In order to determine the absolute energies of the beta rays emitted from a nucleus in the present experiment, several other beta emitters were produced and measured at the same time.

Since the observed energy spectrum was analyzed using the theoretical functions in Eqs. (4.71) and (4.76), at least four unknown parameters (the pulse height at the end point of beta ray spectrum, the pulse height at the energy equal zero, the dispersion of statistical fraction, and the normalization constant) were determined. The zero energy, dispersion, and normalization constant are related to each other. However, the pulse height of the beta rays with end-point energies was almost independent of the other parameters. Moreover, the pulse height had only a small dependence on beta-ray scattering. Because, the scattering near the end point mainly caused a simple reduction of spectrum due to the

scattering out.

The spectrum of ^{12}B required an energy calibration below 13.4 MeV; for ^{12}N it was below 16.3 MeV. The beta emitters for the calibration were those for which their end points were near to the centroid of the spectrum of ^{12}B beta decay. In addition to these, in order to consider the difference in the electron and positron, the ^{12}B and ^{20}F electron emitters were used for ^{12}B. The ^{12}N, ^{41}Sc and ^{17}F positron emitters were used for ^{12}N. As already described, the targets were evaporated on the end part of the target backing. In order to switch the beam position from the main target (^{11}B or ^{11}B) to this part for a correlation, only the timing of the beam pulsing was readjusted. The energy calibration was thus perfectly carried out without changing the other conditions.

As energy scaling was obtained, the scale linearity was also checked. In the present experiment, by using the special target system for producing ^{12}N, ^{8}B, ^{41}Sc, ^{29}P, and ^{17}F, the end point energies could be measured in order to check the linearity of the positron detection. For this purpose, the rotating target system carried five different targets (^{10}B, ^{6}Li^{19}F, ^{40}Ca^{16}O, and ^{28}Si); ^{2}H and ^{3}He were used as incident beams. Fig.(3.23) shows the pulse height at the end point of beta-ray spectra. The good linearity was maintained over the energy region from 3 to 16 MeV.

For electron decay, ^{12}B, ^{20}F, and ^{90}Y were used. The target was the same as that used in the main run; the ^{90}Sr source was used as ^{90}Y . However, since ^{90}Y couldn't be set under the same conditions as the other short-lived emitters, a sufficient check could not be obtained.

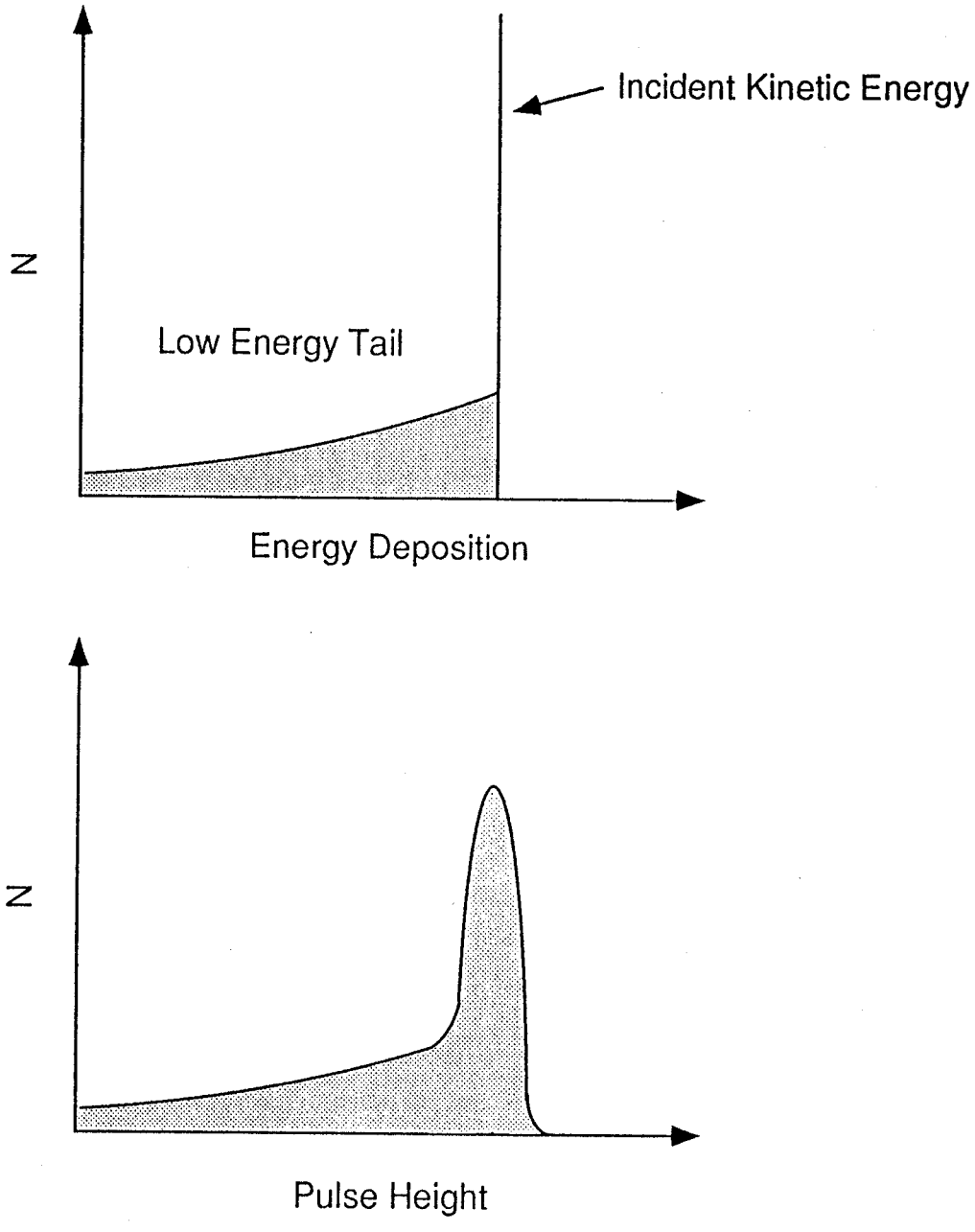

Figure 3.20: The upper figure is the energy deposition of monochromatic beta rays in the plastic scintillator. The lower figure is the responce function for the monochromatic energy of the beta rays.

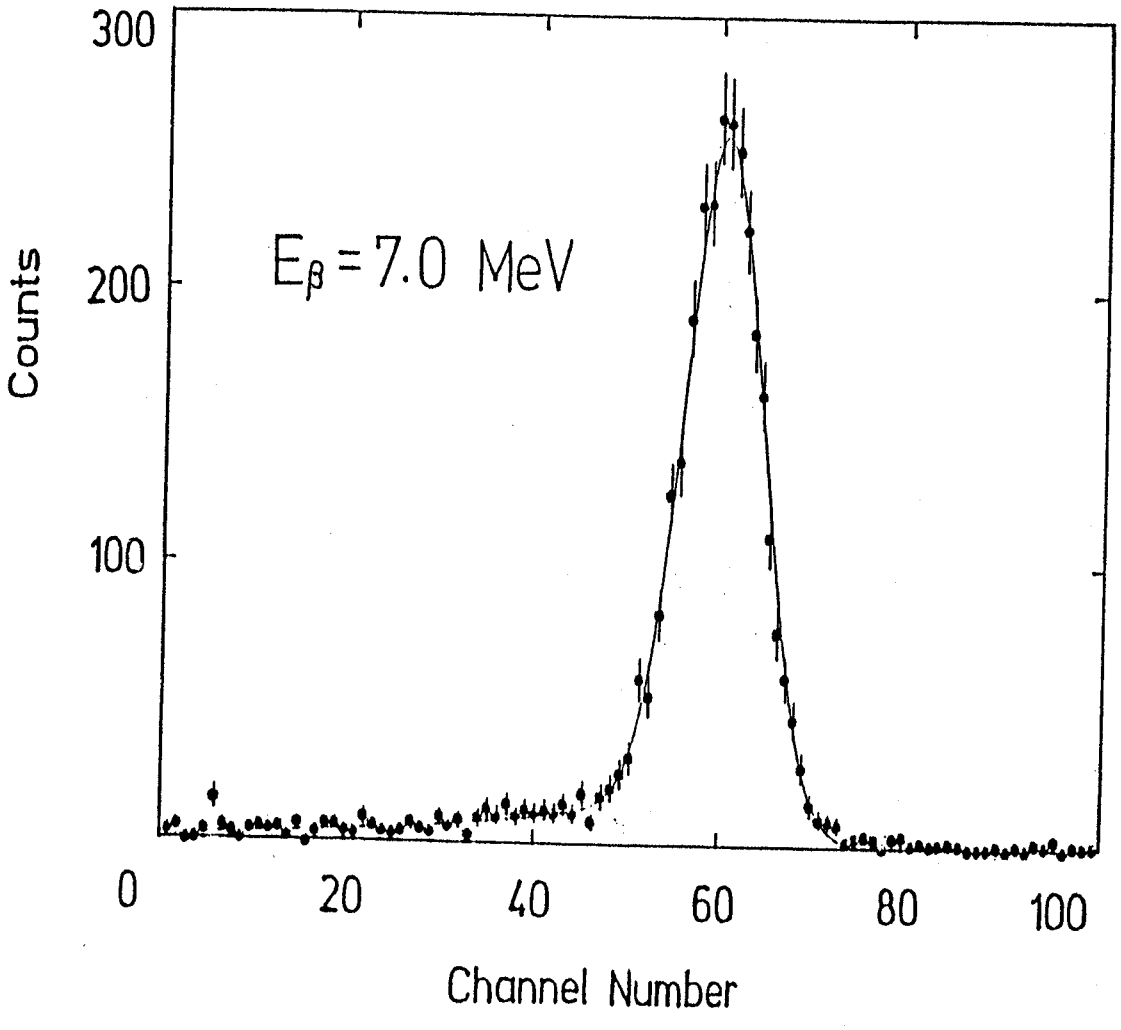

Figure 3.21: Typical observed energy spectrum for monochromatic beta rays. The beta-ray energy was 7 MeV. The beta rays were produced from the decay of ^{12}N, and separated by the analyzer magnet.

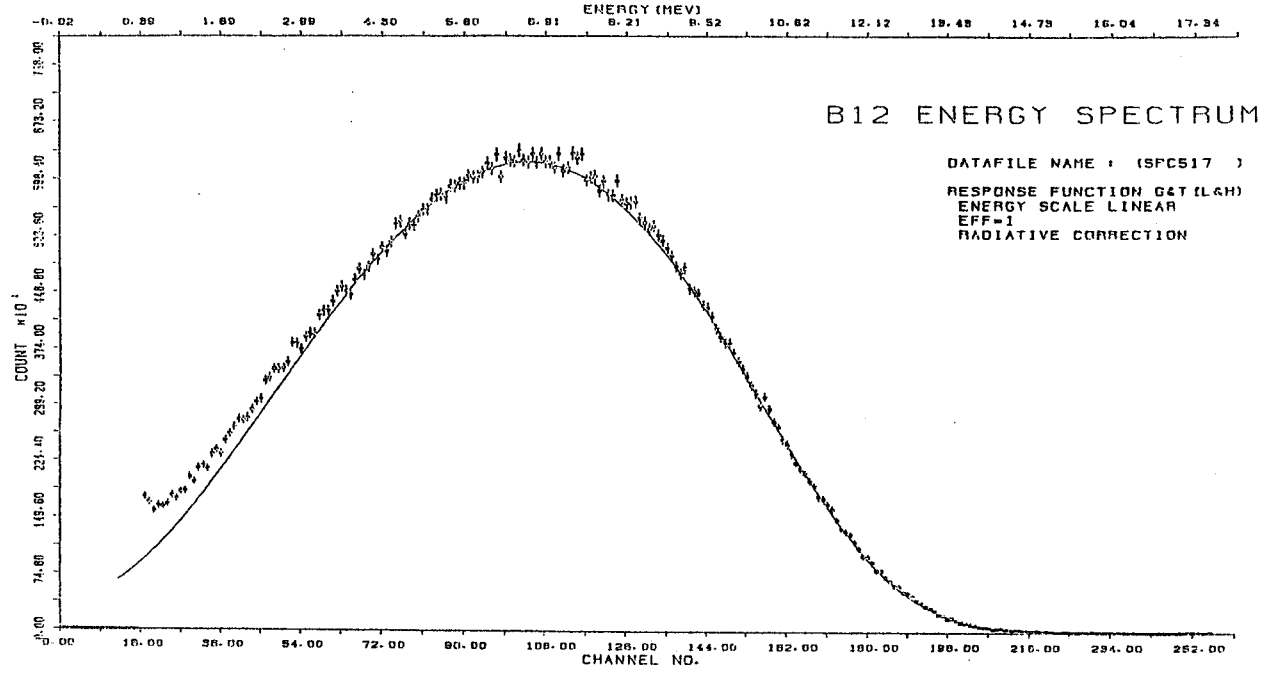

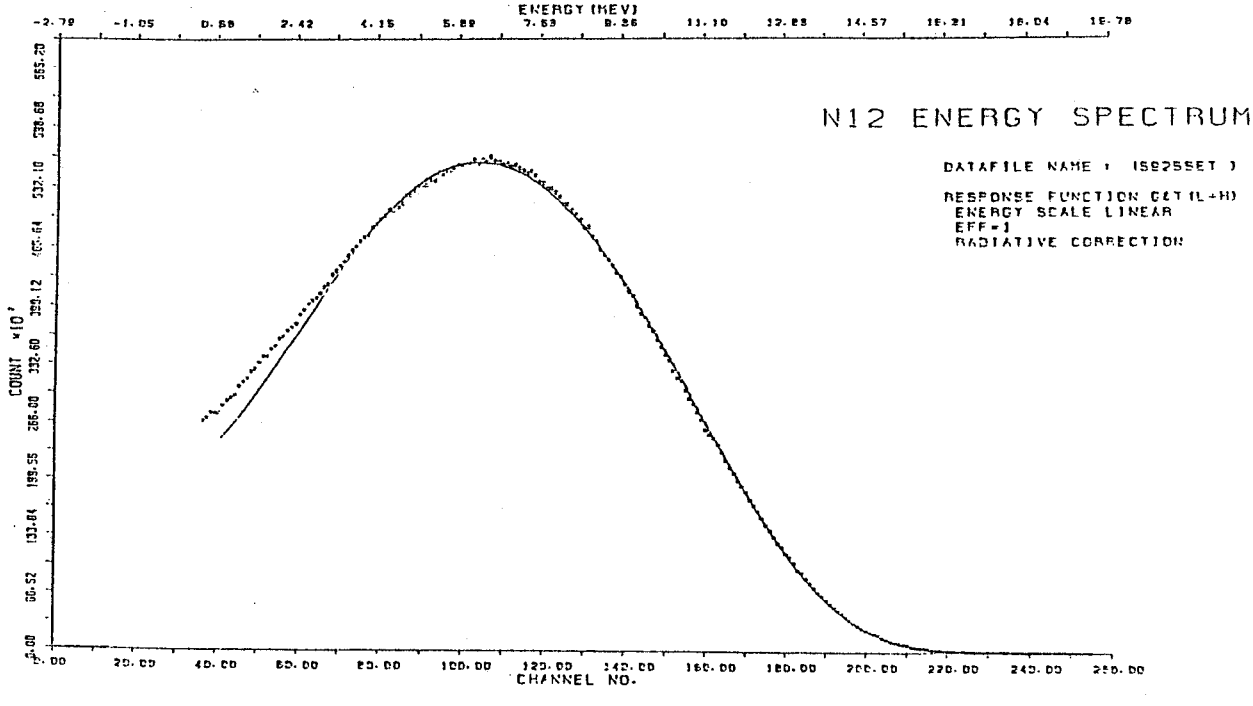

Figure 3.22: Typical observed beta-ray energy spectrum. The solid line is a theoretical fit.

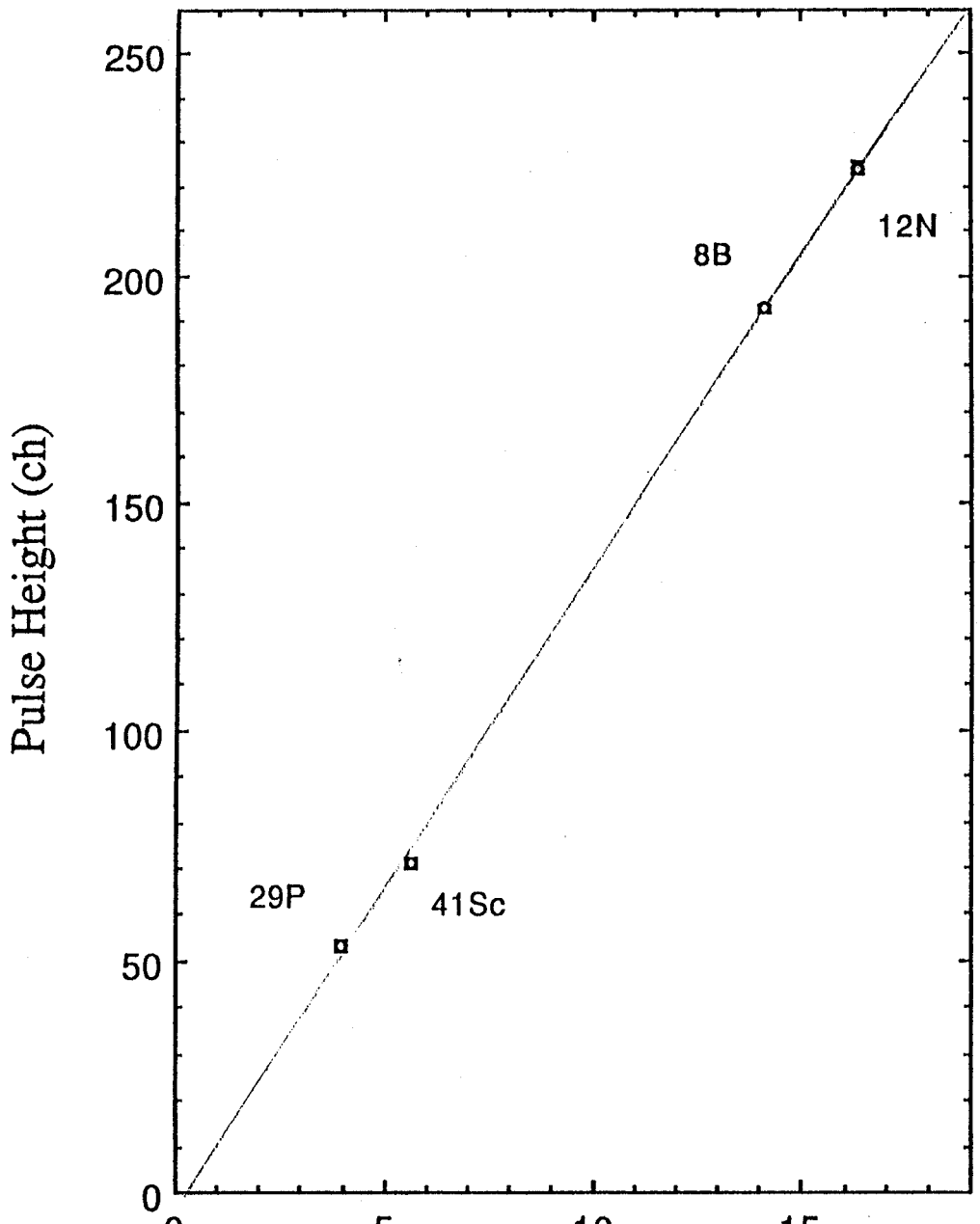

Figure 3.23: Linearity of the pulse height as a function of the beta-ray energy.

Chapter 4

Data Analysis

4.1 Principle of Analysis

From Eq. (2.51) the beta-ray energy spectrum ($N(E)$) at $\theta = 0$ with finite P and A is described using

$$N(E, P, A) = N_0[1 \mp P(p/E)(1 + \alpha_{\mp}E) + A\alpha_{\mp}E]S(E). \tag{4.1}$$

Here, $S(E)$ is the spectral shape function and N_0 is the normalization factor. The subscript of coefficient α corresponds to the sign of the $\beta^{\mp}$-decays. If the spectrum (N) is observed for both the positive alignment $+A$ and the negative alignment $-A$ with zero polarization, N_0 and $S(E)$ cancel each other in ratio $R(E)$ of $N(E, 0, +A)$ to $N(E, 0, -A)$,

$$R(E) \equiv \frac{N(E, 0, +A)}{N(E, 0, -A)} = \frac{1 + A\alpha_{\mp}E}{1 - A\alpha_{\mp}E}. \tag{4.2}$$

The product $\alpha_{\mp}$ is thus given by

$$\alpha_{\mp}E = \frac{1}{A}\frac{R(E) - 1}{R(E) + 1}. \tag{4.3}$$

Therefore, if $N_{(+A)}$ and $N_{(-A)}$ are measured as functions of E, $\alpha_{\mp}$ can be determined.

In actual experiments the residual polarizations ($P_{\pm}$) were small, but finite, and the absolute value of the positive alignment (A_+) was not equal to that of the negative alignment (A_-). The exact expression of $R(E)$ is therefore given by

$$R(E) = \frac{N(E, P_+, A_+)}{N(E, P_-, A_-)} = \frac{1 \mp P_+(1 + \alpha_{\mp}E) + A_+\alpha_{\mp}E}{1 \mp P_-(1 + \alpha_{\mp}E) + A_-\alpha_{\mp}E}. \tag{4.4}$$

As a result, the energy-dependent alignment-correlation term ($\alpha_{\mp}E$) is given by

$$\alpha_{\mp}E = \frac{[1 \mp P_+(1 + \alpha_{\mp}E)] - R(E)[1 \mp P_-(1 + \alpha_{\mp}E)]}{R(E)A_- - A_+}. \tag{4.5}$$

The residual polarizations (P_+ and P_-) are not usually exactly zero, due to the imperfect spin control in converting the polarization into a large alignment, and, by the minority's sites of the ^{12}B and ^{12}N in the Mg catcher crystal. P_+ and P_- have the same sequence of spin control, and only their achievements of AFP(SQ transition) are different from each other. Especially, according to the control of the sub populations, both residual polarizations are the same. Thus, in the present experiment, P_+ and P_- satisfy the following conditions:

$$P_+ \sim P_- \tag{4.6}$$

and

$$|\Delta P| < 0.01, \qquad (\Delta P \equiv P_+ - P_-). \tag{4.7}$$

Since $\alpha_{\mp}$ is at most 0.3%, the $\alpha_{\mp}E$ term in the polarization correlation term is negligible,

$$|\Delta P \alpha_{\mp}E| \leq 5 \times 10^{-4}. \tag{4.8}$$

Using these approximations, Eq.(4.5) can be described by a simple use of these approximations,

$$\alpha_{\mp}E = \frac{1 - R(E) \mp \Delta P}{R(E)A_{-} - A_{+}}. \tag{4.9}$$

Eq.(4.9) still includes a small effect caused by the residual polarization. In order to cancel this effect, $R(E)$ was observed at $\theta = \pi$ at the same time. Ratios $R_u(E)$ and $R_d(E)$ are for $\theta = 0$ and $\theta = \pi$, respectively; $\alpha_{\mp}E$ can thus be written as

$$\alpha_{\mp}E = \frac{1 - R_u(E) \mp \Delta P}{R_u(E)A_{-} - A_{+}} \tag{4.10}$$

and

$$\alpha_{\mp}E = \frac{1 - R_d(E) \pm \Delta P}{R_d(E)A_{-} - A_{+}}. \tag{4.11}$$

Since the polarization term has opposite signs for R_u and $R_d(E)$, while the alignment term has the same sign, the effect of the residual polarization (P) is canceled in the simple sum of these equations, as follows:

$$\alpha_{\mp}E = \frac{1}{2}\left[\frac{1 - R_u(E)}{R_u(E)A_{-} - A_{+}} + \frac{1 - R_d(E)}{R_d(E)A_{-} - A_{+}}\right]. \tag{4.12}$$

Noting that $R_u(E)$ and $R_d(E)$ are close to 1, *i.e.*, $(R(E) - 1) \leq 2\%$, Eq.(4.12) is almost the same as

$$\alpha_{\mp} = \frac{1}{2}\frac{1}{\Delta A}(1 - R_u(E) + 1 - R_d(E)). \tag{4.13}$$

with

$$\Delta A \sim A_{-} - A_{+} \tag{4.14}$$

Thus, $\alpha_{\mp}E$ does not strongly depend on the absolute value of A_{+} and A_{-}, but depends on the difference.

From Eq.(4.13), we can obtain the alignment correlation coefficient ($\alpha_{\mp}$) as a function of the beta-ray energy. To use the energy-dependent coefficients ($B_0(E)$ and $B_2(E)$) in Eq.(2.64), the alignment correlation term $\left[\frac{B_2(E)}{B_0(E)}\right]$ can be described as follows:

$$\left[\frac{B_2(E)}{B_0(E)}\right] = \frac{1}{2}\frac{1}{\Delta A}(1 - R_u(E) + 1 - R_d(E)). \tag{4.15}$$

4.2 Determination of the Alignment

From the requirement given in Eq.(4.12), we must determine the degree of alignment in the experiment. Since the alignment term is very small, and is a value that must be determined experimentally, this term cannot be used for the determination. In our experiment, large alignments were produced from the large initial polarization by spin manipulation. Since the polarization term is sufficiently large to be easily observed, the degree of alignment can be easily deduced from the polarization.

4.2.1 Observation of polarization

From Eq.(4.1), the ratio of the beta-ray counts (U) for the upside detector at $\theta = 0$ to the D for the downside detector at $\theta = \pi$ can be described as

$$\left(\frac{\mathrm{U}}{\mathrm{D}}\right) = \frac{\int g_u\{1 \pm P(p/E)(1+\alpha_\pm E) + A\alpha_\pm E\}S(E)dE}{\int g_d\{1 \pm P(p/E)(1+\alpha_\pm E) + A\alpha_\pm E} . \tag{4.16}$$

Where the g's are the geometrical factor of the detector system. Since, the g's most likely do not depend on the beta-ray energy, the ratio (g) of the g_u to g_d is constant. If g is known, P can be derived. Eq.(4.16) becomes

$$\left(\frac{\mathrm{U}}{\mathrm{D}}\right)_{(E)} = g\frac{1 \pm P\varepsilon}{1 \mp P\varepsilon}, \tag{4.17}$$

where

$$\varepsilon = \frac{< (p/E)(1+\alpha_\pm E) >}{1 + < A\alpha_\pm E >} . \tag{4.18}$$

Here, the notation $< >$ indicates an average over the analysis region. P thus becomes

$$P = \mp\left(\frac{1}{\varepsilon}\right)\frac{\left(\frac{\mathrm{U}}{\mathrm{D}}\right) - g}{\left(\frac{\mathrm{U}}{\mathrm{D}}\right) + g} . \tag{4.19}$$

Since $|1-\varepsilon| < 10^{-2}$ in the present experiments, $(1-\varepsilon)$ is negligible for measurements of $\alpha_{\mp}$. The polarization is thus given by

$$P = \mp \frac{\frac{U}{D} - g}{\frac{U}{D} + g}. \tag{4.20}$$

Determination of the geometrical asymmetry (g)

When the DQ transition between magnetic substates $m = +1$ and $m = -1$ is obtained, the initial polarization (P) is converted to $-P$ (see section 3.2.1). The observed asymmetry is described as follows:

$$\begin{aligned} \left(\frac{\mathrm{U}}{\mathrm{D}}\right)_+ &= g\frac{1+P_0}{1-P_0} \\ \left(\frac{\mathrm{U}}{\mathrm{D}}\right)_- &= g\frac{1-P_0}{1+P_0}. \end{aligned} \tag{4.21}$$

Here, $\left(\frac{\mathrm{U}}{\mathrm{D}}\right)_+$ is the initial asymmetry and $\left(\frac{\mathrm{U}}{\mathrm{D}}\right)_-$ is the asymmetry for a spin ensemble with a conversion of $m = +1 \leftrightarrow m = -1$. P can be thus reduced, as follows:

$$\left[\left(\frac{\mathrm{U}}{\mathrm{D}}\right)_+ - g\right]\left[\left(\frac{\mathrm{U}}{\mathrm{D}}\right)_- + g\right] = \left[\left(\frac{\mathrm{U}}{\mathrm{D}}\right)_+ + g\right]\left[\left(\frac{\mathrm{U}}{\mathrm{D}}\right)_- - g\right]. \tag{4.22}$$

Further, g is given as a solution of the following quadratic equation:

$$g^2 + \left[\left(\frac{\mathrm{U}}{\mathrm{D}}\right)_+ - \left(\frac{\mathrm{U}}{\mathrm{D}}\right)_-\right]g - \left[\left(\frac{\mathrm{U}}{\mathrm{D}}\right)_+ \times \left(\frac{\mathrm{U}}{\mathrm{D}}\right)_-\right] = 0. \tag{4.23}$$

Actually, the conversion of $m = +1 \leftrightarrow m = -1$ was not perfect. The achievement of the DQ transition is defined as

$$P' \equiv \alpha P_0. \tag{4.24}$$

To use this definition, Eq.(4.21) is described as follows:

$$\begin{aligned} \left(\frac{\mathrm{U}}{\mathrm{D}}\right)_+ &= g\frac{1+P_0}{1-P_0} \\ \left(\frac{\mathrm{U}}{\mathrm{D}}\right)_- &= g\frac{1+\alpha P_0}{1-\alpha P_0}, \end{aligned} \tag{4.25}$$

and the quadratic equation of g is

$$g^2 + \left[\frac{\alpha+1}{\alpha-1}\left\{\left(\frac{\mathrm{U}}{\mathrm{D}}\right)_+ - \left(\frac{\mathrm{U}}{\mathrm{D}}\right)_-\right\}\right] g - \left[\left(\frac{\mathrm{U}}{\mathrm{D}}\right)_+ \times \left(\frac{\mathrm{U}}{\mathrm{D}}\right)_-\right] = 0. \tag{4.26}$$

Achievement of a double quantum transition

The achievement of spin control is usually defined by the degree of the population change of the relevant substates. Especially, in the case of spin $I = 1$, the double quantum transition (DQ) between the substates, $m = +1 \leftrightarrow -1$, exchanges only the populations (a_{+1} and a_{-1}). The achievement of DQ is therefore defined by the polarization P,

$$\alpha \equiv \frac{P_f}{P_i} \tag{4.27}$$

with

$$P = a_{+1} - a_{-1}. \tag{4.28}$$

When spin control is perfectly obtained, $\alpha = -1$; Figure (3.13) shows the sequence for obtaining this situation.

In this sequence, the up-down ratios are given by

$$\begin{aligned} R_0 &= g\frac{1+P}{1-P}, \\ R_1 &= g\frac{1+\alpha P}{1-\alpha P}, \end{aligned}$$

and

$$R_2 = g\frac{1+\alpha^2 P}{1-\alpha^2 P}, \tag{4.29}$$

where, R_0, R_1 and R_2 can be experimentally measured, so that P, g, and α can be determined.

Achievement of a single quantum transition

The determination method for the AFP achievement of single quantum transitions (SQ) is different from that for DQ. However, its determination was necessary in order to find the degree of the alignment. The AFP of SQ transitions exchanges the populations between $\Delta I = 1$, $m = +1 \leftrightarrow 0$ or $m = -1 \leftrightarrow 0$. The observable polarization is described using the initial populations (a) and final polarization (a'), where a_{+1},a_0 and a_{-1} are defined as the populations of the magnetic substates ($m = +1, 0, -1$), as follows:

$$a_{+1} + a_0 + a_{-1} = 1 \tag{4.30}$$

$$P_0 = a_{+1} - a_{-1} \tag{4.31}$$

and

$$\begin{aligned} P_1 &= a'_{+1} - a_{-1} \\ &= [\eta a_0 + (1-\eta)a_{+1}] - a_{-1}. \end{aligned} \tag{4.32}$$

Here, P_0 is the initial polarization and P_1 is the polarization after the SQ's AFP between $m = +1 \leftrightarrow 0$. The achieved η is the ratio of the exchanged population.

After controlling the SQ's AFP twice, the polarization is given by

$$\begin{aligned} P_2 &= a''_{+1} - a_{-1} \\ &= [\eta\{\eta a_{+1} + (1-\eta)a_0\} + (1-\eta)\{\eta a_0 + (1-\eta)a_{+1}\}] - a_{-1}. \end{aligned} \tag{4.33}$$

The difference of Eqs. (4.31) and (4.32) reduce the uncontrolled population (a_{-1}); the difference of Eq. (4.31) and (4.33) is also

$$P_1 - P_0 = -\eta(a_{+1} - a_0) \tag{4.34}$$

and

$$P_2 - P_0 = 2\eta(\eta - 1)(a_{+1} - a_0). \tag{4.35}$$

The most important condition in the above equation is that even if the observed P includes some unknown polarization due to the existence of the minority, P is canceled in Eqs. (4.34) and (4.35). Therefore, the achievement(η) can be acquired from Eqs. (4.34) and (4.35) without any effect from the minority group,

$$\eta = 1 - \frac{1}{2}\frac{P_2 - P_0}{P_1 - P_0}. \tag{4.36}$$

4.2.2 Determination of the alignment from the observed polarization

Here, a_{+1}, a_0, a_{-1} are defined as the populations of the magnetic substates: $m = +1, 0, -1$. In the case of nuclei with spin $I = 1$, the polarization (P) and alignment (A) are given by these magnetic substate population (a_+, a_0 and a_-) respectively, as follows:

$$P = a_{+1} - a_{-1} \tag{4.37}$$

and

$$A = 1 - 3a_0. \tag{4.38}$$

P can be easily observed by detecting the asymmetry of the beta rays, while A cannot be measured directly. Measurements of the asymmetry change due to the polarization are necessary for a determination of the degree of alignment.

For this purpose, in the course of the present experiment three beta-ray count sections were used like Fig. (3.13). In section II, $P = 0$ and $A = +A$ were attained for

observations of the alignment correlation. Spin manipulation by the RF for the exchange of a_0 and a_{+1} was applied between each adjacent section. $\mathrm{RF_{I\to II}}$ converted the polarization into alignment, and $\mathrm{RF_{II\to III}}$ reconverted the alignment back to polarization.

The observed polarization at each sections is described as

$$P_{\mathrm{I}} = a_{+1} - a_{-1}, \tag{4.39}$$

$$P_{\mathrm{II}} = a_{+1} - a'_{-1} = a_{+1} - \{\eta a_0 + (1-\eta)a_{-1}\} \tag{4.40}$$

and

$$P_{\mathrm{III}} = a_{+1} - a''_{-1} = a_{+1} - \{2\eta(1-\eta)a_0 + (2\eta^2 - 2\eta + 1)a_{-1}\}. \tag{4.41}$$

The alignment (A_{II}) is given by

$$\begin{aligned} A_{\mathrm{II}} = 1 - 3a'_0 &= 1 - 3\{\eta a_{-1} + (1-\eta)a_0\} \\ &= (1 - 3a_{-1}) - 3(1-\eta)(a_0 - a_{-1}). \end{aligned} \tag{4.42}$$

In order to determine a_{-1} and a_0 from the observed P, Eqs. (4.39) and (4.40) were transformed as follows:

$$P_{\mathrm{II}} = (a_{+1} - a_0) + (1-\eta)(a_0 - a_{-1}), \tag{4.43}$$

$$\begin{aligned} P_{\mathrm{I}} &= \frac{1}{2}\{(a_{+1} + a_0) - 2a_{-1} + (a_{+1} - a_0)\} \\ &= \frac{1}{2}\{(1 - 3a_{-1}) + (P_{\mathrm{II}} - (1-\eta)(a_0 - a_{-1})\}, \end{aligned} \tag{4.44}$$

and

$$1 - 3a_{-1} = 2P_{\mathrm{I}} - P_{\mathrm{II}} + (1-\eta)(a_0 - a_{-1}). \tag{4.45}$$

From Eqs. (4.43) and (4.44), $A_{\rm II}$ is described by P and η only:

$$\begin{aligned} A_{\rm II} &= 2P_{\rm I} - P_{\rm II} - 2(1-\eta)(a_0 - a_{-1}) \\ &= 2P_{\rm I} - P_{\rm II} - 2(1-\eta)(P_{\rm I} + a_0 - a_{+1}) \\ &= 2\eta P_{\rm I} - P_{\rm II} + 2(1-\eta)(a_0 - a_{+1}) \end{aligned} \tag{4.46}$$

Under the experimental condition that $\eta \sim 1$ and $a_0 \sim a_{+1}$, since the third term of Eq. (4.46) can be neglected,

$$A_{\rm II} \sim 2\eta P_{\rm I} - P_{\rm II}. \tag{4.47}$$

Therefore, A is also given by the polarizations at sections II and III:

$$A_{\rm II} = \frac{2}{\eta} P_{\rm III} - P_{\rm II}. \tag{4.48}$$

$A_{\rm II}$ of Eq. (4.47) is the degree of the initial alignment at section II; $A_{\rm II}$ of Eq. (4.48) is the final one. If the populations don't change in section II, they are all equal. However, since the alignment and polarization are decreased by relaxation, the final A becomes smaller than the initial value. This relaxation effect was taken into account in determining P, *i.e.*, A.

4.2.3 Effect of the spin-lattice relaxation time

To account for the effective alignment in the beta-ray counting time sections, both the relaxation time for the alignment and that for polarization must be considered. The alignment with the relaxation time ($\tau = \frac{1}{\lambda}$) is described as

$$A(t) = A_i e^{-\lambda_A t}. \tag{4.49}$$

Here, A_i is the initial alignment; λ_A is the relaxation time of the alignment. The decay of nuclei is also described in terms of the lifetime (λ_ℓ) as follows:

$$N(t) = N_0 e^{-\lambda_\ell t}. \tag{4.50}$$

From Eqs. (4.49) and (4.50), the effective alignment (A_{eff}) at $t = 0 \sim t_c$ is described as follows:

$$\begin{aligned} A_{eff} &= \frac{\int_0^{t_c} A(t)N(t)dt}{\int_0^{t_c} N(t)dt} \\ &= \frac{\int_0^{t_c} A_i e^{-\lambda_A t} e^{-\lambda_\ell t} dt}{\int_0^{t_c} e^{-\lambda_\ell t} dt} \qquad (4.51) \\ &= \frac{\frac{1}{\lambda_A+\lambda_\ell}(A_i - A_i e^{-\lambda_A t_c} e^{-\lambda_\ell t_c})}{\frac{1}{\lambda_\ell}(1 - e^{\lambda_\ell t_c})}. \qquad (4.52) \end{aligned}$$

From Eqs. (4.47) and (4.48), the initial and final alignments of the count section can be observed. From the definition of λ_A,

$$\lambda_A = \frac{\ln(\frac{A_i}{A_f})}{t_c} \tag{4.53}$$

with

$$A_f \equiv A_i e^{-\lambda_A t_c} \tag{4.54}$$

The effective alignment can therefore be determined in terms of only the observable A as

$$A_{eff} = \frac{\lambda_\ell}{\ln(\frac{A_i}{A_f})/t_c + \lambda_\ell} \frac{A_i - A_f e^{-\lambda_\ell t_c}}{1 - e^{\lambda_\ell t_c}}. \tag{4.55}$$

4.3 Corrections and Errors

The alignment correlation coefficients were measured by observing the beta-ray energy spectra and by determining the alignment using the methods discussed in section 4.2.2. However, corrections due to several causes are necessary for the observed coefficient.

In the present work, the following corrections were considered: the solid angle of the beta-ray counters, the beta-decay branches to the excited states, the response function for the beta-ray counters, the beta-ray scattering, the background beta rays, (p/E) and the stability of the incident beam.

These corrections can be classified in terms of whether or not they depend on the beta-ray energy. The energy-independent corrections are listed in Table 4.1 and the total correction factors, including energy-dependent corrections, are listed in Table 4.2. In these descriptions, the correction factor (C) is defined as

$$\alpha_{\text{true}} = C\alpha_{\text{observed}}. \tag{4.56}$$

The systematic error (d) is defined as

$$\Delta\alpha_{\text{true}} = \sqrt{(\Delta\alpha_{\text{observed}})^2 + (d\alpha_{\text{observed}})^2}. \tag{4.57}$$

Table 4.1: Energy-independent correction factors.

	for ^{12}B		for ^{12}N	
	correction factor	error factor	correction factor	error factor
Solid angle	1.031	0.002	1.031	0.002
Decay branch	0.988	0.001	0.976	0.001
Relaxation of P and A	0.999	0.001	0.997	0.002
Background noise	1	0	0.978	0.01
Responce function	1	0.03	1	0.03
α_+	1	0	0.975	0.005
(p/E)	1	0	1	0
Energy independence	1.018	0.030	0.956	0.034

Table 4.2: Energy-dependent correction factors. The correction factors include the energy-independent correction factors given in Table (4.1).

E (MeV)	^{12}B	^{12}N
5.0	0.945	0.874
6.0	0.981	0.922
7.0	1.002	0.950
8.0	1.016	0.966
9.0	1.031	0.975
10.0	1.050	0.979
11.0	1.074	0.983
12.0	1.108	0.987
13.0	1.152	0.998
14.0	-	1.012
15.0	-	1.039
16.0	-	1.074

4.3.1 Correction for the finite solid angle of the beta-ray detectors

The beta-ray counters used in the present experiment had a finite solid angle, as shown in Figure (3.17). The degree of the observed polarization or alignment was corrected for the solid angle. The degree of polarization is thus given as

$$\begin{aligned} P_{obs} &= \frac{1}{\Omega}\int_{\Omega} P\mathrm{P}_1(\cos\theta)d\Omega \\ &= \frac{P}{\Omega}\int_0^{\theta_0} \cos\theta(2\pi\sin\theta d\theta). \end{aligned} \tag{4.58}$$

Here, $2\theta_0$ is the subtending angle of the telescope, which corresponds to the solid angle

$$\Omega = 2\pi(1-\cos\theta_0). \tag{4.59}$$

Thus, Eq. (4.58) is calculated to be

$$\begin{aligned} P_{obs} &= \frac{P}{2}\frac{\cos^2\theta_0 - 1}{\cos\theta_0 - 1} \\ &= \frac{1}{2}P(1+\cos\theta_0). \end{aligned} \tag{4.60}$$

Similarly, the degree of alignment is corrected by using the following equation:

$$\begin{aligned} A_{obs} &= \frac{1}{\Omega}\int_{\Omega} A\mathrm{P}_2(\cos\theta)d\Omega \\ &= \frac{A}{\Omega}\int_0^{\theta_0}\frac{1}{2}(3\cos^2\theta - 1)(2\pi\sin\theta d\theta) \\ &= \frac{A}{2}\frac{\cos\theta_0 - \cos^3\theta_0}{1-\cos\theta} \\ &= \frac{1}{2}A\cos\theta_0(1+\cos\theta_0). \end{aligned} \tag{4.61}$$

Eqs. (4.60) and (4.61) clearly show that the value averaged over a finite solid angle depends differently on the subtending angle between the alignment and polarization terms. In actual

experiments, the degree of alignment was deduced from the polarization change between the sections before and after the conversion. The observed alignment must therefore be corrected using Eq. (4.60). On the other hand, the observed alignment correlation term must be corrected using Eq. (4.61). The net correction factor can therefore be calculated as

$$\begin{aligned}(\alpha E)_{obs} &= \frac{(A\alpha E)_{obs})}{A'_{obs}} \\ &= \frac{A_{obs}\alpha E}{A\frac{P_{obs}}{P}} \\ &= (\alpha E)\cos\theta_0. \end{aligned} \tag{4.62}$$

By substituting θ_0 using the actual angle $(14 \pm 0.5°)$, the correction factor (C_Ω) for a finite counter solid angle is given by

$$C_\Omega = \frac{1}{\cos\theta_0} = 1.031 \pm 0.002. \tag{4.63}$$

4.3.2 Correction for beta-decay branches

The beta-decay branches of ^{12}B and ^{12}N to the excited states of ^{12}C are shown in Fig. (1.2). Since each branch has a different angular distribution, and the actual beta-ray spectrum is a mixture of these branches, the polarization and alignment terms must also be corrected for these decay branches.

The beta-ray angular distribution for each branch is given as follows:

For the ground state,

$$W_0(E,\theta) = CS_0(E)[1 \mp P(p/E)(1+\alpha_\mp E)\mathtt{P}_1(\cos\theta) + A\alpha_\mp E\mathtt{P}_2(\cos\theta)]. \tag{4.64}$$

For the first excited state E_1=4.439 MeV,

$$W_1(E,\theta) = CS_1(E)[1 \pm \frac{1}{2}P(p/E)(1+\alpha_\mp E)\mathtt{P}_1(\cos\theta) + \frac{1}{10}A\alpha_\mp E\mathtt{P}_2(\cos\theta)]. \tag{4.65}$$

For the second excited state E_2=7.654 MeV,

$$W_2(E,\theta) = CS_2(E)[1 \mp P(p/E)(1+\alpha_\mp E)\mathtt{P}_1(\cos\theta) + A\alpha_\mp E\mathtt{P}_2(\cos\theta)]. \tag{4.66}$$

Where $S_0(E)$, $S_1(E)$ and $S_2(E)$ are spectral shape functions which include their branching ratios, the angular distribution to be observed is given by the following sum:

$$\begin{aligned} W(E,\theta) \;=\; & CS(E)[1 \\ & \mp \left(1 - \frac{3}{2}\frac{S_1(E)}{S(E)}\right) P(p/E)(1+\alpha_\mp E)\mathtt{P}_1(\cos\theta) \\ & + \left(1 - \frac{9}{10}\frac{S_2(E)}{S(E)}\right) A\alpha_\mp E\mathtt{P}_2(\cos\theta)], \end{aligned} \tag{4.67}$$

where

$$S(E) \equiv S_0(E) + S_1(E) + S_2(E). \tag{4.68}$$

Therefore, the correction factor ($C^A_{\rm BR}(E)$) for the alignment term is given as

$$C^A_{\rm BR}(E) = 1 \Big/ \left(1 - \frac{9}{10}\frac{S_1(E)}{S(E)}\right). \tag{4.69}$$

Since the polarization to be observed is reduced by a factor of $\frac{3}{2}\frac{S_1(E)}{S(E)}$, the observed coefficient must be increased by this factor. Integrating over the energy region used for the analysis, the correction factor ($C^P_{\rm BR}$) through polarization is given as

$$C^P_{\rm BR} = 1 - \frac{3}{2}\frac{\int_{E_1}^{E_2} S_1(E)dE}{\int_{E_1}^{E_2} S(E)dE}. \tag{4.70}$$

The net correction factor ($C_{\rm BR}$) is therefore the product $C^A_{\rm BR} \cdot C^P_{\rm BR}$, as summarized in Table 4.3.

Table 4.3: Correction factors for the beta-decay branches.

E (MeV)	^{12}B		^{12}N	
	$C^A_{\rm BR}$	$C_{\rm BR}$	$C^A_{\rm BR}$	$C_{\rm BR}$
5	1.019	1.007	1.030	1.005
6	1.014	1.002	1.026	1.002
7	1.008	0.996	1.022	0.998
8	1.003	0.991	1.018	0.993
9	1.000	0.988	1.013	0.988
10	1.000	0.988	1.007	0.983
11	1.000	0.988	1.002	0.978
>12	1.000	0.988	1.000	0.976

$\langle C^P_{\rm BR}\rangle = \int_{4.5}^{13.5} C^P_{\rm BR}(E)dE = 0.988$ (for ^{12}B)

$\langle C^P_{\rm BR}\rangle = \int_{4.5}^{13.5} C^P_{\rm BR}(E)dE = 0.976$ (for ^{12}N)

$C_{\rm BR} = C^A_{\rm BR} \cdot \langle C^P_{\rm BR}\rangle$

4.3.3 Correction for the response function of the beta-ray detector

The observed beta-ray energy spectra are distorted from the true spectra due to the response of the counter by

$$W_{obs}(E,A) = \int_0^{E_0} W_o(E',A)R(E,E')dE', \tag{4.71}$$

where R(E,E') is the response function. The polarization term is neglected since the polarization is negligibly small. The energy spectrum (W(E,A)) is therefore given by

$$W(E,A) = S(E)(1 + A\alpha E), \tag{4.72}$$

where $S(E)$ is the spectral shape function. Using Eq. (4.72),

$$\begin{aligned} W_{obs}(E,A) &= \int_0^{E_0} S(E')(1 + A\alpha E')R(E,E')dE' \\ &= \int_0^{E_0} S(E')R(E,E')dE' + A\alpha \int_0^{E_0} S(E')E'R(E,E')dE' \\ &= S'(E)(1 + A\alpha E\frac{1}{C_{\rm RES}}), \end{aligned} \tag{4.73}$$

where the correction factor ($C_{\rm RES}$) and the new spectral shape ($S'(E)$) are given by

$$C_{\rm RES}(E) = E\frac{\int_0^{E_0} S(E')R(E,E')dE'}{\int_0^{E_0} S(E')E'R(E,E')dE'} \tag{4.74}$$

and

$$S'(E) = \int_0^{E_0} S(E')R(E,E')dE' \tag{4.75}$$

From the observed spectra from monochromatic beta rays, the response function is given as [31]

$$R(E,E') = r\sqrt{\frac{1}{2}\pi\sigma e^{-\frac{(E'-E)^2}{2\sigma}}} + (1-r)[\frac{\lambda}{1-e^{-\lambda E}}e^{\lambda(E-E')}Y(E,E')], \tag{4.76}$$

with

$$Y(E,E') = \begin{cases} 1 & E \leq E' \\ 0 & E > E' \end{cases} \tag{4.77}$$

Parameters r and λ were determined to be $r = 0.18$ and $\lambda = 0.21$ from the same observations. The σ parameter was determined to be $\sigma = 0.3$ from a fitting of the actual spectrum. By neglecting the second-order terms, the correction factor ($C_{\mathrm{RES}}(E)$) was calculated using a simplified spectral shape function, $S(E) = E^2(E_0 - E)^2$. The results are given in Table 4.4.

Table 4.4: Correction factor (C_{RES}) for the response function of the beta-ray detector.

E (MeV)	^{12}B	^{12}N
5	0.911	0.862
6	0.951	0.913
7	0.977	0.945
8	0.996	0.967
9	1.013	0.983
10	1.031	0.997
11	1.055	1.009
12	1.088	1.022
13	1.132	1.037
14	-	1.058
15	-	1.086
16	-	1.122

4.3.4 Error due to beta-ray scattering

Beta-ray scattering distorts the observed energy spectra from that of the theoretical shapes. This effect, however, can be canceled in the first order, since the ratio of the spectra with a positive alignment (A_+) to that of the negative alignment (A_-). Moreover, in the present experiment, beta-ray scattering was reduced as much as possible. The anti-coincidence counters rejected scattered beta rays from the iron-magnet yokes as well as those from the plastic chamber, which contained only the low-Z material; a very small scattering effect was therefore expected. Even though it was small, we estimated the effect on the alignment correlation term due to this beta-ray scattering.

Two effects concerning the distortion of the original beta-ray spectra by beta-ray scattering were considered: that due to the 'scattered out' beta-rays (the original shape was distorted by escaping of beta rays that left the solid angle of the detectors), and that due to 'scattered in' beta rays (those scattered by materials close to the catcher which were emitted in the central direction $\theta = 0$). In addition, 'scattered in' beta rays deposited their energy by scattering at large angles; information concerning the original energy was lost.

The 'scattered out' effect modifies the original energy spectrum ($W_o(E, A)$) according to

$$W'_o(E, A) = W_o(E, A) S_{out}(E), \tag{4.78}$$

where S_{out} is the correction factor; it depends on only the beta-ray energy as, for example,

$$S_{out}(E) = 1 - a \exp\{-bE\}. \tag{4.79}$$

Therefore, although in the ratio of $W_o(E, A_+)$ to $W_o(E, A_-)$ this effect can be canceled, the

response function ($R'(E,E')$) must include $S_{\rm out}$ instead of the original response function ($R(E,E')$), as follows:

$$R'(E,E') = R(E,E')S_{\rm out}(E). \tag{4.80}$$

On the other hand, since the 'scattered in' effect includes spectra with the other direction $\theta \neq 0$, so that this effect modifies $W_{\rm o}(E,P,A)$ according to

$$W'_{\rm o}(E,P,A) = W_{\rm o}(E,P,A)S_{\rm out}(E) + \int_0^{E_0}\int_0^{\pi} W_(E',P,A,\theta)S_{\rm in}(E,E',\theta)d\theta dE', \tag{4.81}$$

where $S_{\rm in}(E,E',\theta)$ is the observed spectrum of the 'scattered in' beta rays emitted with the energy of E' and the θ direction. By combing Eq. (4.81) with Eq. (4.72), the spectrum to be observed can be written as

$$\begin{aligned} W_{obs}(E,P,A) &= \int_0^{E_0}[W_{\rm o}(E'',P,A)S_{\rm out}(E'') \\ &\quad + \int_0^{E_0}\int_0^{\pi} W_{\rm o}(E',P,A)S_{\rm in}(E',E'',\theta)d\theta dE']R(E,E'')dE''. \end{aligned} \tag{4.82}$$

We estimated the 'scatter in' effect by a computer simulation using the Monte Carlo method. As a result, in the present experimental setup, the effect of 'scatter in' was negligible.

4.3.5 Correction for the background beta rays

In the present experiment, the beta-ray yield was sufficiently high (10^3 cps for ^{12}B, 100 cps for ^{12}N), and the electrical noise was negligible ($\leq 10^{-3}$ cps) compared to true events. The effect of background beta rays was thus very small. However, we found the mixture of $(HD)^+$ beam in the ^{3}He beam from the Van de Graaff accelerator. $(HD)^+$ beam was equivalent D^+ beam in the nuclear reaction. So that, ^{12}B were produced in the experiment

for ^{12}N. This mixture caused by the leak of ionization gas in the ion source of the Van de Graaff. It is important that the spin of these ^{12}B was not manipulated, since they had different resonance frequencies for the NMR than ^{12}N. We can thus consider the admixture of ^{12}B as the usual background. At first, I explain the effects due to the usual background noises except for the beam mixture, and then explain the effect of the beam admixture.

Background noise

Background beta rays have two origins: one is beta rays from other beta emitters and/or cosmic rays; the other is beta rays from the ^{12}B or ^{12}N stopped at locations other than the catcher. The fraction of the other beta emitters was observed using the time spectra under the same experimental conditions. Since the end-point energies of ^{12}B and ^{12}N are very large, there were no beta-ray counts from other beta emitters in the energy region used for the analysis (above 5 MeV). Also, the cosmic-ray background was negligible ($\leq 10^{-2}$ cps), since cosmic rays can be canceled by the anti-coincidence of the opposite-side counter.

The beta rays that come from outside of the catcher modify the original spectrum ($W_o(E,P,A)$) by $f(E)$, the spectrum of the outer beta rays,

$$W'_o(E,P,A) = W_o(E,P,A) + f(E). \tag{4.83}$$

Since $f(E)$ depends only on the beta-ray energy, using Eq. (2.67), Eq. (4.83) can be transformed as follows:

$$\begin{aligned} W'_o(E,P,A) &= w(E)[1 + P\frac{B_1(E)}{B_0(E)} + A\frac{B_2(E)}{B_0(E)}] + f(E) \\ &= \{w(E) + f(E)\} \\ &\quad \times[1 + \frac{w(E)}{w(E)+f(E)}P\frac{B_1(E)}{B_0(E)} + \frac{w(E)}{w(E)+f(E)}A\frac{B_2(E)}{B_0(E)}]. \end{aligned} \tag{4.84}$$

The observed alignment correlation term is therefore modified as

$$\left[\frac{B_2(E)}{B_0(E)}\right]_{\rm obs} = \frac{\frac{w(E)}{w(E)+f(E)}A\frac{B_2(E)}{B_0(E)}}{A_{\rm obs}}. \tag{4.85}$$

It is noted here that we obtained the degree of alignment from the degree of observed polarization, where the degree of polarization was extracted from the asymmetry of the integrated spectral shape. The observed polarization can therefore be described as

$$P_{\rm obs} = \frac{\int w(E)dE}{\int\{w(E)+f(E)\}dE}P. \tag{4.86}$$

Thus, the observed alignment correlation term is finally given as

$$\begin{aligned}\left[\frac{B_2(E)}{B_0(E)}\right]_{\rm obs} &= \frac{\frac{w(E)}{w(E)+f(E)}A\frac{B_2(E)}{B_0(E)}}{\frac{\int w(E)dE}{\int\{w(E)+f(E)\}dE}A} \\ &= \frac{\frac{w(E)}{w(E)+f(E)}}{\frac{\int w(E)dE}{\int\{w(E)+f(E)\}dE}}\left[\frac{B_2(E)}{B_0(E)}\right] \\ &\equiv C_{\rm bg}\left[\frac{B_2(E)}{B_0(E)}\right].\end{aligned} \tag{4.87}$$

When the background ratio is small, the correction factor ($C_{\rm bg}$) can be approximated to the first order as

$$C_{\rm bg} \simeq 1 + \frac{f(E)}{w(E)} - \frac{\int f(E)dE}{\int w(E)dE}. \tag{4.88}$$

In order to estimate the beta rays from outside of the catcher we observed the beta-ray spectra without using a catcher. The detector setup shown in Fig. (3.17) cannot completely reject the 'outer beta rays' and, thus, counted such beta rays. This result gave the upper limit of the admixture of such beta rays, since the main part of the ^{12}B or ^{12}N nuclei which was supposed to be stopped by the catcher also scattered out under this condition. From the observed energy spectra of the background beta rays, we obtained the ratio of the 'outer beta rays' to the true beta rays as

$$\frac{\int f(E)dE}{\int w(E)dE} \leq 0.04 \tag{4.89}$$

and

$$\frac{f(E)}{w(E)} \leq 0.10. \tag{4.90}$$

This value is negligible for the correction. Moreover, we observed the alignment correlation terms with the other detector configuration in order to reject such background beta rays. For the rejection of such 'outer beta rays', we added an additional counter close to the catcher. When small counters were placed just outside of the vacuum window shown in Fig. (3.1), such outside beta rays disappeared almost completely. On the contrary, however, beta-ray scattering was increased. We therefore measured the alignment-correlation coefficients under both of these conditions and compared them with each other. As a result, the two coefficients agreed within the error.

The admixture of ^{12}B in the ^{12}N

The effect of the beam admixture can be considered as the same method as the other background noise. The spectrum of ^{12}B was well known, thus, the correction was very accurate. For the correction, the amplitude of the admixture was needed. We observed this amplitude from the measurement of the ratio of the ^{16}N yield induced D^+ beam to the yield induced $(HD)^+$ beam. So that, the beam admixture was obtained about 0.1%. In the setup for the ^{12}N experiment, the ratio of the yield of ^{12}B to the yield of ^{12}N was determined about 2%. This admixture was taken into account in the correction. Table (4.5) shows the correction factor due to the beam admixture.

Table 4.5: Correction factor ($C_{\rm bg}$) for the background noise due to the beam admixture.

E (MeV)	^{12}B	^{12}N
	$C^A_{\rm bg}$	$C_{\rm bg}$
5	1.029	1.007
6	1.028	1.006
7	1.027	1.005
8	1.026	1.004
9	1.024	1.002
10	1.020	0.998
11	1.016	0.994
12	1.010	0.988
13	1.006	0.984
>14	1.000	0.978

$\langle C^P_{\rm bg}\rangle = \int_{4.5}^{13.5} C^P_{\rm bg}(E)dE = 0.978$ (for ^{12}N)

$C_{\rm bg} = C^A_{\rm bg} \cdot \langle C^P_{\rm bg}\rangle$

4.3.6 Error due to the gain instability of pulse amplification

In the present experiment the total gain of the detector systems and amplifier was stabilized by a feedback loop using a standard light pulse from a light-emitting diode (LED). By using this stabilizer system, the pulse height for a standard light pulse was kept constant. The actual gain of the detector system was monitored by the center of gravity of the spectra for actual beta rays. As shown in Fig. (3.18), the stability of the center of gravity was better than $\pm 0.5\%$, which is negligible for the coefficients.

Chapter 5

Results and Discussion

5.1 Extraction of Alignment-Correlation Coefficients

5.1.1 Alignment-correlation terms $\left[\frac{B_2(E)}{B_0(E)}\right]$

The alignment correlation terms $\left[\frac{B_2(E)}{B_0(E)}\right]$ can be extracted as a function of the beta-ray energy from the ratio $R(E)$ of the beta-ray spectrum with alignment A_+ to the spectrum with A_-, as shown in Eq. (4.15) of chapter 4. It is therefore necessary to obtain the ratio of beta-ray counts in each energy bin. In the present analysis, the spectra from individual runs were summed up after adjusting the beta-ray energy-scale by an individual energy calibration for each run.

From the analysis, the alignment correlation terms $\left[\frac{B_2(E)}{B_0(E)}\right]$ for ^{12}B and ^{12}N were obtained as functions of the beta-ray energy, as shown in Tables 5.1 and 5.2. The raw data (called 'uncorrected') in the second column of the tables are the sums of data from all of the runs. The same analysis method for both energy calibration and the determination of

the degree of alignment was used. The absolute beta-ray energy was calibrated for each run from the end points of the beta-ray spectra of ^{12}B and ^{20}F (for ^{12}B), or of ^{12}N, ^{41}Sc and ^{17}F (for ^{12}N), as described in chapter 3. The total gain of the detector system was quite stable, as shown in Fig. 3.18. The degree of alignment was determined using data from the same energy region as that used for the analysis of the alignment-correlation terms. The achievement of spin-ensemble manipulation was also stable during each run. We could therefore sum up all of the experimental alignment correlation terms, $\left[\frac{B_2(E)}{B_0(E)}\right]$. The summed data were then corrected in each energy bin by using the correction factors given in Table 4.2. The 'corrected' data are listed in the third column of Tables 5.1 and 5.2 and in Fig. (5.1).

5.1.2 Definition of the alignment-correlation coefficients ($\alpha_{\pm}$)

As was theoretically shown by Morita *et al.*, the observed $\alpha_{\mp}$ coefficients were almost independent of the beta-ray energy. However, as was also theoretically shown by Koshigiri *et al.*, there was a slight energy dependence in the experimental coefficients, as shown in Fig. (5.2). The experimental results must therefore be compared with the theoretical prediction by using the same averaging procedure in the same energy range.

In the previous analysis, α_- and α_+ were individually determined from the ratio of their spectra with the different energy region; the old coefficients were extracted from the total gradient of $\left[\frac{B_2(E)}{B_0(E)}\right]$ over the energy region $E = E_\ell \sim E_h$, as follows:

$$\alpha \equiv \frac{\left[\frac{B_2(E_h)}{B_0(E_h)}\right] - \left[\frac{B_2(E_\ell)}{B_0(E_\ell)}\right]}{E_h - E_\ell}. \tag{5.1}$$

Although their definition was matched by a the theoretical calculation for a comparison,

this method was not sufficiently accurate to consider the energy-dependent alignment-correlation terms.

In the present analysis, the alignment correlation coefficients ($\alpha_{\pm}$) are defined as being the average of the $\left[\frac{B_2(E)}{B_0(E)}\right]$ ratio over the range of beta-ray energy under consideration,

$$\alpha_{\mp} \equiv \left\langle \frac{\left[\frac{B_2(E)}{B_0(E)}\right]_{\beta\mp\text{decay}}}{E} \right\rangle. \tag{5.2}$$

This definition is equivalent to the least-square fitting of a straight line ($\alpha_{\mp}E$) drawing from the origin of the coordinate to the experiment $\left[\frac{B_2(E)}{B_0(E)}\right]$. We chose the energy region from 4.5 MeV to 13.5 MeV for both ^{12}B and ^{12}N, so that the amount of any correction factor would be less than 15%, which is five-times larger than the present statistical errors. Because the present uncertainty of the correction factors may reach 20% (relative), we used the same energy region for both ^{12}B and ^{12}N for simplicity in any further analysis. The $\alpha_{\mp}$ values were thus determined to be as follows:

$$\alpha_{-} = -0.0174 \pm 0.0056 \quad (\%/\text{MeV}) \tag{5.3}$$

and

$$\alpha_{+} = -0.2774 \pm 0.0086 \quad (\%/\text{MeV}). \tag{5.4}$$

5.1.3 Sum and difference of $\alpha_{\pm}$

In order to discuss concerning on the time component and second class current, it is necessary to obtain the sum and difference of the coefficients. The sum and difference of the coefficients were extracted from the average of $\left[\frac{B_2(E)}{B_0(E)} \Big/ E\right]_{^{12}\text{B}}$ and $\left[\frac{B_2(E)}{B_0(E)} \Big/ E\right]_{^{12}\text{N}}$ in the energy region. As a result, the sum and difference were determined in the energy region from 4.5 to 13.5 MeV as

$$(\alpha_- + \alpha_+) = -0.2948 \pm 0.0107 \text{ (\%/MeV)}$$

and

$$(\alpha_- - \alpha_+) = 0.2600 \pm 0.0107 \text{ (\%/MeV)}.$$

Before comparing the present data with the theoretical predictions, it is noted that the present $\alpha_\pm$ coefficients were derived from the absolute inclination of the alignment correlation term $\left[\frac{B_2(E)}{B_0(E)}\right]$, *i.e.* the average $\left\langle \frac{B_2(E)}{B_0(E)} \Big/ E \right\rangle$. So, the predicted values should be also derived from the same averaging method. This is because the theoretical $\left[\frac{B_2(E)}{B_0(E)}\right]$ has also a second-power term of beta-ray energy with a coefficient of about -0.0025 %/MeV^2 for both ^{12}B and ^{12}N besides the linear term of beta-ray energy. Since the second power term is almost the same for ^{12}B and ^{12}N, this term is canceled in the difference of α_- and α_+. However, it is doubled in the sum $(\alpha_- + \alpha_+)$. Therefore, in this discussion, the sum of the coefficients was directly compared with the theoretical calculations instead of reducing y value from the experimental sum. The theoretical sum in Fig. (5.6) is calculated from the theoretical $\left[\frac{B_2(E)}{B_0(E)}\right]$.

Table 5.1: Alignment correlation term of ^{12}B as a function of the beta-ray energy

E (MeV)	$\frac{B_2(E)}{B_0(E)}$ (%) uncorrected	$\frac{B_2(E)}{B_0(E)}$ (%) corrected
5	-0.0776 ± 0.1319	-0.0735 ± 0.1284
6	$+0.0405 \pm 0.1219$	$+0.0399 \pm 0.1235$
7	-0.0075 ± 0.1162	-0.0076 ± 0.1206
8	-0.1557 ± 0.1158	-0.1589 ± 0.1218
9	-0.1155 ± 0.1210	-0.1195 ± 0.1287
10	-0.2360 ± 0.1343	-0.2487 ± 0.1446
11	-0.3511 ± 0.1620	-0.3786 ± 0.1772
12	-0.1963 ± 0.2201	-0.2183 ± 0.2465
13	-0.4657 ± 0.3617	-0.5387 ± 0.4195
	Coefficient α_- (%/MeV)	-0.0174 ± 0.0056

The coefficient α_- is defined as the mean of $\frac{\left[\frac{B_2(E)}{B_0(E)}\right]_{^{12}\mathrm{B}}}{E}$ in the 4.5 $\sim$ 13.5 MeV energy region.

Table 5.2: Alignment correlation term of ^{12}N as a function of the beta-ray energy

E (MeV)	$\frac{B_2(E)}{B_0(E)}$ (%) uncorrected	$\frac{B_2(E)}{B_0(E)}$ (%) corrected
5	-1.4321 ± 0.2287	-1.2539 ± 0.2338
6	-1.6315 ± 0.2122	-1.5065 ± 0.2192
7	-1.8870 ± 0.2002	-1.7949 ± 0.2101
8	-2.0524 ± 0.1943	-1.9873 ± 0.2062
9	-2.4928 ± 0.1933	-2.4346 ± 0.2107
10	-2.9239 ± 0.1992	-2.8685 ± 0.2222
11	-3.2284 ± 0.2128	-3.1780 ± 0.2389
12	-3.4991 ± 0.2364	-3.4612 ± 0.2641
13	-3.9315 ± 0.2771	-3.9324 ± 0.3071
14	-4.6398 ± 0.3450	$-4,7056 \pm 0.3786$
15	-5.9478 ± 0.4712	-6.1929 ± 0.5119
16	-3.5464 ± 0.7341	-3.8150 ± 0.7438
	Coefficient α_+ (%/MeV)	-0.2774 ± 0.0086

The coefficient α_+ is defined as the mean of $\frac{\left[\frac{B_2(E)}{B_0(E)}\right]_{^{12}\mathrm{N}}}{E}$ in the $4.5 \sim 13.5$ MeV energy region.

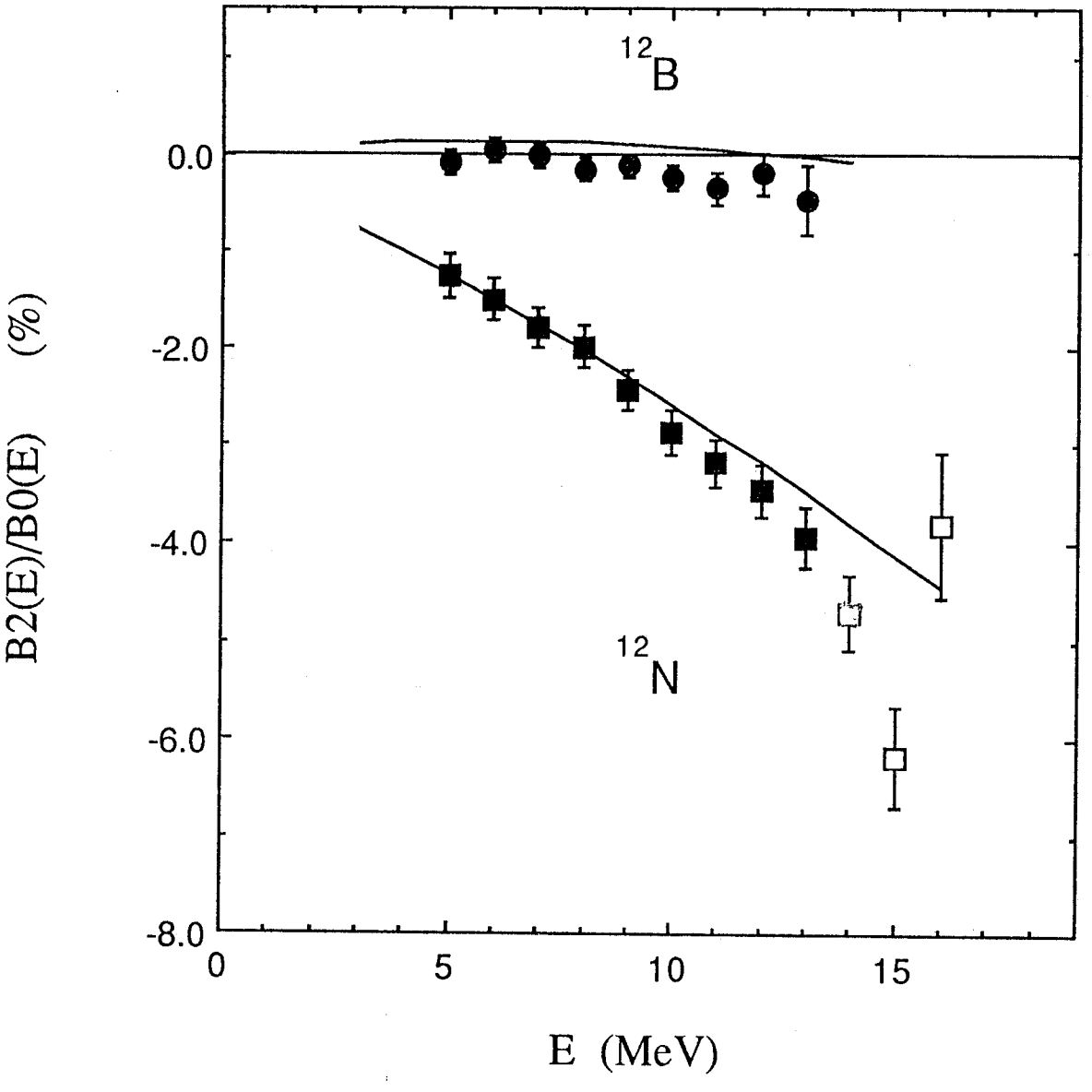

Figure 5.1: Alignment correlation terms $[\frac{B_2(E)}{B_0(E)}]$ for ^{12}B and ^{12}N. The closed marks are used in the present analysis. The solid lines are the theoretical predictions by Koshigiri, *et al.* [27, 33].

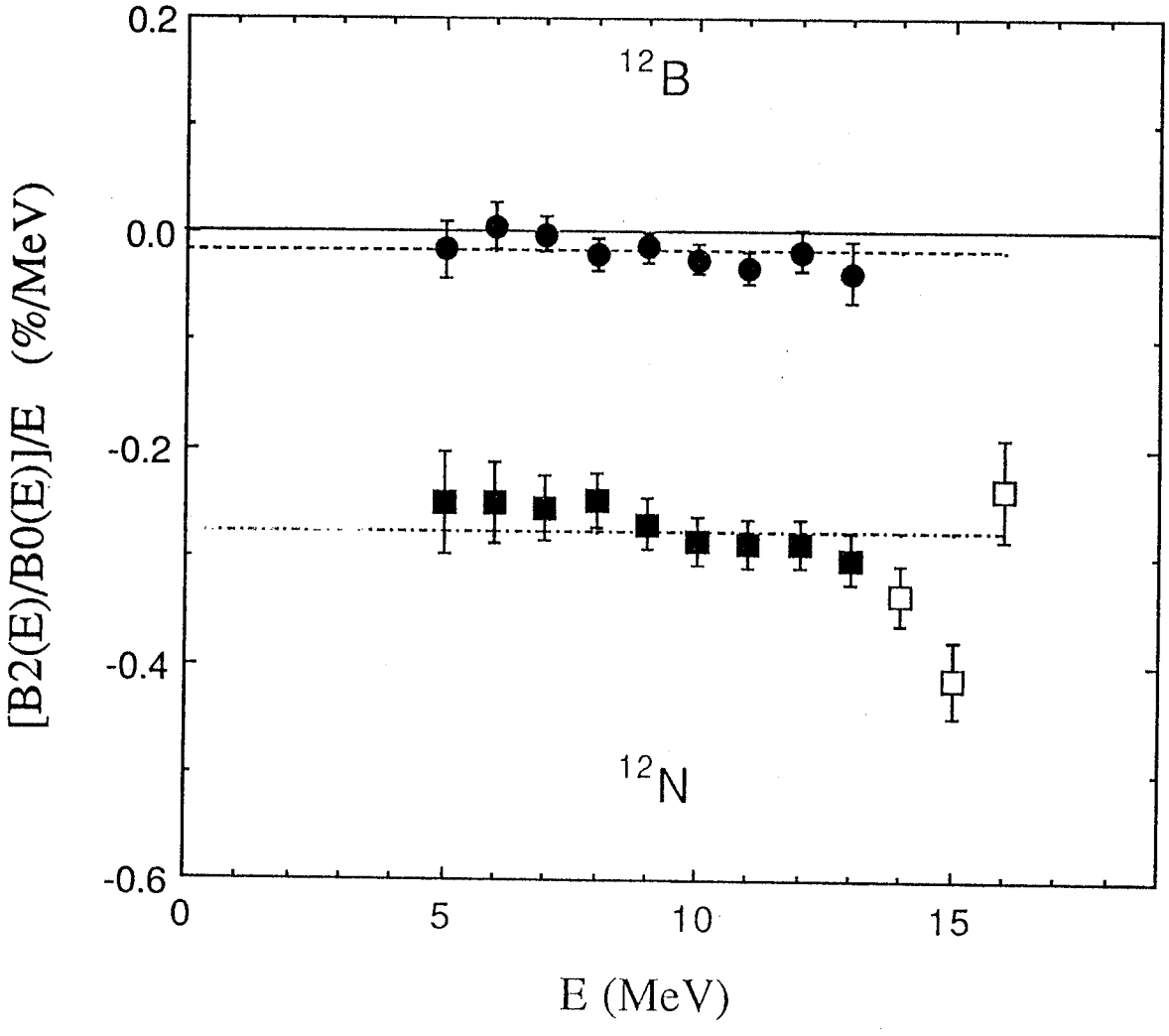

Figure 5.2: Alignment correlation coefficients ($\frac{\left[\frac{B_2(E)}{B_0(E)}\right]}{E}$) as a function of the beta-ray energy. The closed marks are used in the present analysis. The dotted lines are the averaged coefficients $\alpha_{\mp}$.

Table 5.3: Difference and sum of the alignment correlation terms of ^{12}B and ^{12}N.

E (MeV)	$\left[\frac{B_2}{B_0}\right]_{^{12}\mathrm{B}} - \left[\frac{B_2}{B_0}\right]_{^{12}\mathrm{N}}$ (%)	$\left[\frac{B_2}{B_0}\right]_{^{12}\mathrm{B}} + \left[\frac{B_2}{B_0}\right]_{^{12}\mathrm{N}}$ (%)
5	$+1.2912 \pm 0.2504$	-1.3491 ± 0.2504
6	$+1.9811 \pm 0.2344$	-1.7746 ± 0.2344
7	$+2.0596 \pm 0.2255$	-2.1962 ± 0.2255
8	$+1.9502 \pm 0.2236$	-2.2994 ± 0.2236
9	$+2.3893 \pm 0.2307$	-2.7487 ± 0.2307
10	$+2.9068 \pm 0.2499$	-3.3138 ± 0.2499
11	$+2.6965 \pm 0.2891$	-3.6033 ± 0.2891
12	$+3.7998 \pm 0.3735$	-4.2211 ± 0.3735
13	$+3.9447 \pm 0.5949$	-5.0389 ± 0.6289

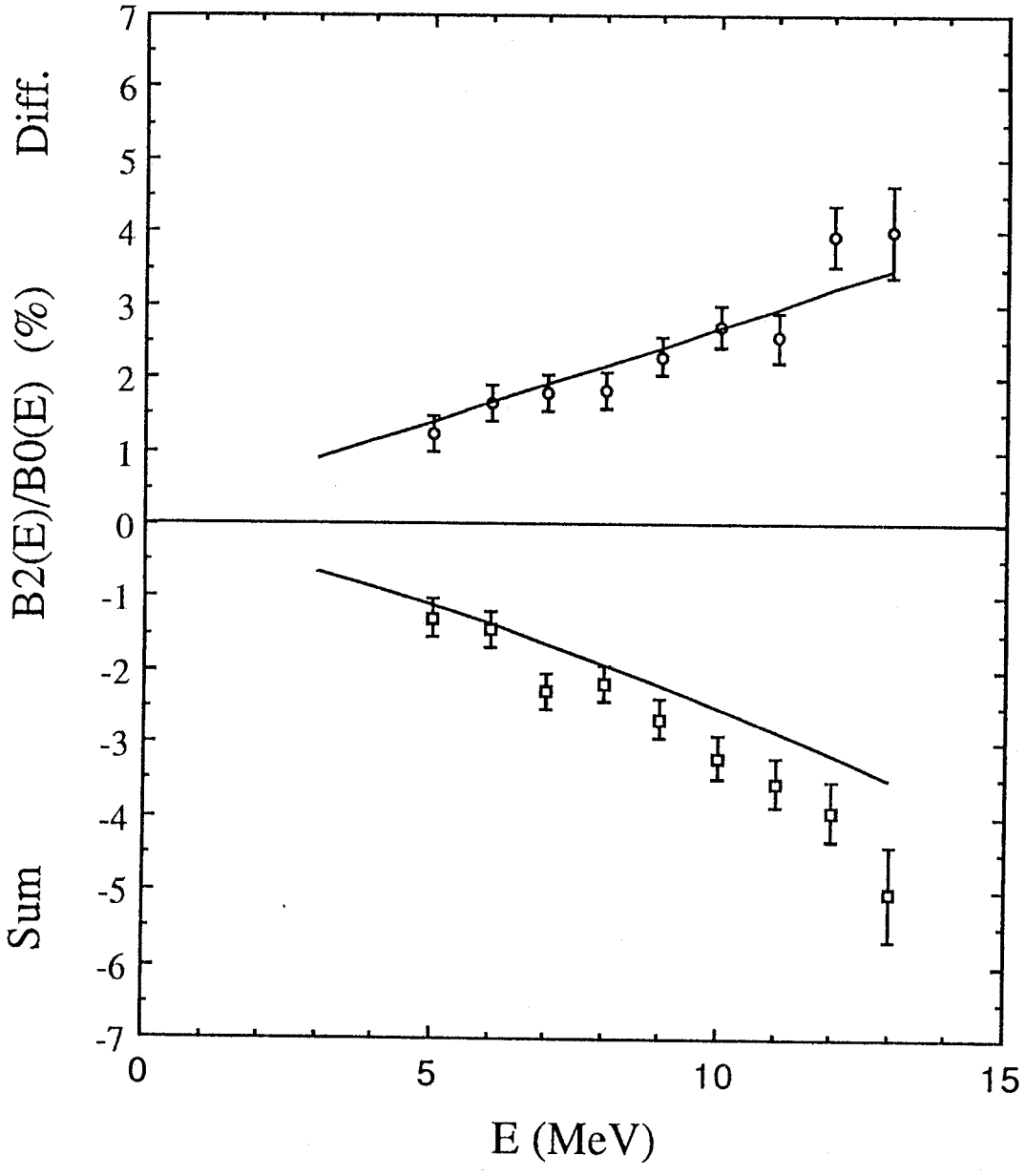

Figure 5.3: Sum and difference of the alignment correlation terms $\left[\frac{B_2(E)}{B_0(E)}\right]$ as a function of the beta-ray energy. The solid lines are the theoretical predictions by Koshigiri, *et al.* [27, 33].

5.2 Time Component of the Axial Vector Current

5.2.1 Determination of the time component

The sums of the alignment correlation terms are shown as functions of the beta-ray energy in Table 5.3. In Fig. (5.4), the present results are given with improved precision. Under the rough approximation, the sum of the alignment correlation terms comprise only the nuclear parameter (y), which is the ratio of the axial charge, *i.e.*, the main term of the time component of the axial vector current divided by the Gamow-Teller matrix element, as given in Eq.(2.62):

$$\begin{aligned}(\alpha_- + \alpha_+) &\equiv \left\langle \frac{\left[\frac{B_2(E)}{B_0(E)}\right]_{^{12}\mathrm{B}} + \left[\frac{B_2(E)}{B_0(E)}\right]_{^{12}\mathrm{N}}}{E} \right\rangle \\ &= -\frac{4}{3}y. \end{aligned} \tag{5.5}$$

Therefore, the determination of $(\alpha_- + \alpha_+)$ is equal to the determination of the time component.

However, the actual sum of alignment-correlation terms includes a second-power term of beta-ray energy. In order to extract the meson-exchange effect with accuracy, the experimental value must be directly compared with the theoretical calculation as a function of beta-ray energy. In the present analysis, the meson-exchange effect was extracted as a discrepancy (δ) from the theoretical IA calculation as follows:

$$\left[\frac{B_2(E)}{B_0(E)}\right]_{\mathrm{exp}} = (1+\delta)\left[\frac{B_2(E)}{B_0(E)}\right]_{\mathrm{IA}}. \tag{5.6}$$

δ was determined by using the least-square fitting over the 4.5 $\sim$ 13.5 MeV energy region.

5.2.2 Enhancement of the time component due to mesonic effects

Fig. (5.5) shows both the present experimental value and the theoretical predictions under the impulse approximation with the Cohen-Kurath shell model by Koshigiri, *et al.* [10]. The solid line is the IA values and the dotted line is the values fitted by the least-square method. The discrepancy δ was determined as

$$\delta = 0.36 \pm 0.05. \tag{5.7}$$

This large enhancement ($36 \pm 5\%$) clearly shows a effect of the meson-exchange currents in the time component. The nuclear parameter y in the IA value is calculated as

$$y = 3.72. \tag{5.8}$$

From Eq. (5.7), the experimental $y_{\rm exp}$ is obtained as

$$y_{\rm exp} = 5.06 \pm 0.19. \tag{5.9}$$

However, the nuclear parameter y has the theoretical model dependence, since y is divided by the Gamow-Teller matrix element. The Gamow-Teller matrix element calculated from the Cohen-Kurath shell model is inconsistent with the experimental value.

In the recent studies, Koshigiri, *et al.* predicted the new theoretical calculation, which included the meson-exchange currents and the first- and higher-order core polarization, by using the Paris potential [27, 33]. Fig. (5.6) shows the present experimental value and the most advanced theoretical predictions. 'IA ($0\hbar\omega$)' means the value calculated by using the Paris potential in the $0\hbar\omega$ shell model. 'IA ($0\hbar\omega$)' means the full $0 + 2\hbar\omega$ shell model.

As shown in Fig. (5.6) clearly, the present value is larger by about 56% than the 'IA $(0\hbar\omega)$' value. This large enhancement clearly shows a effect of the meson-exchange currents in the time component. According to Koshigiri *et al.*, the meson effect on the $(\alpha_- + \alpha_+)$ is as large as 36%. However, the core polarization effect, which includes the first and higher order core polarization, reduced the enhancement by about -12%. As a result, the most advanced theory predicts a total enhancement of about 24%, as graphically shown as 'IA+MEC $(0 + 2\hbar\omega)$' value in Fig. (5.6).

The evident discrepancy (about 25%) between the experiment and theoretical value still exists.

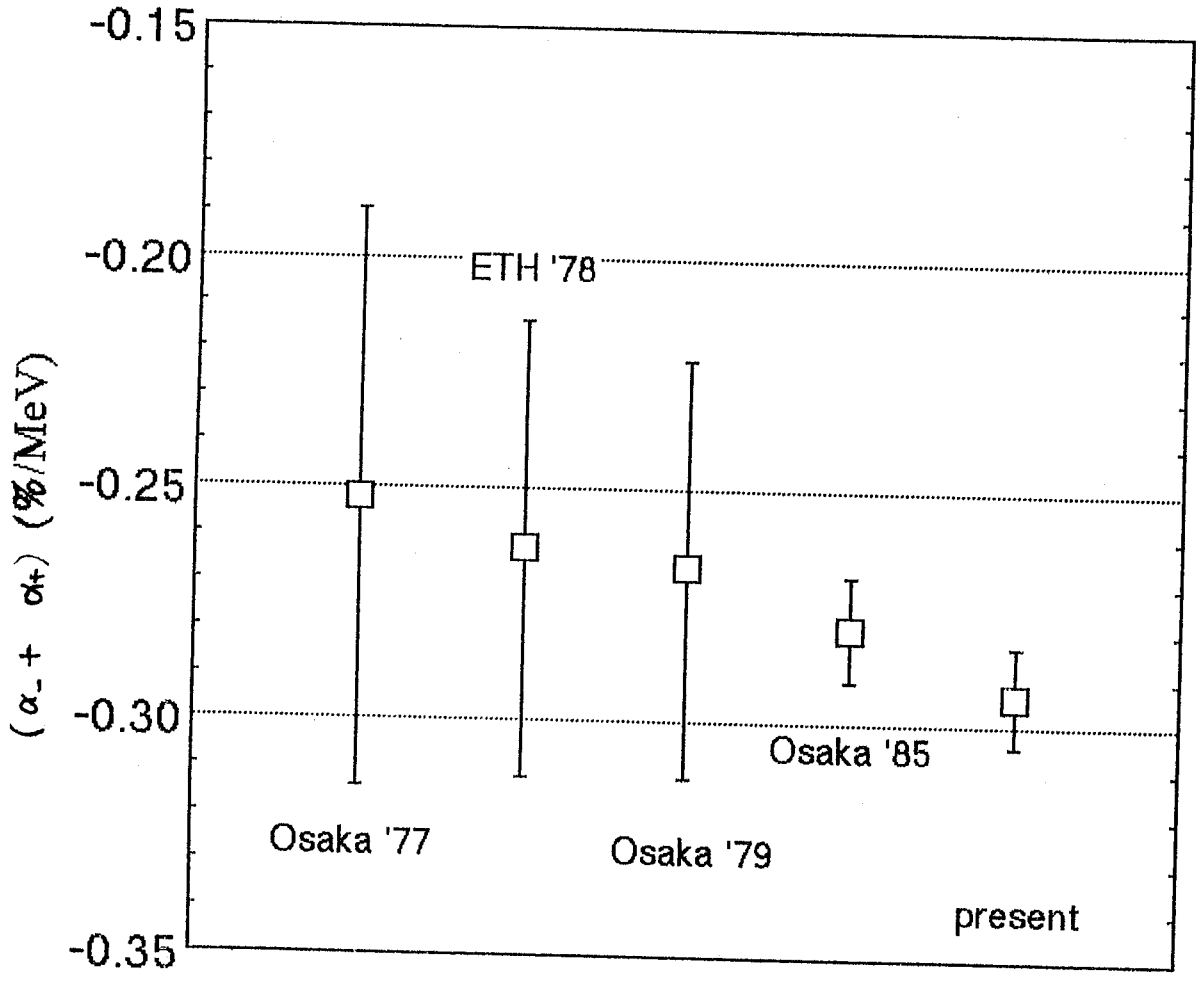

Figure 5.4: Comparison of the sum of the alignment coefficients $(\alpha_- + \alpha_+)$ from the previous and present results.

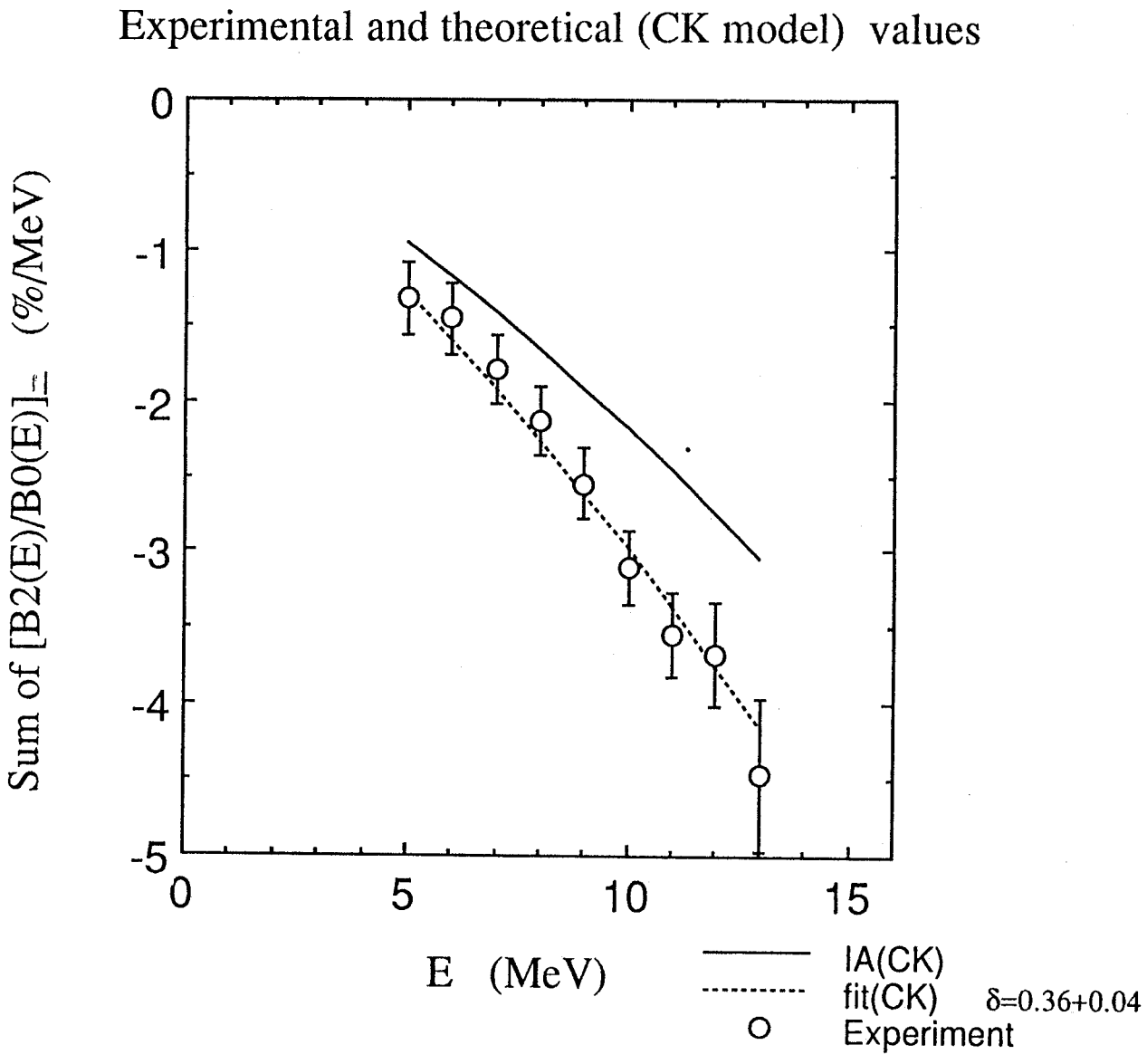

Figure 5.5: Comparison of the present result and the theoretical value of the sum of alignment-correlation terms. The solid line is the theoretical values calculated under the impulse approximation with the Cohen-Kurath shell model [10]. The dotted line is the fitted values by using the least-square method.

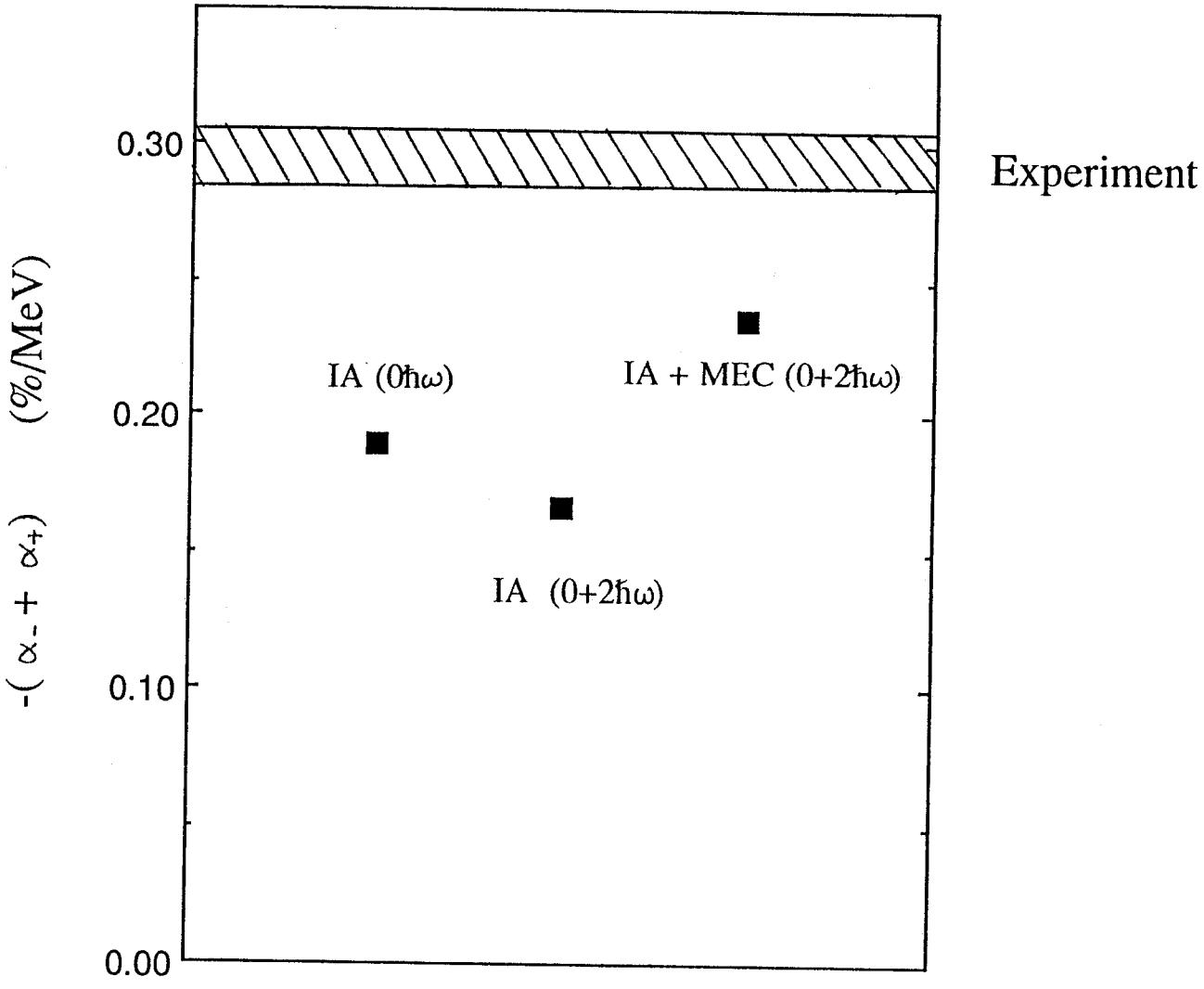

Figure 5.6: Comparison of the present value and the theoretical value of the sum of coefficients $(\alpha_- + \alpha_+)$. The theoretical values were calculated from the recent studies [27, 33].

5.3 Induced Tensor and Weak Magnetism Term

The difference of the alignment correlation term comprises a second-class current term and a weak magnetism term like as Eq. (2.63).

$$\begin{aligned}(\alpha_- - \alpha_+) &\equiv \left\langle \frac{\left[\frac{B_2}{B_0}\right]_{^{12}\mathrm{B}} - \left[\frac{B_2}{B_0}\right]_{^{12}\mathrm{N}}}{E} \right\rangle \\ &= \frac{4}{3}(a - \frac{f_\mathrm{T}}{g_\mathrm{A}}).\end{aligned} \tag{5.10}$$

The difference was determined as follows:

$$(\alpha_- - \alpha_+) = 0.2600 \pm 0.0107. \tag{5.11}$$

A comparison of $(\alpha_- - \alpha_+)$ in the previous and the present results is shown in Fig. (5.7).

5.3.1 Test of G-parity conservation

If the second-class current exists, conservation of the G-parity in weak nucleon currents is violated. From Eq. (5.10), the second-class current term can be described as

$$\frac{f_\mathrm{T}}{g_\mathrm{A}} = -\frac{3}{4}(\alpha_- - \alpha_+) + a. \tag{5.12}$$

Here, g_A is the effective coupling constant reformed from the free nucleon coupling constant, f_A:

$$g_\mathrm{A} = f_\mathrm{A} + E_0 f_\mathrm{T}. \tag{5.13}$$

The $E_0 f_\mathrm{T}$ term can be neglected, since it is less than 1% of f_A; g_A can thus be approximated to be equal to f_A. Therefore, Eq. (5.12) can be transformed as

$$\frac{f_\mathrm{T}}{f_\mathrm{A}} \sim -\frac{3}{4}(\alpha_- - \alpha_+) + a. \tag{5.14}$$

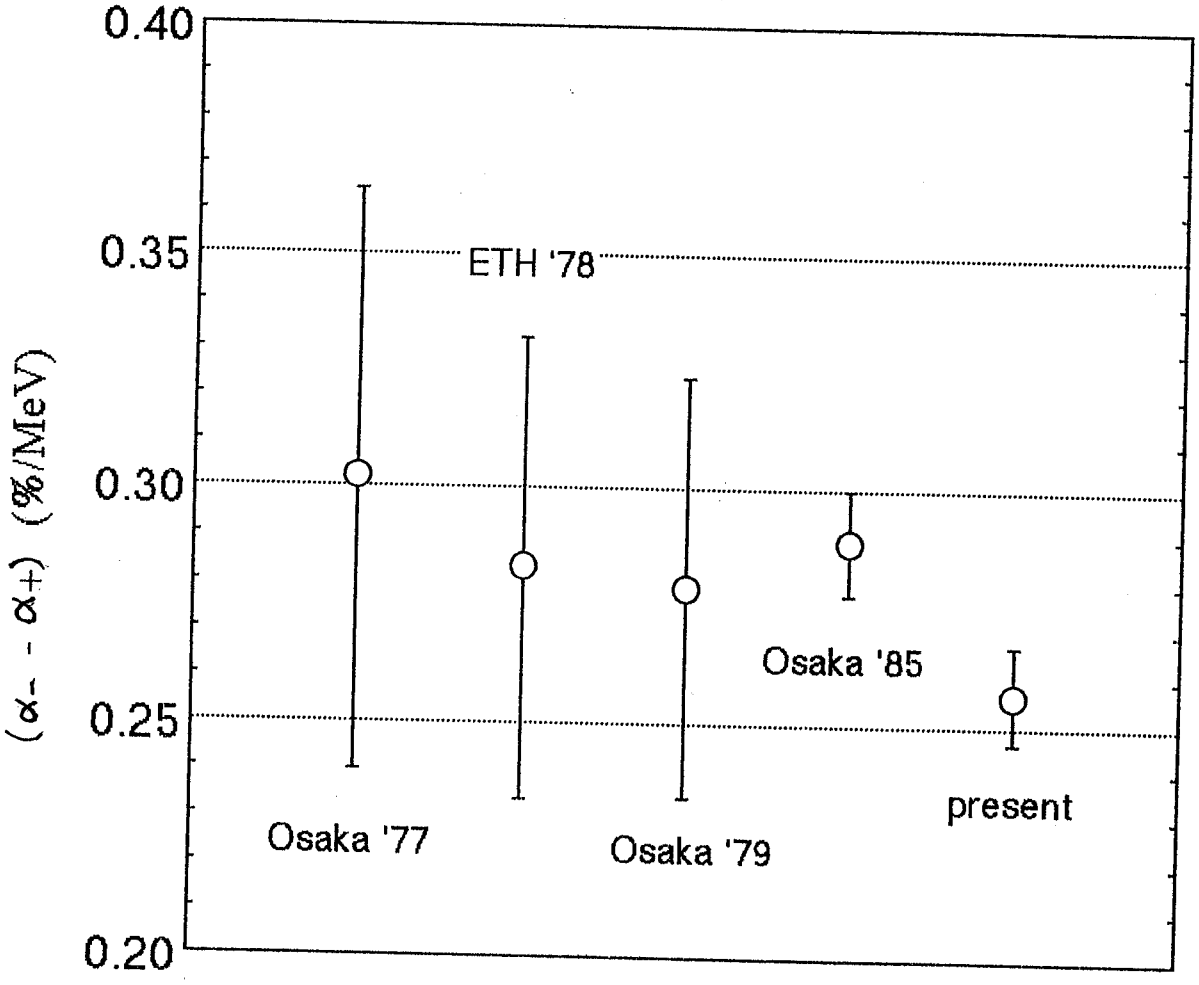

Figure 5.7: Comparison of the difference in the alignment coefficients $(\alpha_- - \alpha_+)$ in both the previous and present results.

In order to determine the second-class current term from only the experimental data, the weak magnetism term (a) is required; a was measured by observation of the beta-ray energy spectral shape correction factors ($a_{\mp}$) in the decay of ^{12}B and ^{12}N

$$a = \frac{3}{16}(a_- - a_+). \tag{5.15}$$

The Columbia group and Heidelberg group observed experimental data for $a_{\pm}$, independently. The weighted mean of their values was adopted as being the experimental value:

$$\begin{aligned}
(a_- - a_+) &= 0.86 \pm 0.24 \quad (\%/\mathrm{MeV}): \quad \text{Columbia group} \\
&= 1.09 \pm 0.09 \quad (\%/\mathrm{MeV}): \quad \text{Heidelberg group} \\
\overline{(a_- - a_+)} &= 1.062 \pm 0.084 \quad (\%/\mathrm{MeV}).
\end{aligned} \tag{5.16}$$

From Eq. (5.15)

$$a = 0.199 \pm 0.016 \quad (\%/\mathrm{MeV}). \tag{5.17}$$

From the present value

$$-\frac{3}{4}(\alpha_- - \alpha_+) = -0.1948 \pm 0.0073. \tag{5.18}$$

f_{T} was obtained as

$$\begin{aligned}
\frac{f_{\mathrm{T}}}{f_{\mathrm{A}}} &= 0.004 \pm 0.018 \quad (\%/\mathrm{MeV}) \\
&= 0.02 \pm 0.09 \quad (\times 10^{-4}/m_e c^2)
\end{aligned} \tag{5.19}$$

and

$$f_{\mathrm{T}} = (0.08 \pm 0.33) \quad (f_{\mathrm{A}}/2M). \tag{5.20}$$

f_A was determined by observing the neutron decay. In order to use this value, f_T is given as,

$$f_A = -1.254 \pm 0.007 \tag{5.21}$$

and

$$f_T = -0.10 \pm 0.42 \quad (1/2M). \tag{5.22}$$

From the CVC theory, the weak magnetism term f_W^{CVC} is given as,

$$f_W^{CVC} = -3.706 \quad (1/2M). \tag{5.23}$$

The limitation of the second-class current term was obtained as the following ratio of f_T to f_W^{CVC}:

$$\frac{f_T}{f_W^{CVC}} = 0.03 \pm 0.11. \tag{5.24}$$

On the other hand, when the weak magnetism term $a = 0.193$, which is theoretical calculation, was used, the second-class current term was obtained as

$$\frac{f_T}{f_W^{CVC}} = 0.01 \pm 0.05. \tag{5.25}$$

However, this theoretical calculation does not include the meson-exchange effect.

In conclusion, the G-parity violating current is less than 11% of the weak magnetism term with only experimental values, or less than 5% with the CVC theory. This is consistent with the non-existence of the second-class current. The present result and the previous results are given in Fig. (5.8).

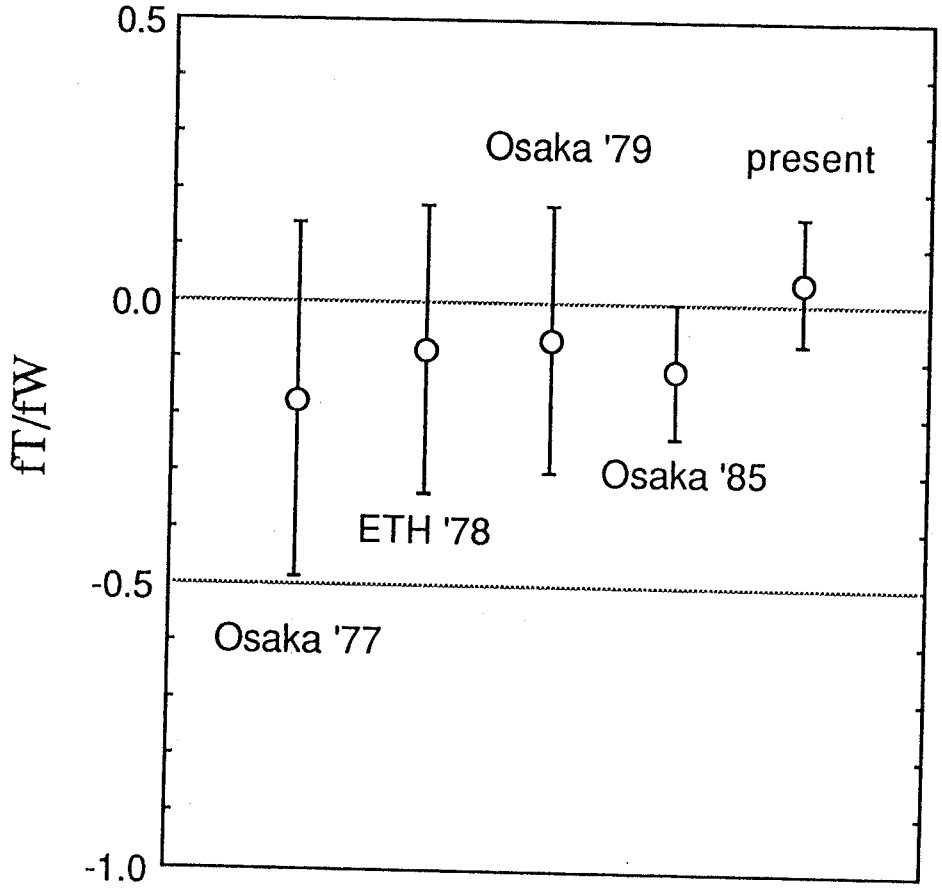

Figure 5.8: Ratio of the G-parity violating second class current to the weak magnetism current.

5.3.2 Test of CVC theory

If the second-class current does not exist (as discussed in section 5.3.1), the weak magnetism term can be obtained from the present experimental result. Eq. (5.12) can be transformed under the condition that $f_{\mathrm{T}} = 0$, as follows:

$$a = \frac{3}{4}(\alpha_- - \alpha_+), \tag{5.26}$$

where a is obtained as

$$a = 0.1950 \pm 0.0080 \quad (\%/\mathrm{MeV}). \tag{5.27}$$

There are some methods for testing the CVC theory in an A=12 system, as follows: measurement of the shape correction factors of the beta-ray energy spectra in ^{12}B and ^{12}N; measurement of the γ-ray energy width of the M1 transition from the isobaric analogue state of ^{12}C; and the present work.

The weak magnetism term 'a' obtained from each method was related to each other, as follows:

$$a = \frac{3}{16}(\mathrm{a}_- - \mathrm{a}_+) \tag{5.28}$$

$$= \sqrt{\frac{3}{4}\frac{\Gamma_\gamma}{\alpha E_\gamma^3}\frac{ft}{ft_{(0^+\to 0^+)}}} \tag{5.29}$$

$$= \frac{3}{4}(\alpha_- - \alpha_+). \tag{5.30}$$

In Eq. (5.28), $\mathrm{a}_\mp$ are the spectral shape-correction factors in $\beta^\mp$ decays. In Eq. (5.29), ft is the ft value for the beta decay of ^{12}B and ^{12}N; $ft_{(0^+\to 0^+)}$ is the reduced transition probability ft value of pure Fermi transitions ($0^+ \to 0^+$); α is the fine-structure constant; E_γ is the gamma-ray energy; and Γ_γ is the energy width.

The present result and these other tests' results are given in Fig. (5.9). The dotted-line indicates the theoretical values by Koshigiri, *et al.* [10]. The present result shows good agreement with this calculation.

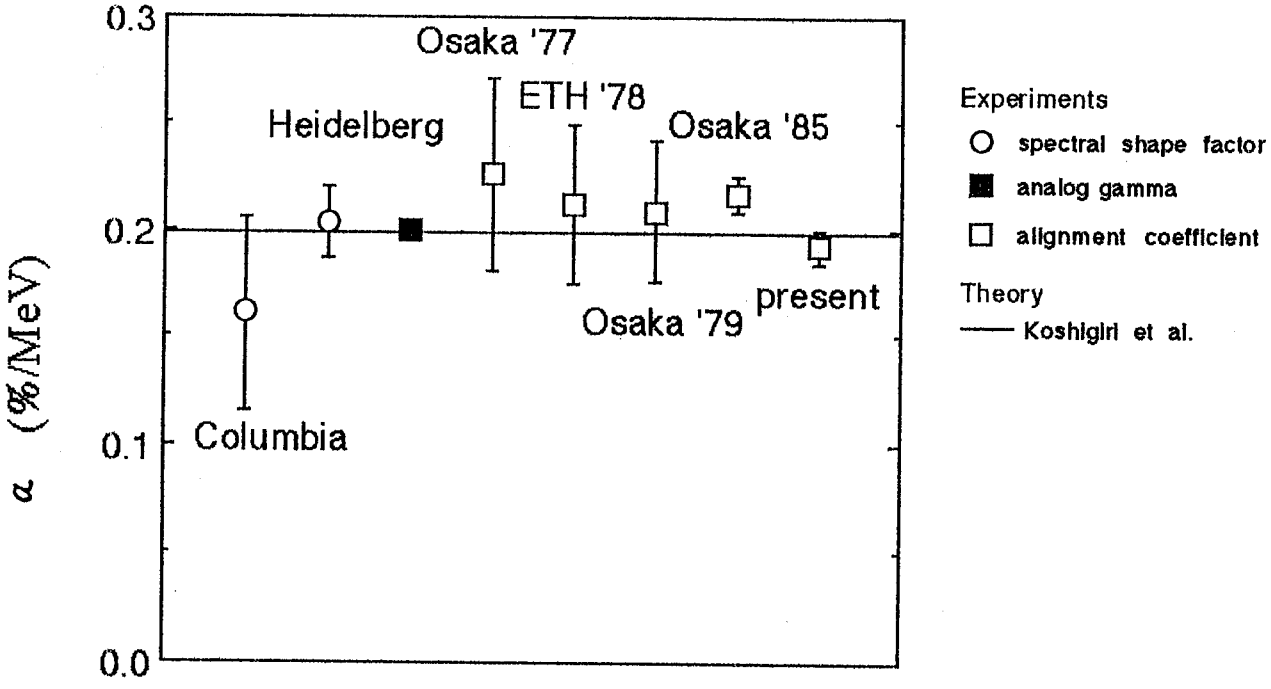

Figure 5.9: Weak magnetism term (a) for a comparison of the present results and the previous results.

Chapter 6

Conclusion

Alignment correlation coefficients $\alpha_{\mp}$ were determined to be $\alpha_{-} = -0.0174 \pm 0.0056$ and $\alpha_{+} = -0.2774 \pm 0.0086$ for ^{12}B and^{12}N, respectively. In the present experiment, the reliability of the degree of alignments and the achievement of spin manipulation were improved by the new knowledge on the hyperfine interaction of ^{12}B and ^{12}N in Mg. The accuracy of the energy calibration was also improved by measuring beta-ray energy spectra of several beta emitters.

In order to determine the meson-exchange enhancement of the time component of the axial vector currents, the sum of coefficients, which was proportional to the time component, was compared with the theoretical calculations. The present experimental value $(\alpha_{-} + \alpha_{+}) = -(0.2948 \pm 0.0107)$ showed significant enhancement due to meson-exchange current by about $36 \pm 5\%$ than the theoretical value under the impulse approximation with the Cohen-Kurath shell model. Of cause, under this model the tensor force is too strong and the calculated Gamow-Teller matrix element is inconsistent with the experimental value. However, this discrepancy cannot explain without the evidence of the meson-exchange

currents.

In the recent theoretical studies by Koshigiri *et al.*, the meson-exchange current enhances the time component by 36% and the core polarization reduces by 12%. They calculated the theoretical values by using the Paris potential, which was the full $0 + 2\hbar\omega$ shell model included the higher-order core polarization and had good consistency between the theoretical and experimental Gamow-Teller matrix element. This theoretical value is larger by 9% than the impulse approximation value under the Cohen-Kurath shell model. Therefore, the present value is still larger than the most advanced theoretical value by about 25%. It can be concluded from these facts that the present experimental results of the alignment-correlation coefficients definitely indicate the strong meson-exchange effect in the time component of the weak nuclear axial vector currents.

The theoretical studies are still in progress for more accurate value. The value, which included the meson-exchange effect in the Gamow-Teller matrix element, may reduce the gap between theoretical value and experimental value by about 5%. For more evaluate discussions on the meson-exchange current, more accurate theoretical calculations of the core polarization are required.

On the other hand, in the present experiment the limitation of the G-parity conservation law was determined from the difference of the coefficients $\alpha_{\mp}$. The difference of coefficients comprised of the weak magnetism term and the second class term. In the present analysis the weak magnetism term determined experimentally was used so that the limit $f_{\mathrm{T}}/f_{\mathrm{W}} = 0.04 \pm 0.11$ was obtained. This result is the most reliable limit of the G-parity conservation law.

References

[1] S. Weinberg, Phys. Rev. Lett. **19**(1967)1264

[2] UA1Collaboration, Phys. Lett. **122B**(1983)103

[3] N. Cabibbo, Phys. Rev. Lett. **10**(1963)531

[4] H. Yukawa, Proc. Phys. Math. Soc. **17**(1935)48

[5] F. Villars, Helv. Phys. Acta **20**(1948)476

[6] R. G. Sachs, Phys. Rev. **74**(1948)433

[7] M. Chemtob and M. Rho, Nucl. Phys. **A163**(1971)1

[8] K. Kubodera, J. Delorme and M. Rho, Phys. Rev. Lett. **40**(1978)755

[9] P. Guichon, H. Giffon and C. Samour, Phys. Lett. 74B(1978)15

[10] K. Koshigiri, H. Ohtsubo and M. Morita, Prog. Theor. Phys. 66(1981)358

[11] S. Nozawa, K. Kubodera and H. Ohtsubo, Nucl. Phys. **A453**(1986)645

[12] L. Palffy, J. P. Deutsh, L. Grenacs, J. Lehman and M. Steels,
Phys. Rev. Lett. **34**(1975)212

[13] C. A. Gagliardi, G. T. Garvey and J. R. Wrobel, Phys. Rev. Lett. **48**(1982)914

[14] T. Minamisono, K. Takeyama, T. Ishigai, H. Takeshima, Y. Nojiri and K. Asahi, Phys. Lett. **130B**(1983)1

[15] H. Mach, E. K. Warburton, R. L. Gill, R. F. Casten, J. A. Becker, B. A. Brown and J. A. Winger, Phys. Rev. **C41**(1990)226

[16] M. Morita, Phys. Rev. **113**(1959)1584

[17] Y. K. Lee, L. M. Mo and C. S. Wu, Phys. Rev. Lett. **10**(1963)253

[18] C. S. Wu, Y. K. Lee, and L. W. Mo, Phys. Rev. Lett. **39**(1977)72

[19] W. Kaina, v. Soergel, H. Thies and W. Trost, Phys. Lett. **70B**(1977)411

[20] S. Weinberg, Phys. Rev. **112**(1958)1375

[21] K. Sugimoto, I. Tanihata and J. Goring, Phys. Rev. Lett. **44**(1978)801

[22] Y. Masuda, T. Minamisono, Y. Nojiri and K. Sugimoto, Phys. Rev. Lett. **43**(1979)1083

[23] P. Lebrun, Ph. Deschepper, L. Grenacs, J. Lehmann, C. Leroy, L. Palffy, A. Possoz, and A. Maio, Phys. Rev. Lett. **40**(1978)302

[24] T. Minamisono, K. Matsuta, Y. Nojiri and K. Takeyama, J. Phys. Soc. Jpn. Supple.**55**(1986)382

[25] K. Koshigiri, M. Nishimura, H. Ohtsubo and M. Morita, Nucl. Phys. **A319**(1979)301

[26] A. Kitagawa, K. Matsuta, Y. Nojiri and T. Minamisono, Hyp. Int. **60**(1990)869

[27] K. Koshigiri, K. Kubodera, H. Ohtsubo and M. Morita, Proc. Int. Conf. on Nuclear Weak Process and Nuclear Structure, Osaka, 1989, p.52

[28] M. Morita, A. Shimizu, H. Ohtsubo, and K. Kubodera, Suppl. Prog. Theor. Phys. **60**(1976)1

[29] K. Koshigiri, Ph. D. Thesis

[30] T. P. Das, E. L. Hahn, Nuclear Quadrupole Spectroscopy Resonance (1958)

[31] Y. Masuda, Ph. D. Thesis

[32] A. Abragam, The principles of Nuclear Magnetism (1961)

[33] K. Koshigiri, private communications